Glacial Melt Water and Antarctic Bottom Water Formation and Circulation in the Weddell Sea Inferred by Tracer Observations

Master Thesis

USMAN AHMED

Master of Environmental Physics

Matriculation Number: 2953307

Supervisor: Dr. Oliver Huhn

Co-Supervisor: Prof. Dr. Torsten Kanzow

Department of Physical Oceanography

Institute of Environmental Physics

University of Bremen, Germany

Bremen, 18 May, 2017

Contents

Acknowledgement

I would like to honor my father Jameel Ahmed and my mother Naseema Jameel for their hardships and love for me. I would like to thank very humble Prof. Dr Monika Rhein for her unprecedented support for my Thesis. I feel fortunate enough that I worked with Dr. Oliver Huhn’s worthy and commendable supervision. I admire his scientific approach and guidance throughout the Thesis process. I am pleased that Prof. Dr. Torsten Kanzow accepted my request to become my co-supervisor.

I am thankful to Lars Jeschke and Anja Gatzka for the administrative guidance. At last but not least, my PEP friends ☺ Saqr Munassar, Nelson Igbinehi, Razib Vhuiyan and Andreas, who accompanied me throughout the PEP.

Abstracts

The Weddell Sea contributes the two third of cold deep ocean water mass formed globally. The global warming can force warm deep water entrainment to the ice shelves cavities, less sea ice formation and freshening of the bottom water, thus, global thermohaline circulation can be altered including sea level rise and imposing severe social and economic catastrophes. Therefore, a close investigation in the Weddell Sea is inevitable.

The Weddell Sea hydrographic and noble gas observations from 17 research expeditions have been used to analyze water mass formation, distribution and circulation. We applied an Optimum Parameter analysis to calculate the relative water mass fractions from the data.

The FRIS is identified as prominent in the Weddell Sea by its high, Helium (^{4}He) and Neon (Ne) concentrations, and High Salinity Shelf Water (HSSW) and Glacial Melt Water (GMW) fractions. There is a significant increase of GMW of 88% from the Ronne Ice Shelf region (RIS) to the Filchner Ice Shelf region (FIS). A ‘trapped’ Ice Shelf Water (ISW) core with the highest measured ^{4}He, Ne and GMW fraction is found in the Filchner Trough. A 20 year temporal analysis (1995 and 2014) on the northern Filchner Shelf has shown a decrease of HSSW by -30% and an increase of GMW fraction, and a ‘new’ GMW plume appears in 2014 which was not visible in 1995. We also detected an addition of up to 4.5% ^{4}He in FRIS water and an addition of 5.4% ^{4}He in ACC water. The highest GMW fraction in front of the Larsen Ice Shelf (LIS) is detected in WSDW. The WSBW formed at the Filchner Slope is also identified at the slope in front of the LIS and mixing of local WSDW with entrained WSBW is observed at 70°S on the slope in front of the LIS. The LIS local WSDW and WSBW formations are also certain.

The Weddell Transect and the Prime Meridian show the WSDW and WSBW outflow to the northeast of the Weddell Sea. There is also an inflow of AABW observed between Maud Rise and the continental shelf at the Prime Meridian. However, low resolution data and OMP inconsistency hindered the analysis of the bottom water.

1. Introduction

1.1 Background

The climate change is currently an important issue and demands prompt measures to investigate warming of the Earth and its consequences. The Southern Hemisphere has faced an increased warming of 3˚C (Hellmer et al. 2011) since 1951 at the Antarctic Peninsula. The Antarctic continent has the largest ice sheets on earth, equivalent to 58m sea level rise (Allison et al. 2013). One consequence of the warming has been seen through the disintegration of Larsen A completely (Seehaus et al. 2015) and Larsen B are partially fragmented in 1995 and 2002 respectively. The Wilkins Ice Shelf (2008) split away from its parent ice shelf much earlier than predicted (Hellmer et al. 2011) at the western coast of Antarctic Peninsula in Southern Ocean. Therefore, a precise observation of the parameters influenced by climate change is necessary. Several expeditions have been made to the Southern Ocean for multi-purpose scientific data retrieval.

I have worked on the general circulation in the Weddell Sea by detection of ocean water masses particularly basal Glacial Melt Water. I used the data comprising noble gasses in the oceanic water samples from the Weddell Sea region, particularly in close vicinity of the Larsen Ice Shelf (LIS) and Filchner-Ronne Ice Shelf (FRIS) regions. The data exclusively includes stations' positions, θ (Potential Temperature), *S* (Salinity), He (4-helium) concentration, Ne (Neon) and δ^3He anomaly (i.e. the 3-helium/4-helium ratio normalized to the atmospheric isotope ratio).

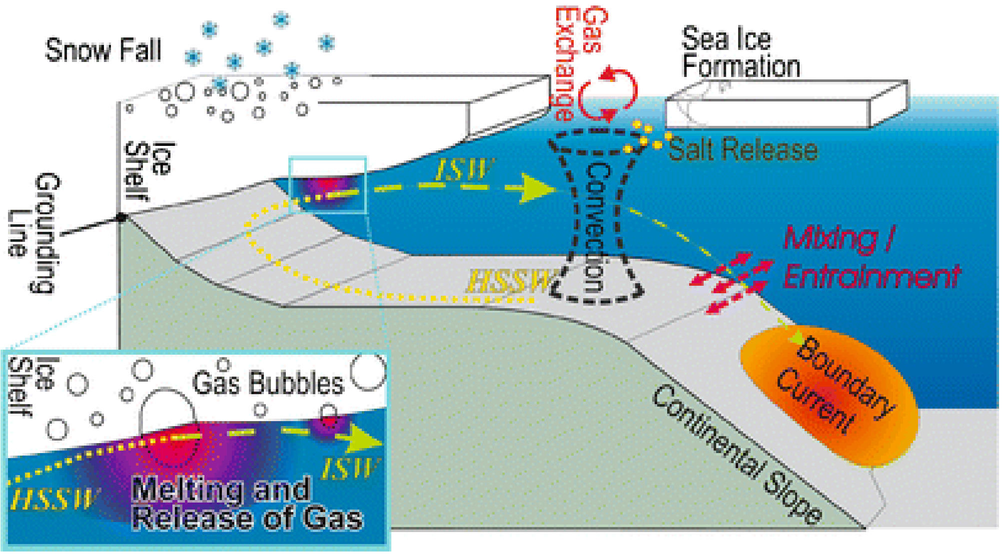

Figure 1.1.1 The depiction of water mass formation and of gas transfer from the atmosphere to the shelf ice, melting at the base and further mixing with HSSW. The left bottom subsection highlights the release of gas from glacial ice into pure GMW and ISW (Rodehacke et al. 2007).

Meteoric ice falls as precipitation over the Antarctic region and is further transformed into firn and over a course of time turns into glaciers. The average air content in Antarctic glaciers is 0.11 g cm-3 measured from 14 drill sites in Antarctica (Loose & Jenkins 2014). The Antarctic continental glaciers are in continuous offshore flow (Paolo et al. 2015). The Figure 1.1.1 represents the schematic process of dense water formation by interaction of the atmosphere, the ocean, and the ice shelf, i.e. the formation and ventilation of High Salinity Shelf Water (HSSW) formation at the shelf's front in so called polynyas and mixing of it with basal Glacial Melt Water (pure GMW) to form Ice Shelf Water (ISW) in the ice shelf cavity.

1.2 Southern Ocean

The Southern Ocean Figure 1.2.1 is defined as the region between the Antarctic continent and the subtropical convergence (where cold, northward-flowing Antarctic waters meet the relatively warmer waters of the sub-Antarctic). The Southern Ocean is the world's only zonal sea. The southern ocean shares its boundaries with the South Pacific Ocean, the South Atlantic Ocean and the Indian Ocean. The continental boundary to the south is surrounded by deep ice shelves approx. 500m deep (Foldvik & Gammelsrød 1988). The Southern Ocean is dominated by geostrophic currents named Antarctic Circumpolar Current (ACC) and Antarctic Subpolar Current (ASC).

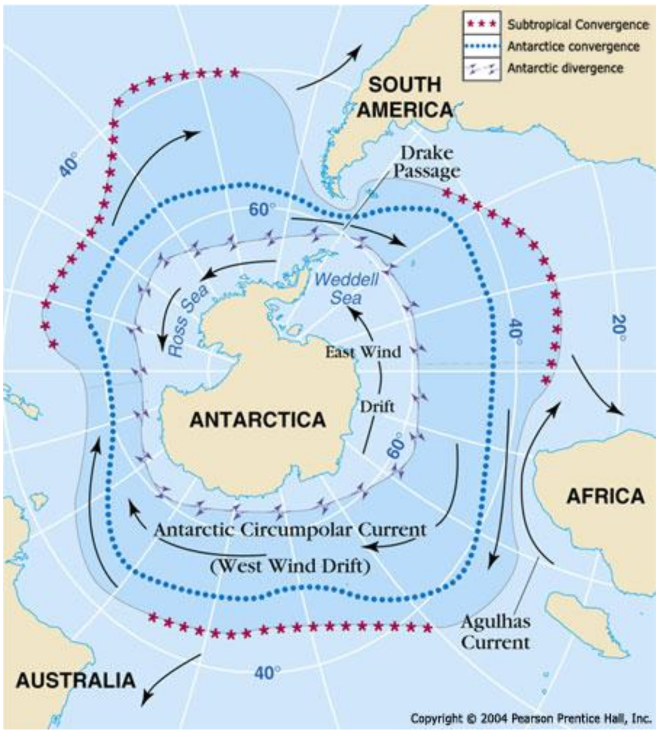

Figure 1.2.1 The map of Southern Ocean where red star represent the boundary of Southern Ocean as the subtropical convergence, the blue dots show the Antarctic convergence and the purple double-aero show Antarctic divergence. The black aero shows the direction of ACC and East wind drift.

The westerly wind implies zonal forcing of the sea surface known as West Wind Drift on the temperate side of Southern Ocean. On contrary the polar easterly induces East Wind Drift at the sea surface at the continental side (Foldvik & Gammelsrød 1988). The lack of landmass interference gives circular characteristic to the West Wind Drift known as Antarctic Circumpolar Current (ACC).

The only hindrance on the way of ACC is the Drake Passage between South America and the Antarctic Peninsula with transport measured 134 *Sv* (1 $Sv = 10^6$ m^3 s^{-1}) (Foldvik & Gammelsrød 1988) making it the strongest oceanic current. The West Wind Drift gives rise to northward Ekman transport and the East Wind Drift gives rise to southward Ekman transport. These Ekman transports in opposite directions accelerate the upwelling as a result of Antarctic Divergence. Therefore, the upwelling and downwelling can mainly be determined by the wind stress curl.

At the Antarctic Divergence region, the intermediate warm water from the north rises through upwelling along with the high saline deep water from the south. This form low saline cold surface water directed towards the Antarctic Convergence known as Polar Front, where, it sinks to form low saline intermediate water. The warmer subantarctic surface water is found at the subtropical convergence further towards the north where the temperature rises rapidly.

Particularly, at the Atlantic region the North Atlantic Deep Water (NADW) remains sandwiched between the Antarctic surface water and the Antarctic Bottom Water (AABW) until it mixes Antarctic waters in the ACC. Restlessly, AABW keeps flowing northward (Foldvik & Gammelsrød 1988).

1.3 Antarctic Ice Sheet Dynamics

The Antarctic ice sheet moves slowly from the mainland to the coastline and end up as a vertical wall of ice shelf called a Barrier. The ice shelves cover around one million square kilometer over the Southern Ocean. The Antarctic floating ice shelves cover a large area particularly in the Weddell Sea and the Ross Sea, whereas the Weddell Sea ice shelves areas alone can be compared with those of Greenland (Foldvik & Gammelsrød 1988).

The melting and calving of ice shelves represent the coastward flow rate of glacial ice. The collapse of an ice shelf leaves the space for the upstream glaciers and accelerates the coastward flow rate. The ice shelves’ loss is estimated by ice shelf fragmentation, ice bergs calving and underneath glacial melt. Estimation of the basal glacial melt rate is the most challenging due to the lack of direct observations (Loose & Jenkins 2014). State of the art melting and calving estimates are usually based on satellite observations and model results (e.g. Paolo et al. 2015; Rignot et al. 2013)

The Antarctic Ice Shelves are so wide that the only way to map and measure their temporal change in thickness at such a wide scale is possible only by satellite altimetry. Paolo et al., 2015 estimated ice shelf thickness trends from 18 years (1994-2012) satellite radar altimetry data. The FRIS thickness change is +0.2±0.5 m/decade on such a long term, however Figure 1.3.1 shows that the short term changes can be higher than the long term changes.

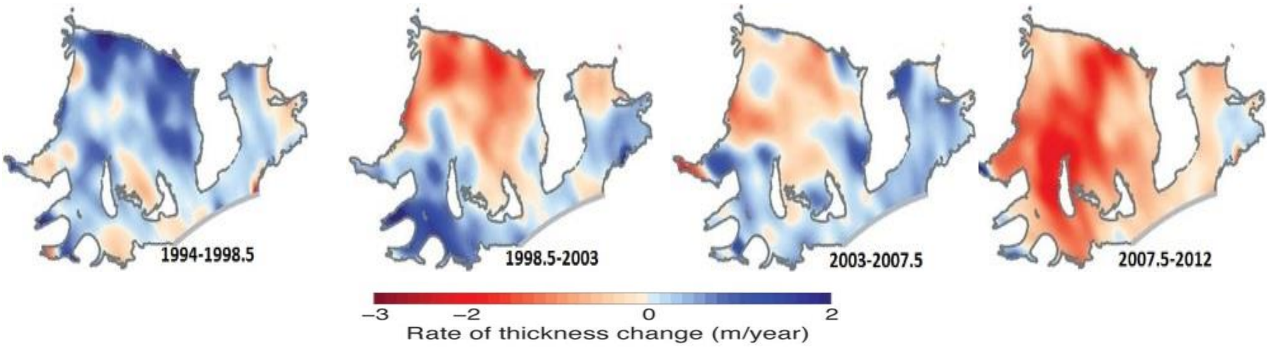

Figure 1.3.1 FRIS rate of thickness change for four consecutive 4.5 years interval (Paolo et al. 2015).

The Larsen C ice shelves average thinning rate is 3.8±1.1 m/decade (Paolo et al. 2015). The Larsen C Ice Shelf thinning has progressed from its north to south (Figure 1.3.2). According to Paolo et al., 2015, Larsen C ice shelf is expected to be fully vanished by the next 100 years.

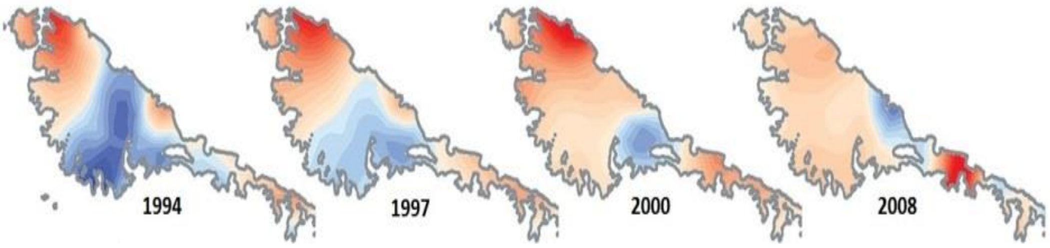

Figure 1.3.2 Larsen B,C and D Ice Shelves rate of thickness change for four specific times and FRIS (Paolo et al. 2015).

The fastest basal melt rates under ice shelves is estimated on the western side of the Antarctic Peninsula (Rignot et al. 2013). The Amundsen and Bellingshausen ice shelves account for only 20% from west Antarctica ice shelf area but by volume loss they account for 85% from west Antarctica with thinning rates of 19.4±1.9 m/decade and 7.4±0.9 m/decade (Paolo et al. 2015) respectively. The total Antarctic ice shelves average loss was reported 1.4±0.4 m/decade from 18 years (1994-2012) satellite radar altimetry data.

1.4 Ventilation and Water Masses Formation in the Weddell Sea

The Weddell Sea Figure 1.4.1 contributes more than two third of cold deep ocean water mass formed globally. The Weddell Sea is the region where most of the AABW (60%) is formed. The very cold bottom water in the Atlantic can be traced back to the Weddell Sea (Foldvik et al. 2004).

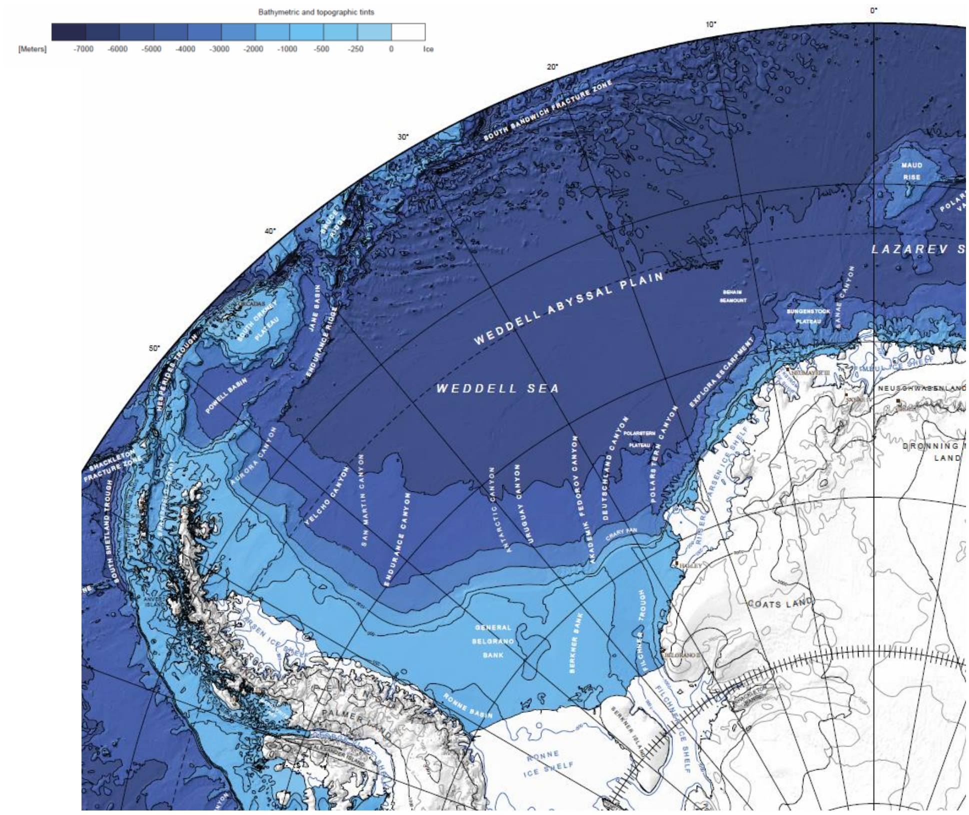

Figure 1.4.1 The map of Weddell Sea representing the bathymetry in meters and geographical features (IBCSO).

The Weddell Sea surface layer of cold water formed during winter as a result of sea ice formation is called Winter Water (WW) with 100 to 200m depth. The WDW is imported from the ACC through the Weddell Gyre (Ryan et al. 2016) typically above θ= 0˚C. The WW is mixed with the underlying Warm Deep Water (WDW) to form Modified Warm Deep Water (mWDW). The mWDW is sandwich between WW and WDW (Michels et al. 2002).

AABW is mainly derived from sea surface processes (e.g. formation of sea ice and brine rejection) and considered as young age water mass (i.e. the time since water sinks down from the sea surface). The whole process of sea ice formation involves intense heat transfer between atmosphere and ocean in the polar region that initiates thermohaline circulation. The Antarctic surface water heat loss to the atmosphere and formation of sea ice produce dense cold High Salinity Shelf Water (HSSW) mainly on the broad continental shelves, destabilizing the water column to form AABW by interaction with warm water masses at the shelf brake. The newly formed AABW in the Southern Ocean contains high level of dissolved oxygen, transient tracers such as Chlorofluorocarbons (CFC's) etc. It is also high in ^{4}He and Ne (see 1.1).

The AABW meets NADW in the Atlantic Ocean, where AABW tends to be colder, denser and fresher than NADW at relevant depths and flows below the NADW (Bulister et al. 2013). The AABW enters the Scotia Sea along the western boundary of the Weddell Sea. Thus providing the cold dense water to the ACC where the Scotia Sea plays as a junction between AABW and the ACC (Locarnini et al. 1993).

In Antarctica most of the sea ice is formed every year that prevents the ice thickness from 1 to 2 m. The open boundaries of the Southern Ocean to the north increases the ice melt rate in austral summer leaving around 10% ice covered area left (Foldvik & Gammelsrød 1988).

The Weddell Sea is almost 80% covered with sea ice in austral winter. The Weddell Sea minimum sea ice coverage is reported 50% in austral summer (Michels et al. 2002).The cold deep water formation depends on the dense shelf water with salinities typically above 34.465 with average depths of 500m water column at the continental shelf break in the Weddell Sea (Hellmer et al. 2011). The shallower the shelf break the more saline water is observed. The formation of sea ice in austral winter particularly leads to form HSSW through a so called process of brine rejection (Foldvik et al. 2004). The big volume of HSSW is aided by so called polynyas along the FRIS (Markus et al. 1998).

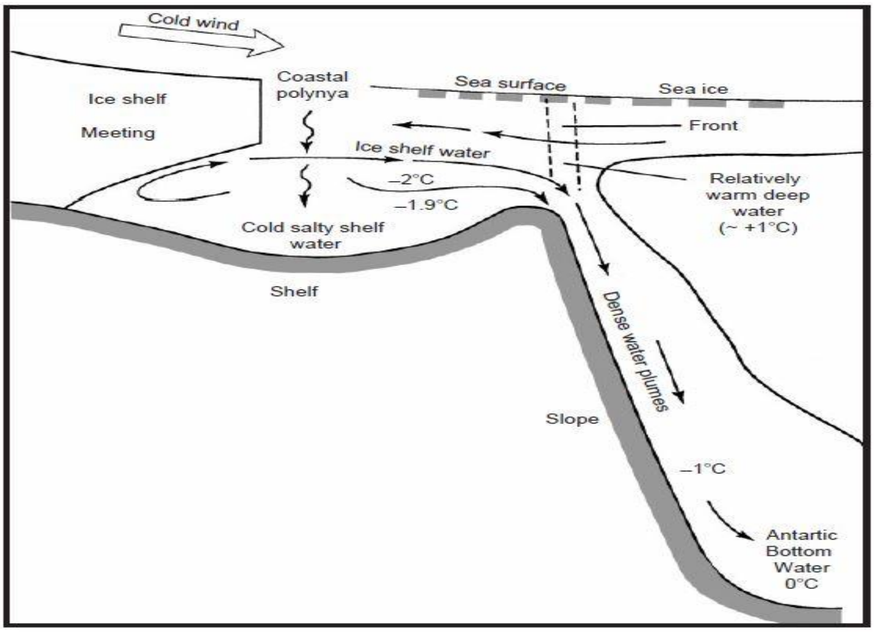

Figure 1.4.2. Schematic of circulation and water masses in the Antarctic continental shelf (Gordon 2013).

The regional sea ice production at a particular location may differ from the observed sea ice thickness in winter. This is the special case near the Barrier (see Figure 1.4.2) where open water is formed due to off coast winds. Such open water is called coastal polynya, in most cases latent heat polynya (Foldvik & Gammelsrød 1988). The polynyas along FRIS are backed by southwesterly winds. The newly formed sea ice is transported away and HSSW is continuously formed.

Most of HSSW in Weddell Sea is produced in its southwest region (Foldvik et al. 2004). The HSSW in the southwest of Weddell Sea has potential temperature θ= -1.9˚C and salinity ≈34.7 dense enough to sink down (Huhn et al. 2008) . This process is often referred to as the "Foster-Carmack process" (e.g. Foster & Carmack 1976.

1.5 Ice Shelf - Ocean Interaction and Basal Glacial Melting

The Ice shelves around Antarctic Ocean are important sources of AABW formation and a part of the locally formed HSSW flows into the ice shelf cavity. The ice shelf ground base is around one degree colder than surface freezing point with a *draft of 1500 meter* (Foldvik et al. 2004). The higher hydrostatic pressure reduces the freezing point under the ice shelf cavity. This helps HSSW to melt glaciers and to form GMW in the ice shelf cavity. The mixture of HSSW with GMW is called ISW. The ISW retains a potential temperature lower than ≈ -1.9˚C (surface freezing temperature). The ISW formed under the ice shelf flows out of the cavity onto the shelf in front and further down over the continental slope and mix with overlying WDW (θ > 0˚C) or mWDW. The mixture of ISW and WDW is dense enough to sink and form WSDW (0˚C > θ > -0.7˚C) and WSBW (-0.7˚C >θ > -1.5˚C) (Foldvik & Gammelsrød 1988). The θ of WSDW is higher (>-0.7˚C) than WSBW (<-0.7˚C) due to mixing with comparatively warmer water i.e. WDW, but remains below 0˚C. Mixing of HSSW and mWDW (WW+WDW) is relatively warmer than the WSBW (ISW+WDW) also forms the WSBW (Figure 1.5.3 A). That process is often referred to as "Foldvik process" (e.g. Foldvik et al. 1985).

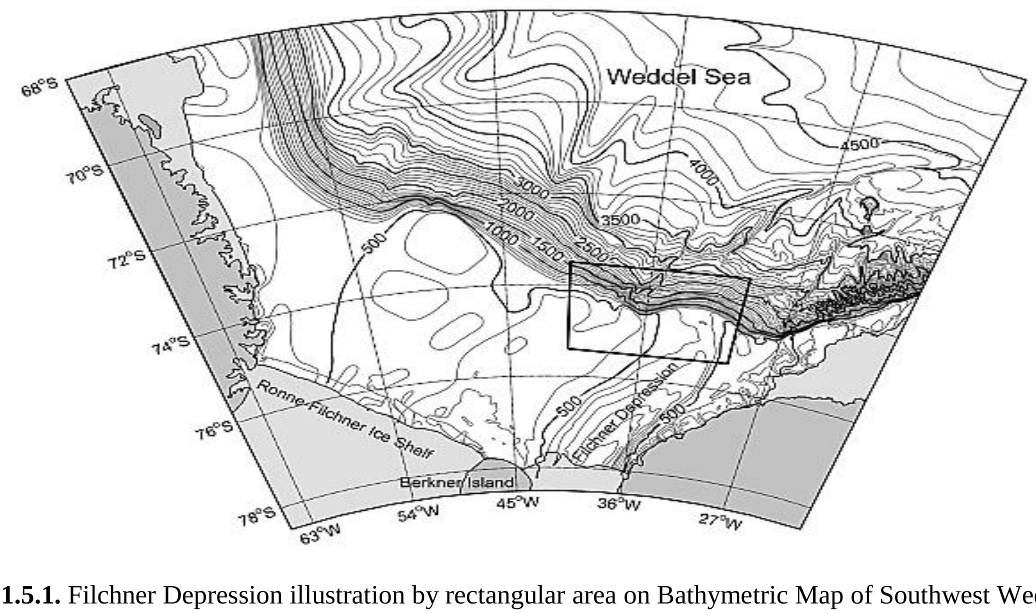

Figure 1.5.1. Filchner Depression illustration by rectangular area on Bathymetric Map of Southwest Weddell Sea (Foldvik et al. 2004).

The ISW in the Weddell Sea is found below 300m depth with characteristic θ below surface freezing point (≈ -1.9°C). The core of the ISW is characterized by the minimum of potential temperature (≈ -2.19°C) found at approx. depth of 425m. The salinity decreases from 34.05 in surface water to 34.60 in the ISW core with the highest ^{4}He concentration.

The region around the Filchner Trough Outflow is considered pivotal because large amount of Weddell Sea Deep Water (WSDW) and Weddell Sea Bottom Water (WSBW) is formed (Figure 1.5.2). ISW mainly flows out of the Filchner Depression (Foldvik et al. 2004) , a fraction of ISW also flows westward on the shelf and along the continental slope.

The ISW losses its coldness fast as it slops down the Filchner Depression (Huhn et al. 2008). The mooring data confirmed that the major outflow pathway of ISW is the Filchner Depression with a 100Km wide and 100m thick layer at 600m depth (Figure 1.5.2). The large flow of potentially supercool ISW shows the immense role of Weddell Sea ice shelves (Foldvik & Gammelsrød 1988). The reported 1*Sv* of ISW outflow largely from Filchner Depression is responsible for the 3.9±1.2 *Sv* WSBW/WSDW formation with estimated 10% ISW (Figure 1.5.3 B) originated from FRIS (Huhn et al. 2008).

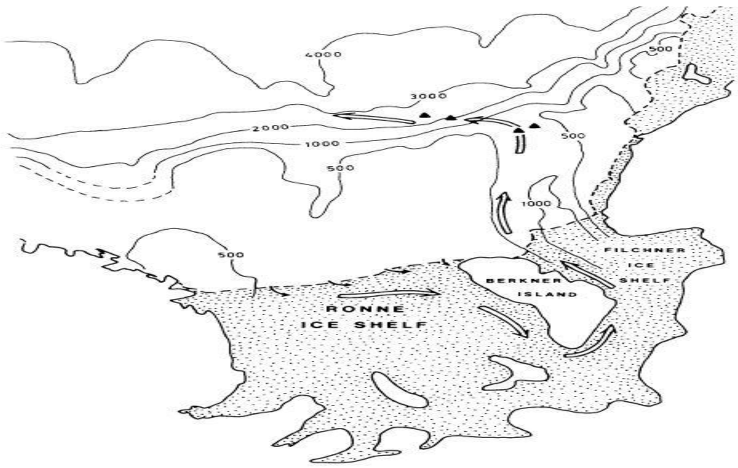

Figure 1.5.2. Sketch of flow of ISW under FRIS, the positions of moorings and slopes are denoted by triangles (Foldvik & Gammelsrød 1988).

The LIS contribution to WSBW formation is still uncertain (van Caspel et al. 2015), however, LIS water traces have been found in the formation of WSBW. ISW traced back to LIS is not combination of local HSSW and GMW but a mixing of mWDW and GMW forming 1.1±0.5 *Sv* WSDW/WSBW (Huhn et al. 2008). Nicholls et al. 2004 reports also ISW formation in the western Weddell Sea by basal ice shelf melting induced by mWDW, pre-conditioned during winter, but not by HSSW.

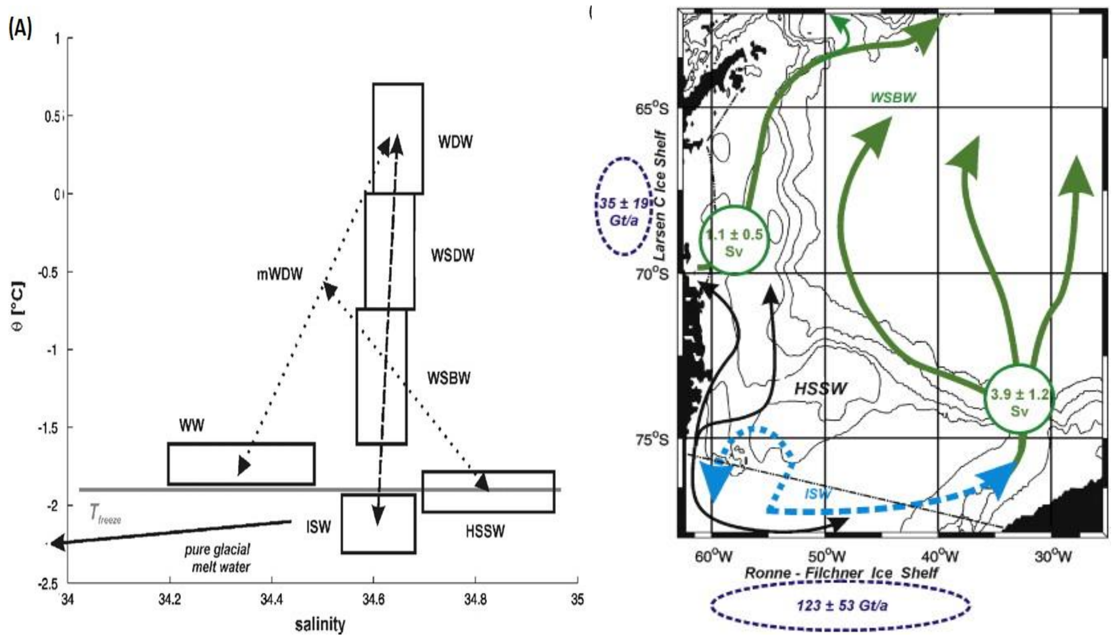

Figure 1.5.3. Distribution of water masses in the western Weddell Sea. (A) θ is potential temperature and salinity is in psu. The solid arrow is pointing pure glacial melt water; the horizontal grey line indicates surface temperature the two doted arrows point water masses mixing and dashed arrow point formation of WSBW. (B) Green arrows show WSBW distribution encircled relevant transport. Black arrows show HSSW and light blue dashed arrows show ISW largely towards FRIS and blue dashed circles with numbers show relevant GMW rate (Huhn et al. 2008).

The decay of LIS (A and B) has influence on western Weddell shelf water where large icebergs drifts are observed by the satellite images. The iceberg calving and lack of sea ice formation creates open water (coastal polynya) in shallow basin, which were formerly covered by ice shelves. The open water created in such a process results in enhanced salinity in the basins. Such process can also influence nearby shelves water density once the basin has meet its threshold density (Hellmer et al. 2011).

1.6 Current Evidences of Warming and Freshening of the Weddell Sea Water and Future Projections from Modeling (FESOM)

Southern Ocean Warming and increased basal Ice Shelf melting are evidenced through sophisticated model projections using global sea ice - ice shelf - ocean interactions (Timmermann & Hellmer 2013). The model is named Finite Element Sea-ice Ocean Model (FESOM). The model focused Antarctic marginal seas and used atmospheric forcing of the last century from two different climate models (HadCM3 and ECHAM5/MPI-OM) to project recent Antarctic Ocean dynamics, both climate models are based on different atmospheric parameters; (Timmermann & Hellmer 2013). The models show comparable ice shelf basal melt trend,

The future projections of Southern Ocean sea ice dynamics are derived from the atmospheric output of IPCC's fourth assessment report with two different scenarios E1 and A1B, where A1B scenario is supposed to be more realistic and pessimistic as compared to E1 (where CO_2 is stabilized at

≈440ppmv by 2100 in E1 scenario) based on the atmospheric CO_2 concentration trend from 2000 to 2199. The data for ECHAM5 is only available till 2099. Eventually we get four FESOM future projections from the two climate models separately with each scenario. Each model also used the 20C scenario from 1958 to 1999 for current Southern Ocean status.

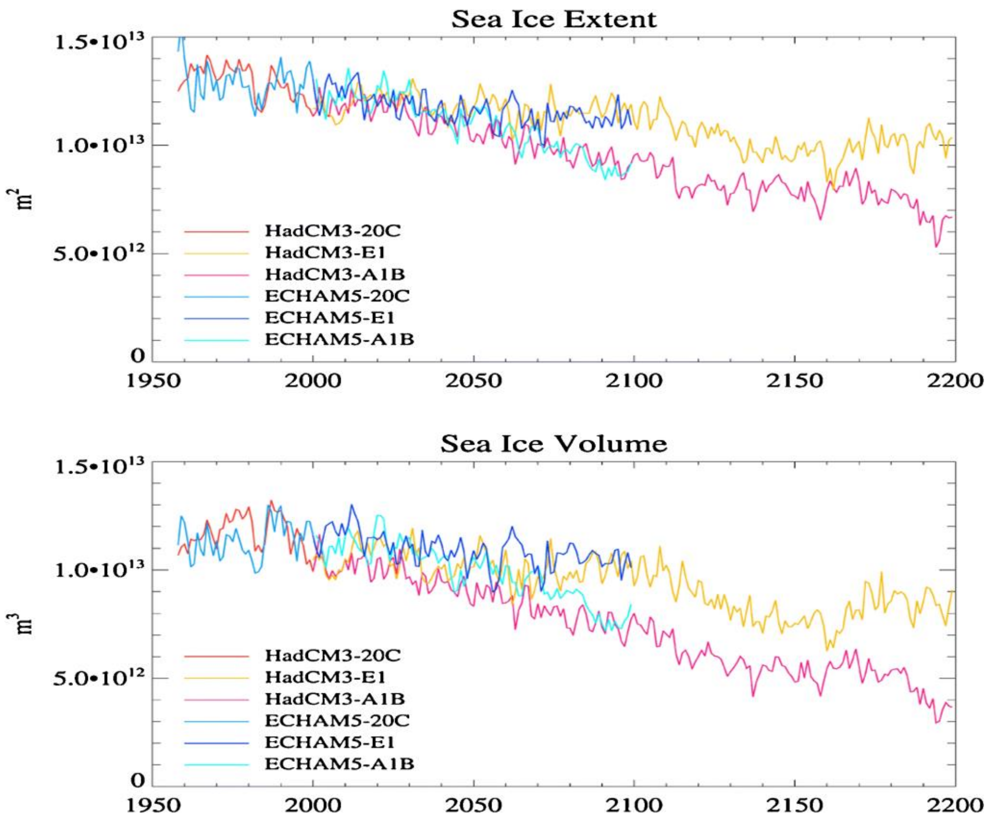

Figure 1.6.1. Annual mean Antarctic sea ice extent and volume simulations from FESOM (Timmermann & Hellmer 2013).

The HadCM3 (Figure 1.6.1) shows that the sea ice extent has already started decaying from 1990's. Both climate models show a fast decline throughout the time series in A1B scanario (most pessimistic). The ECHAM5 (Figure 1.6.2) future simulation is quite colder side within this century in both scenarios, as contrary to HadCM3 in the Southern Ocean. In addition, no trend of ECHAM5 is in the warming favor during 21st century in the World Ocean, however the differences between the scenarios are not profound in either climate model.

Timmermann and Hellmer, 2013 defined two water masses. The "Weddell Shelf" when mean potential temperature is measured from 200m to the bottom of the shelf excluding surface water due to short term variations of potential temperature, the "Weddell Deep" when mean potential temperature is measured from 400m to 1000m excluding waters in subice cavities.

The HadCM3 shows continuous warming trend with interannual variations in the "Weddell Shelf" waters. Further HadCM3-A1B shows the warm deep water influx into the shelf water in second half of 21st century.

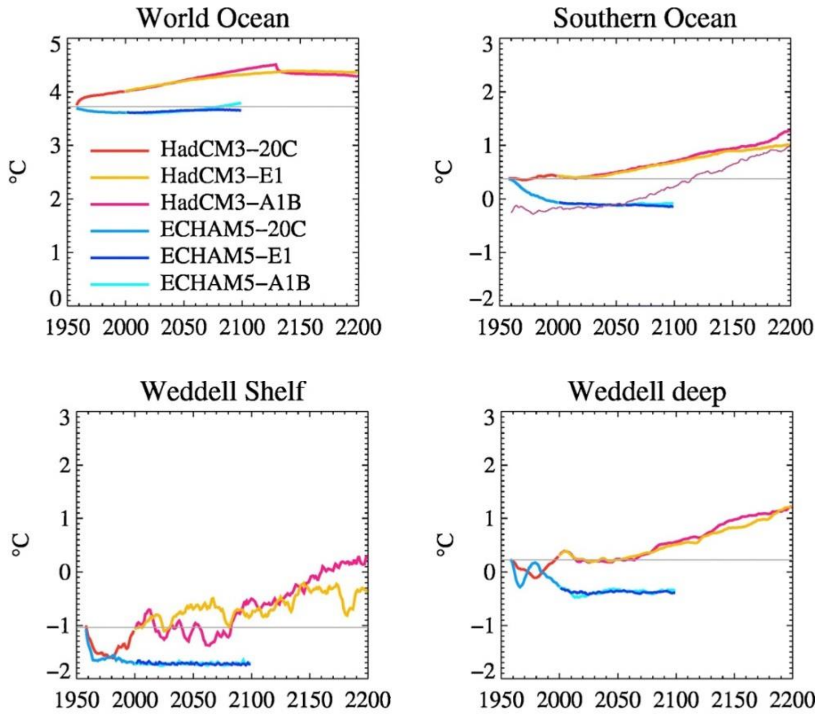

Figure 1.6.2. Mean potential temperature measured with isobath boundary of 800m between the Weddell Shelf and the Weddell Deep. A magenta line is added to Southern Ocean figure for comparison with mean potential temperature from HadCM3-20C/A1B in Arctic ~60˚N. The gray horizontal line shows mean temperature from NOAA's world ocean atlas 2001 (Timmermann & Hellmer 2013).

The global mean salinity trend (Figure 1.6.3) seems to be constant as part of the oceans coupling. For the Southern Ocean, ECHAM5 and HadCM3 both show negative trends in 21st century but it is strong negative after 2100. The freshening is most probably due to increasing of GMW and less sea ice formation. Further, the "Weddell Shelf" shows the strong negative trend in both FESOM's climate models. In "Weddell Deep", the trend is close to average salinity with a noticeable difference between ECHAM5 and HadCM3 but after 2100 freshening increases in the "Weddell Deep". The FESOM (Figure 1.6.4) present day forcing scenarios show very close melt rates to each other around 90 Gt/year at FRIS, whereas ECHAM5-A1B future scenario shows 110 Gt/year melt rate with no trend from E1 scenario. The HadCM3-A1B varies within the first half of the 21st century between 300 to 500Gt/year, which is largely due to increased WDW influx.

A rapid increase in FRIS basal melt is observed from FESOM (HadCM3) which is further more dramatic in 22nd century and observed as ≈600 Gt/year in the start of 22nd century and reaches ≈2500 Gt/year in the end of the century. The rapid basal melt increase from FESOM is supported by BRIOS model with an alarming basal melt rate reaching 1500 Gt/year in 22nd century.

In Eastern Weddell Ice Shelves (EWIS), the FESOM simulations for all ECHAM5 scenarios and HadCM3 present day (20C) tend to show ≈50 Gt/year glacial melt rate. In the start of 22nd century basal melt rate increases rapidly in FESOM but BRIOS show a constant trend of basal melt rate at ≈150Gt/year.

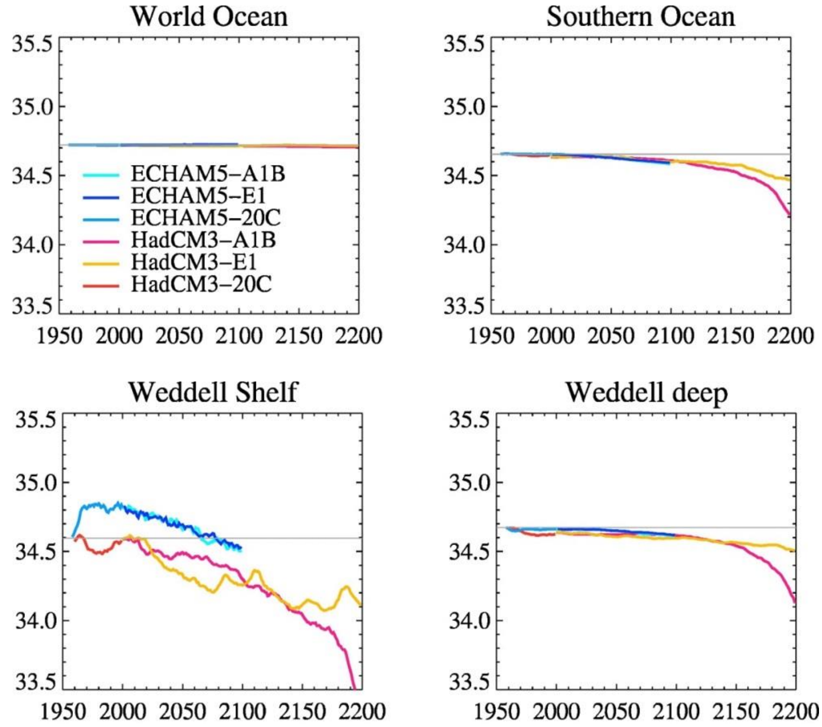

Figure 1.6.3 Mean salinity simulations from FESOM. The gray horizontal line shows mean salinity from NOAA's world ocean atlas 2001 used as the initial reference for all simulations (Timmermann & Hellmer 2013).

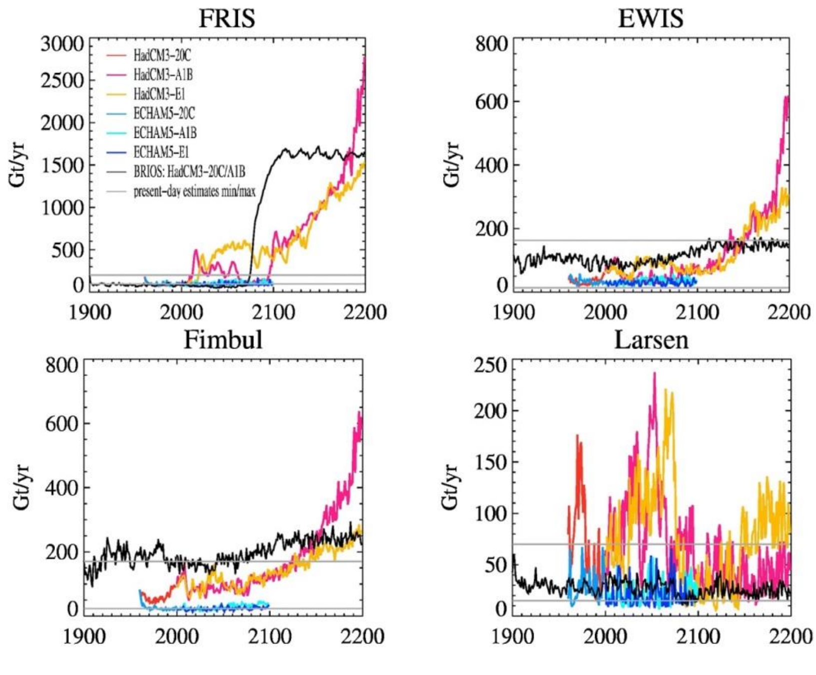

Figure 1.6.4. Annual means of ice shelves basal mass loss in the Weddell Sea with varying y-axis values. The grey horizontal lines show current range of melt rates from independent estimates (compiled from TWH12) (Timmermann & Hellmer 2013) .

As contrary to other ice shelves, the LIS (B and C ice shelves) has an increase basal melt trend in the 21st century by FESOM (HadCM3) but then reduces to the present day value in the start of 22nd century. That is because of the FRIS increased basal melt rate from 22nd century resulting in less dense shelf water. This result in reduced formation of deep water thus shallower cold water is supplied to the western shelf constantly. Eventually, the basal melt rate of the LIS decreases as coupling result with FRIS in 22^{nd} century (Timmermann & Hellmer 2013).

2. Methods and Data: Noble Gases and the Optimum Multiparameter (OMP) Analysis

2.1 Helium and Neon as Glacial Melt Water Indicator

Assessments of the NG are supported by their unique characteristic of being inert and lake of involvement in biology and chemistry of ocean waters. Therefore they can be used as a tool to estimate e.g. the rate of diapycnal mixing at the equatorial thermocline, deep water ventilation, the rate of air-sea gas exchange and the GMW formation rate. The heavier noble gas is more soluble in water and the solubility of NG is largely affected by the changes in temperature and salinity. CFC's or Tritium are so called transient tracers, i.e. they vary in time and, thus, can be used to determine the age of water masses (Huhn et al. 2008).

^{4}He and Ne are useful parameters among the NG to estimate GMW fraction due to their low solubility (Schlosser 1986; Hohmann et al. 2002; Huhn et al. 2008; Loose & Jenkins 2014). Oceanic water in atmospheric equilibrium is low in ^{4}He and Ne due to their low solubility. The atmosphere has a specific amount of (NG); a fraction of atmospheric air is trapped during the formation of glacial ice. Hence, pure basal GMW is extremely high in ^{4}He and Ne, when the glacial ice is melting under enhanced hydrostatic pressure at the underside of a floating ice shelf. Thus, ^{4}He and Ne anomalies (excess) in ocean water indicate the basal melting of glaciers and can be used as the direct measure of the GMW content.

The basal melting under higher hydrostatic pressure as compared to surface water leads to dissolve the low soluble ^{4}He and Ne completely into the melt water (Huhn et al. 2008). The pure GMW has an excess of Δ^4He=1280% and Δ^4Ne=890% (Loose & Jenkins 2014). The Δ denotes the saturation anomaly referenced to the air-water surface solubility equilibrium shown in the equation below. For $He_{equ} = f\ (\theta, S)$ and $Ne_{equ} = f\ (\theta, S)$ we used the solubility function of Weiss 1971.

$$\Delta^4 He(\%) = \left(\frac{He_{obs}}{He_{equ}}\ -1\right) \times\ 100 \qquad \text{Eq. 2.1}$$

The first measurements of WSBW samples show ^{4}He excess about 1-2% due to influx of ISW in WSBW (Schlosser 1986). ^{4}He traces in WSBW reflect the contribution of pure GMW mixing with HSSW, WW and WDW in the formation of WSBW. The observed ^{4}He excess ranges typically from

≈ 5% in surface water to 19% with maximum excess found in the ISW core (Schlosser 1986). Huhn et al., 2008 found even higher values in ISW at FRIS containing 20% of helium excess equivalent to 1.4% of GMW after considering 5% additional Δ^4He background from other sources. The ^{4}He concentration decreases between 50m to 150m depth in the shelf water and increases again below this depth, and shows a maximum in the core of ISW. After the ISW is sloped down the Filchner Depression, the ^{4}He concentration reduces to 10% with a 0.5% fraction of GMW in ambient water (Huhn et al. 2008).

The active hydrothermal vents in the mid Pacific Ocean ridges are the major additional sources of ^{3}He to the deep ocean water with a small addition of ^{4}He (so called mantle or primordial helium). The ^{3}He is transported into the Circumpolar Deep Water (CDW) increasing the ^{3}He/^{4}He ratio in CDW and hence also in WDW. The 3He/^{4}He ratio is usually normalized to the atmospheric isotopic ratio and expressed as δ^3He (see Eq. 2.2).

$$\delta^3 He(\%) \;=\; [\frac{(^3He/^4He)_{obs}}{(^3He/^4He)_{atm}} - 1] \times 100 \qquad \text{Eq. 2.2}$$

Therefore WDW is high in δ^3He as compared to other water masses (see Table 1). The ^{3}He from tritium decay is assumed negligible (due to rare existence of bomb tritium in the area of investigation). The GMW/ISW other ways show a significant increase from a crustal source (as a product of uranium decay in the rock on which the glacial ice rests and slides towards the ocean). Hence in ISW/GMW the δ^3He is reduced and slightly larger values of ^{4}He are expected as compared Ne. Since, Ne in glacial ice has its sole origin in atmospheric air, therefore Ne can be used to estimate the contribution of crustal ^{4}He and mantel ^{4}He (Hohmann et al. 2002). Thus, Neon (Ne) serves as an independent tracer for the GMW, because Ne has no additional source like ^{4}He.

2.2 Detection and Quantification of Water Masses Using an OMP:

To calculate the relative fractions of the relevant water masses, in our case mainly of GMW, we used the so called Optimum Multiparameter (OMP) analysis, in our OMP analysis (Hinrichsen & Tomczak 1999; Huhn et al. 2008). Water masses can be described mathematically by functional relationships between the hydrographic properties and by a set of standard deviations about those relationships (Hinrichsen & Tomczak 1999). Any conservative water mass type can be calculated as relative fraction by assigning the associated parameters to that water mass in a series of linear relations as shown in the equations below. The variable ($x_1 \rightarrow x_4$) represents the water mass types with ($T_1 \rightarrow T_4$) and ($S_1 \rightarrow S_4$) as their respective associated parameters, similar for other conservative parameters like ^{4}He, Ne and δ3He.

$$x_1T_1 + x_2T_2 + x_3T_3 + x_4T_4 = T(obs) \qquad \text{Eq. 2.3}$$

$$x_1S_1 + x_2S_2 + x_3S_3 + x_4S_4 = S(obs) \qquad \text{Eq. 2.4}$$

.

.

.

$$x_1 + x_2 + x_3 + x_4 = 1 \qquad \text{Eq. 2.5}$$

This basis of the OMP analysis is to invert this linear system of mixing equations (see Eq. 2.3 and Eq. 2.4 etc.) combining the relative fractions (x_i) of the four water masses (e.g. here GMW, WW, HSSW and WDW) and (in this case) five conservative hydrographic properties (e.g. θ, *S*, ^{4}He concentration, Ne concentration, δ^3He anomaly) as well as mass conservation (Eq. 2.5) and the observed properties of a water sample. This equation system is inverted and solved in a least-square manner. The inverse method technique resolves the relative contributions of the four water masses that fit best to the observed parameters.

The parameters of the pure water mass type must remain conserved until mixing occurs with another water mass type. The system of equations is normalized by the mean and the range each property spans to account for their different orders of magnitude.

Furthermore, it is weighted by the average uncertainty of each property to account for the different signal-to-noise ratios. The last equation Eq. 2.5 represents the mass conservation. A weight for mass conservation cannot be calculated in the same way as for the parameters. The mass conservation equation is usually weighted the highest of the parameters' weights (Hinrichsen & Tomczak 1999). The highest weight from those of parameters for the mass conservation is necessary to normalize the water mass fractions on the scale of 1.

The above equations are a set in linear relation (Eq. 2.6) and the Inverse method for an over-determined system is applied for the OMP analysis (Eq. 2.7).

$$A\,x = d \qquad \text{Eq. 2.6}$$

$$x = (A^tWA)^{-1}\,A^t\,Wd \qquad \text{Eq. 2.7}$$

In our OMP analysis the matrix A includes the five parameters of the four water masses plus mass conservation. To normalize the equation system and to account for the different orders of magnitude of the parameters, each parameter (except mass conservation) is subtracted by the individual mean of the parameters and divided by the individual standard deviation of the parameters. Vector d contains the parameters of one observed water sample. It is also normalized by applying the same subtraction of mean and dividing by standard deviation as the Vector A. W (in Eq. 2.7) contains the weighting factors for each parameter to account for the different signal-to-noise ratios of the different parameters. These weighting factors account for the standard deviation of the source water mass properties (e.g. $Std(\theta_i)$) and the assumed scatter (or possible range) of the water mass properties (e.g. ε_θ). The inversion of the equation is repeated for each individual water sample with its parameters in vector d and with the same vector A in order to get solution vector x containing the optimum water mass fractions for each sample.

2.2.1 Setting the OMP Water Mass Properties

The first step in the OMP analysis is to set the known parameters of the individual water masses (see Table 1). For GMW, we adopted the parameters from Loose & Jenkins 2014. For the three other water masses, i.e. WW, HSSW and WDW, we first considered using the values from Huhn et al. 2008 and then adjusted the parameters to the observed data from the Weddell Sea (see Table 2) comprising θ, S, ^{4}He, Ne and δ^3He. The weight factor in Table 1 is the square root of the weight.

Table 1. Source water properties in context of Optimum Multiparameter (OMP).

Properties	WW	WDW	HSSW	GMW	Weight Factor
Pot. Temperature [˚C]	-1.88	1.00	-1.91	-91.08	563.69
Salinity [psu]	34.00	34.70	34.84	0.00	215.75
^{4}He [nmol/Kg]	1.79	1.82	1.90	28.44	665.25
Ne [nmol/Kg]	8.05	8.00	8.45	91.97	83.80
δ^3He [%]	-1.80	9.50	-0.50	-3.70	11.79
Mass Conservation Σx [%]	100	100	100	100	665.25

The above parameters have been carefully set by using the Weddell Sea water masses identified on the multiple property plots shown in Figure 2.2.1. We aimed to represent the four water masses as good as possible and to create parameter polygons enveloping the observed data as good as possible.

The θ for the pure GMW is determined by calculating its heat conduction between the surrounding seawater and the inner ice shelf temperature and its latent heat consumption. This latent heat consumption reduces the surrounding seawater temperature according to Loose & Jenkins 2014. The θ of pure GMW from its Latent Heat consumption and heat conduction is derived through the equation below given by Loose & Jenkins 2014.

$$\theta(gmw) = \theta f - \frac{Lf}{Cp} - \frac{Ci}{Cp}(\theta f - \theta i) \qquad \text{Eq. 2.8}$$

The θf is the freezing point temperature at the ice shelf base, θi is far field ice shelf temperature and Lf, Ci and Cp are latent heat of ice melting, heat capacity of ice and water respectively. We have used θf = -2.5°C (at ≈800 dbar and a salinity of 34.6) and θi of -20ºC in the equation. The θ of pure GMW is then calculated -91.08ºC. The most efficient parameters to quantify the GMW are ^{4}He and Ne. The ^{4}He and Ne concentrations values for the pure GMW are obtained by using the anomaly Δ^4He=1280% and ΔNe=890% (Loose & Jenkins 2014) and their respective saturation functions (θ=-2.5ºC, salinity=0) in the sea water. The δ^3He for pure GMW is not known due to unknown amount of crustal ^{4}He in pure GMW at different depths and locations. Therefore, the lowest δ^3He value of -3.70% is chosen from the available data.

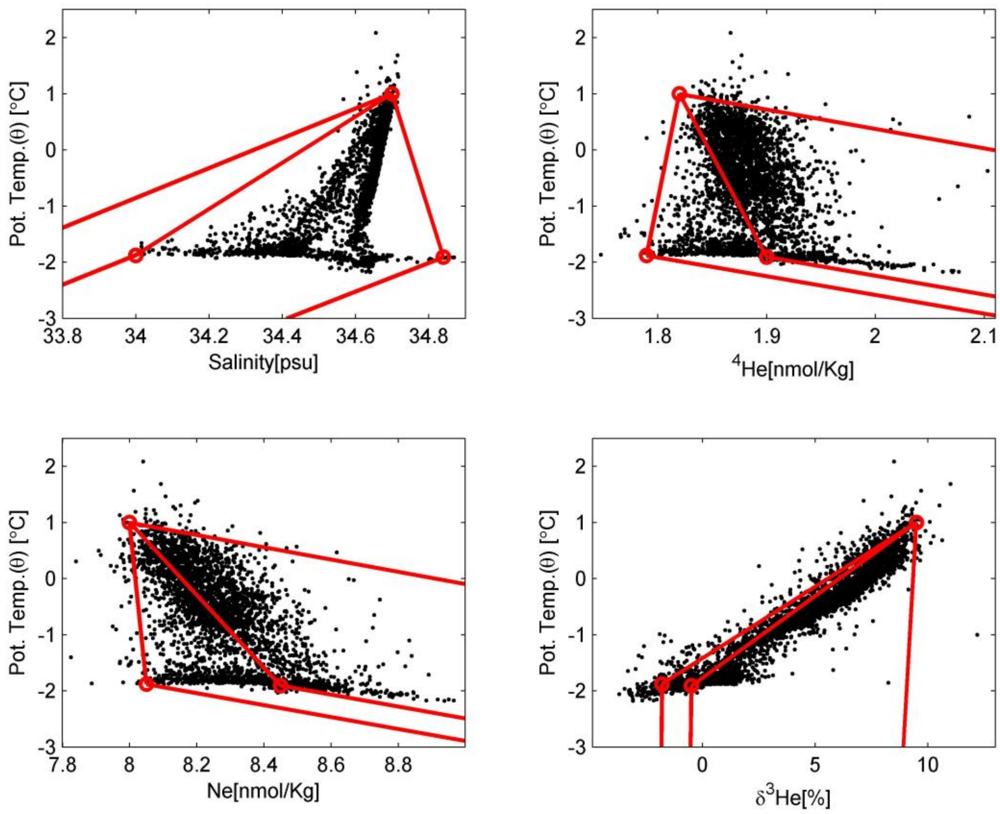

.

Figure 2.2.1 The hydrographic parameters subplots with red lines making two rectangles among the four water masses (i.e WW, WDW, HSSW and GMW) as defined in Table 1. The black dots are all available measurements from the Weddell Sea south of 60°S.

The ^{4}He and Ne concentrations values for the WW are set to surface water equilibrium values, i.e. assuming Δ^4He=0% and ΔNe=0% using the saturation function (θ=-1.88ºC, salinity=34). The salinity of WW 34.0 psu is chosen as the lowest value measured in surface water, which makes HSSW well distinct from the WW in OMP analysis. The δ^3He for WW is derived from the atmospheric $^3He/^4He$ ratio of $1.4x10^{-6}$ using Eq. 2.2. The parameters for the HSSW and WDW are identified from the Figure 2.2.1.

The weight factors (Table 1) are the ratios (e.g. $Std(\theta_i)$ /ε_θ), i.e. the standard deviation of the source water mass properties (e.g.$Std(\theta_i)$) and the estimated average scatter (or range) of the water mass properties (e.g. ε_θ). For the ε we used ε_θ= 0.08 °C, ε_S = 0.08, ε_{He} = 0.02 nmol/kg, ε_{Ne} = 0.5 nmol/kg, and ε_{δ^3He} = 0.5%. However, artificially we reduced the weight of Ne, since the ^4He signal-to-noise ratio from glacial ice (air plus crustal ^4He, see section 3.1, e.g. Figure 3.1.7 and Figure 3.1.8) is higher than that from Ne.

2.2.2 Errors and Uncertainties of the OMP

The mass conservation is one of the strongest constraints in the OMP analysis. However, in some cases water mass fractions < 0% or > 100% occurred. This may be the case if data points are outside the mixing polygons; see Figure 2.2.1. Note that the values ε "increase" the size of the mixing polygons and, hence, the tolerance for the OMP calculation, so that not all data points outside the polygons lead automatically to erroneous OMP results. For those cases, the calculated water masses fractions were set to 0% if below 0% and 100% if above 100%. Therefore, mass conservation (Σx) is compromised in some cases 2.2% of the final water mass fractions have Σx > 105%, 13.1% have Σx >101% and 21.7% have Σx > 100% in the Weddell Sea. No Σx is below 100%.

The errors or uncertainties of the OMP derived water mass fractions 'x' cannot be calculated directly, since the uncertainties of the set water mass properties (matrix A in Eq. 2.7, Table 1) and the observations (vector d in Eq. 2.7) cannot be differentiated in an easy way. Hence, Huhn et al. 2008, have assessed the uncertainties of the OMP water mass fractions 1) by individual variation of each source water mass property (i.e. the values in Matrix A, Eq. 2.6 or Eq. 2.7, Table 1) within their respective uncertainties ε, and 2) by statistically (random) variation of the properties of the water sample (i.e. the measurements in vector d, Eq. 2.6 or Eq. 2.7) within their measurement errors (see 2.3.1 for the errors of the measurements). By propagating the resulting deviations from the unvaried result, they got a measure of the uncertainty of the water mass fractions: GMW ± 0.03 %, WW ± 5 %, WDW ± 3 %, HSSW ± 5 %. Varying only the ^4He and Ne values of GMW in matrix A, the resulting GMW fractions $x_{(GMW)}$ have an uncertainty in the order of 0.01 %.

2.3 Date Set

The up-to-date data set from the Weddell Sea region used here is unique. It comprises hydrographic (θ, S) and noble gas (^{4}He, Ne, δ^3He) measurements spanning a period of 24 years and containing 4495 data points from 17 different cruises. Those 289 data points that were scattered out of the inner rectangle (red line) in θ-S subplot Figure 2.2.1 have been filtered out.

The RV-Polarstern has made several research journeys in the Antarctic regions. One aim was to find the WSBW formation and GMW fractions by measuring hydrographic characteristics and tracers observations. The data from other cruises are also included. Data have been acquired usually in austral summer to investigate the shelf water column transitions and detection of water masses in the wake of GWM addition (Huhn et al. 2008). Therefore, the data from 17 different expeditions have been analyzed (see Table 2). The sampled stations with respect to the used cruises are shown in the map (see Figure 2.3.1) and in the table below.

Table 2. Cruises overviews from the data are used for water masses identification and retrieval.

Year	Ship	Cruise Label
1990	RV Meteor	M 11/5
1990	RV Polarstern	ANT 9/2
1992	Akademik Fedorov	ISW-1
1992	RV Polarstern	ANT 10/4
1995	RV Polarstern	ANT 12/3
1995	RV James Clarke Ross	JCR 10
1996	RV Polarstern	ANT 13/4
1998	RV Polarstern	ANT 15/4 Dovetail
1999	RV James Clarke Ross	JCR 40 Albatross
2004-5	RV Polarstern	ANT 22/2 ISPOL
2006	RV Polarstern	ANT 23/3
2006	RV Polarstern	ANT 23/7 WWOS
2008	RV Polarstern	ANT 24/3
2009	RV Polarstern	ANT 25/4
2010-11	RV Polarstern	ANT 27/2
2013	RV Polarstern	ANT 29/3
2013-14	RV Polarstern	ANT 29/9

The ANT 29/9 (19 Dec 2013 - 05 March 2014) was exclusively focused on the Filchner Depression by RV-Polarstern. It has provided 350 samples with valid data from 62 stations. The region around the Filchner Trough Outflow is considered pivotal because large amounts of deep and bottom water in the Weddell Sea is formed. One of the objectives was to determine the basal melt rate under the Filchner Ronne Ice Shelf and therefore how much ISW is formed under the FRIS and how much ISW flows through the Filchner Trough to form WSBW. ANT 12/3 (1995) covered almost the same region and had a similar scientific focus. The rest of the expeditions are mainly focused on Weddell Transect, Prime-Meridian and ACC.

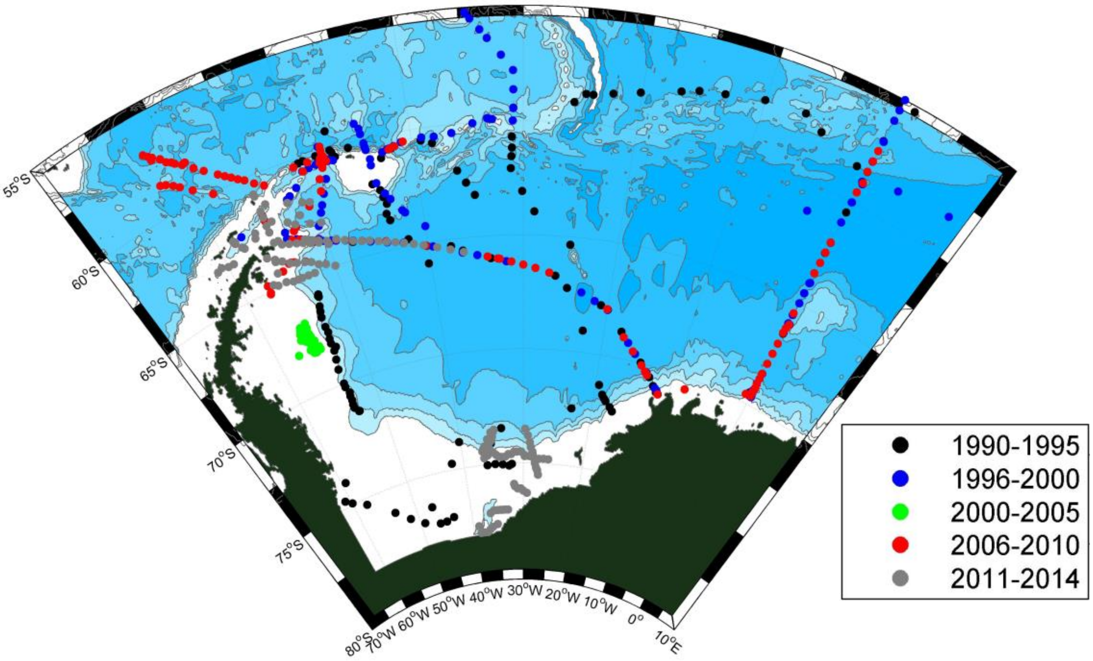

Figure 2.3.1 Map of stations consisting ^{4}He and Ne in reference of 5 years of interval in the Weddell Sea.

Among all the expeditions the ISW-1 and ISPOL are unique because the both were anchored on floating ice floes during the scientific measurement. The ISW-1 data has been taken from February 12 to June 4 in the year 1992; the ISW-1 covered an area roughly from 71.4˚S to 66.8˚S along 53˚W (see Figure 2.3.1) only contain ^{4}He, no Ne and not measured in Bremen. Previously, the observations from the ships were almost not available to the west of 53˚W in western Weddell region i.e. the western edge of the Weddell Gyre due to high concentration of perennial ice cover hindrance. One of the main objectives was to discover ocean processes in the western rim of the Weddell Sea in the formation of AABW (Gordon 1993). The data have 264 valid samples from 24 stations.

The ANT 22/2 (ISPOL) by RV-Polarstern from November 2004 to January 2005 provided 321 samples from 21 stations including several samples from helicopter deployed stations (providing no profiles but a single sample near the bottom). The stations from ISPOL are close to LIS (Hellmer et al. 2008). The heavy sea ice prevented the RV-Polarstern to go further southwest (Huhn et al. 2008). ISPOL can be assumed as the complementary to ISW-1 in the western rim of the Weddell Sea. The RV-Polarstern anchored an ice floe of 10km x 10km and approx. 2m thick second year ice. The drift took place over a uniform topography at ≈1500m isobath; however the depth decreased to less than 1000m at the end of the drift. A drift speed of less than 3km/day was observed, which is less than during other seasons i.e. ≈ 7km/day, reflecting the influence of northeasterly winds (Hellmer et al. 2008). Expedition ANT 29/3 (2013) is located nearest downstream to ISW-1 and ISPOL.

2.3.1 Noble Gas Measurements

Most of the NG measurement are carried out in IUP, Bremen Mass Spectrometric facility established in 1989 (Sültenfuss et al. 2009). The oceanic water samples are carefully transferred from Niskin Bottles to copper tubes. The copper tubes are air tight to avoid any air contamination. The dissolved air is then Ne is extracted by using Ultra High Vacuum (UHV) system before mass spectroscopy. The sample gases are transferred into a glass ampule through liquid nitrogen temperature. The NG isotopes (^{3}He, ^{4}He, ^{22}Ne) are separated by using Ultra High Vacuum (UHV) system and cooling traps to avoid contamination with other gasses and are finally measured by advanced UHV mass spectrometer. The measurements are frequently calibrated and corrected due to systematic errors of variations from a calibration standard. The data are calibrated according to an air standard. The error sources are measured by comparing duplicate sample. The measurement accuracy of ^{4}He is up to 0.01 nmol/kg or 0.5% and for Ne is 0.04 nmol/kg or 0.5%, and 0.2% for the $^{3}He/^{4}He$ ratio (Huhn et al. 2008). The Bremen Mass Spectrometric facility has capacity of 32 Helium sampling per working day (Sültenfuss et al. 2009).

3. Results and Analysis

3.1 Hydrographic and Noble Gases Distribution in the Weddell Sea

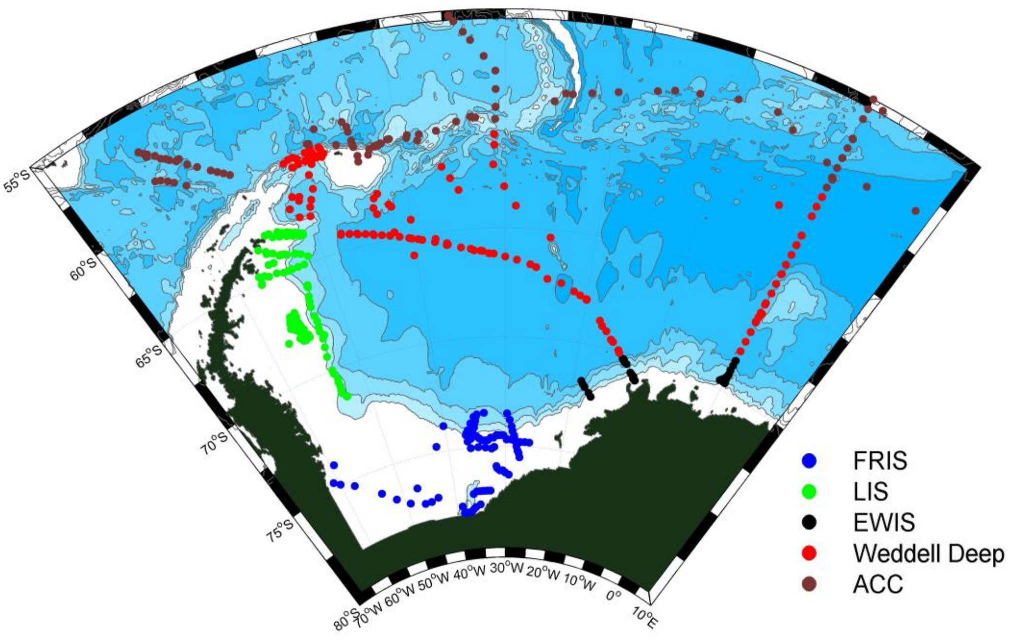

Figure 3.1.1 Map of the data stations in reference of their regional distribution in the Weddell Sea and ACC.

The figures below are derived from the data described in 2.3. The figures show the potential temperature (θ) against S, ^{4}He, Ne and δ^3He and the identified water masses are indicated.

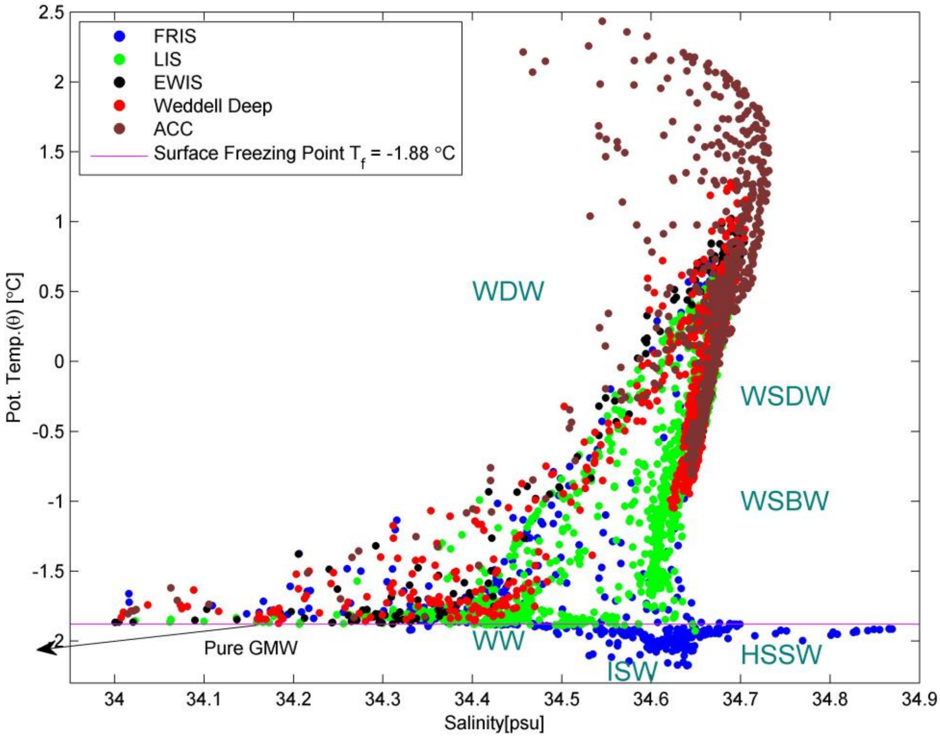

Figure 3.1.2 The θ-S plot with identified water masses of distributed regions in the Weddell Sea. The magenta horizontal line shows surface water freezing point. The black arrow points the pure GMW (θ=-91.08°C and S=0psu) expected existence.

The Figure 3.1.2 shows the characteristics of the identified water masses on the scale of θ and *S*. The surface freezing temperature is assumed -1.88˚C (solid horizontal magenta line in Figure 3.1.2 and in each of the following θ plots). The FRIS data (blue dots) have been obtained from ANT 12/3(1995) and ANT 29/9(2014) and both cover the Filchner Ice Shelf front. The Ronne Ice Shelf (RIS) front has data only from ANT 12/3(1995), it clearly shows the dominance of HSSW in the region with salinity exceeding 34.88. The salinity increase is largest in the upper 800m in FRIS water as most of the HSSW is formed along the RIS front. The HSSW undergoes a decrease of θ and Salinity, mainly caused by the GMW/ISW influx.

The FRIS shows prominent ISW due to sufficient sampling of stations in the Filchner depression. The ISW is sufficiently cold (θ=-2.3ºC) and shows that the ISW is formed by mixing of HSSW and basal GMW. The ISW is found at depth of 1100m and θ is clearly below -2.2ºC (see also Figure 3.2.2 (right) below).

The LIS water (green dots Figure 3.1.2) does not achieve the high salinity as the FRIS water, and the θ in LIS remains > -1.95ºC. The lower salinity in LIS water might be caused by less sea ice formation at LIS or by the increase of GMW formation due to increased entrainment of WDW or mWDW. However, the LIS stations location closer to the Weddell Gyre cannot be ignored. ISW (with $\theta < T_f$) in LIS water cannot be identified, considering the ISW has lost its presumed $\theta < T_f$ characteristic due to dilution with WDW or mWDW. The Weddell Deep water (red dots in Figure 3.1.2) might indicate that WSBW and WSDW are formed by mixing of WDW with ISW rather than with HSSW. At least the prominent salinity of HSSW is no longer present in the Weddell Deep WSDW and WSBW, whereas the LIS WSBW still has a little tendency towards slightly higher salinity.

In all data sub-sets the WDW's high salinities indicate its origin from CDW (Bulister et al. 2013). The WDW from the ACC provides the warmest water to the Weddell Sea and can be traced back to the high saline North Atlantic Deep Water (Foldvik & Gammelsrød 1988).

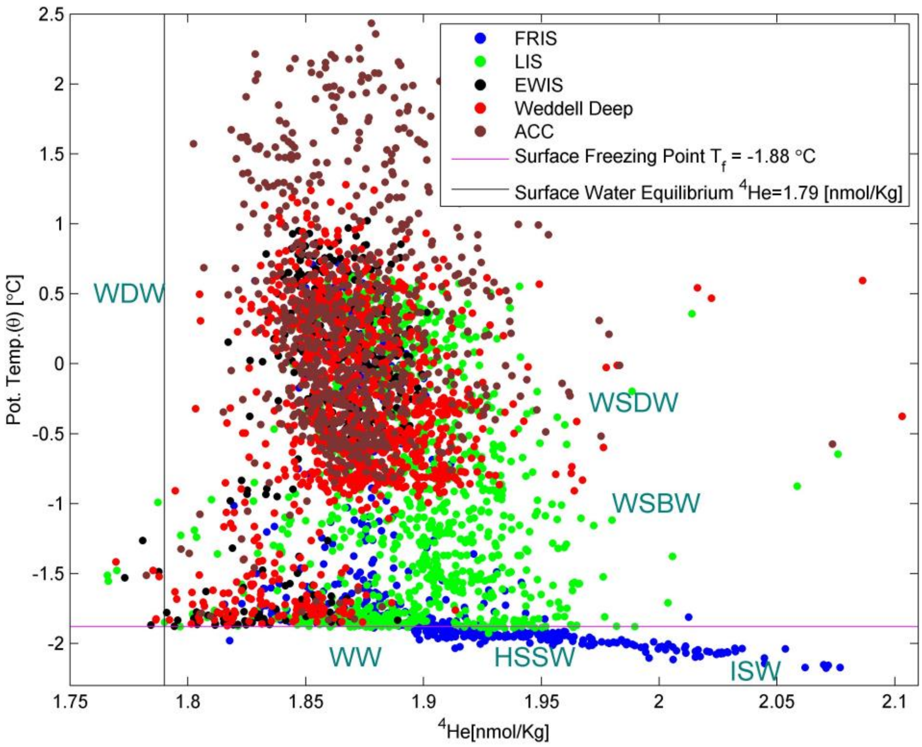

Figure 3.1.3 The θ-^{4}He plot with identified water masses of distributed regions in the Weddell Sea. The magenta horizontal line shows surface water freezing point. The black vertical solid line shows surface water equilibrium value of ^{4}He.

The high ^{4}He and Ne concentrations in FRIS water (blue dots Figure 3.1.3 & Figure 3.1.4) indicate the presence of a large fraction of GMW in ISW. The high ^{4}He and Ne concentrations in the LIS water (green dots) is due to the local ISW formation from mixing of GMW and mWDW as indicated by Huhn et al. 2008. Also the WSBW entrainment from FRIS may increase ^{4}He and Ne concentrations in the LIS region.

The WW in the Weddell Sea has average of has ^{4}He =1.85 nmol/kg and Ne = 8.24 nmol/kg (calculated from upper 200m data in the Weddell Sea, Figure 3.1.3 & Figure 3.1.4), which is higher than surface water equilibrium 1.79 nmol/kg and 8.05 nmol/kg (see 2.2) respectively. The WW is likely to have mixed with ISW from below and the resulting NG excess in the WW cannot equilibrate because of sea ice cover. The increased ^{4}He and Ne in WW might have also been induced by the wind over surface water. For instance, the Loose & Jenkins 2014 indicates wind induced Δ^4He up to 11.6% and ΔNe up to 8.8% provided wind speed of 10ms^{-1} for 25 days over surface water, such wind induced may cause false GMW presence in surface water in OMP analysis.

The HSSW should also have ^{4}He and Ne close to surface water equilibrium (similar as in WW), because it is generated by surface water freezing, but observations show even higher ^{4}He ≈1.90 nmol/kg (Figure 3.1.3) and Ne ≈1.95 nmol/kg (Figure 3.1.4) in HSSW than in than surface water equilibrium or even WW. One can interpret that the identified HSSW has lost its purity after mixing with overlying ISW that is recirculating on the southwestern shelf.

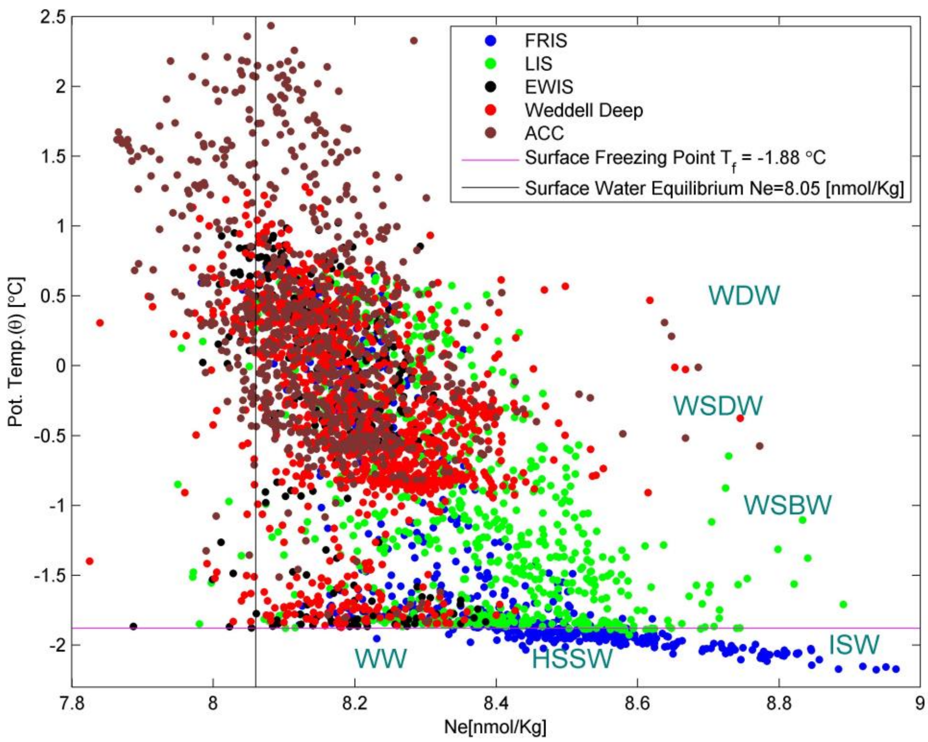

Figure 3.1.4 The θ-*Ne* plot with identified water masses of distributed regions in the Weddell Sea. The magenta horizontal line shows surface water freezing point. The black vertical solid line shows surface water equilibrium value of Ne.

The WDW is assumed to be free of GMW due to its source outside the Weddell Sea. Indeed it shows consistent lower values of ^4He and Ne (Figure 3.1.3 & Figure 3.1.4) close to the ^4He and Ne surface water equilibrium value. However, ^4He values (not Ne) in WDW are also slightly higher than the surface water equilibrium in ACC water. The increase is explained as the addition of Helium (mainly mantel or primordial ^3He and also ^4He) from hydrothermal vents in the Pacific. This primordial source can be identified by the high δ^3He (see below Figure 3.1.6; note that +8% δ^3He from hydrothermal vents also imply +1% Δ^4He but no ΔNe). Since the Ne has no additional source unlike ^4He, ACC water lies close to the surface equilibrium value of Ne (Figure 3.1.4). The WSBW shows intermediate concentrations of ^4He and Ne because the ISW high in ^4He and Ne mixes with WDW low in ^4He and Ne. After FRIS and LIS, the Ne concentration steadily decreases in EWIS, Weddell Deep and ACC.

To remark clearly: The presence of ISW or GMW in the above θ-S plot (Figure 3.1.2) is not visible (except for FRIS water), because the addition of super-cooled and low saline GMW or ISW into other water masses is mixed away towards lower salinities and moderate temperatures. We need parameters that make GMW/ISW prominent in the other water masses. The θ-^4He and θ-Ne correlations are in a way different from the θ-S plot, and hence, the θ-^4He and θ-Ne clearly show the presence of ISW (high in ^4He and Ne), making it distinguishable from the other water masses (generally low in ^4He and Ne).

Whereas the Figure 3.1.3 (θ-^4He) and Figure 3.1.4 (θ-Ne) might suggest that ^4He and Ne provide rather similar information, the θ-^4He/Ne plot below Figure 3.1.7 demonstrates clearly that ^4He and Ne provide complementary information. The significant difference of the ^4He and Ne information is caused by

- the different solubility of ^4He and Ne at different temperatures (Weiss 1971),
- a fractionation of ^4He and Ne when the atmospheric gas composition is trapped in the glacial ice matrix (Loose & Jenkins 2014),
- the ^4He addition from external sources, such as crustal ^4He from the bedrock and primordial ^4He from hydrothermal vents from the deep Pacific into ACC water.

The distribution of FRIS, LIS, Weddell Deep and ACC water masses are represented in the schematic in θ-S (left) and θ-^4He (right) plots in Figure 3.1.5. The schematic distribution is derived from the highest and lowest values of θ, S and ^4He for each of the sub-region. The EWIS is not included in the schematic distribution due to its quite resemblance with Weddell Deep in its θ, S and ^4He values.

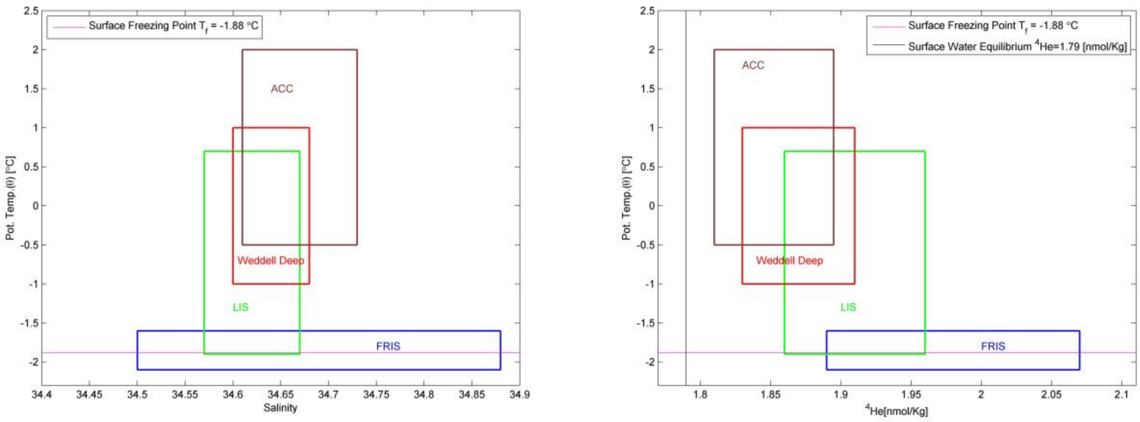

Figure 3.1.5 Schematic positions of the ACC, FRIS, LIS and Weddell Deep in θ-S (left) and θ-*He* (right) plots. The magenta horizontal line shows surface water freezing point. The black vertical solid line shows the surface water equilibrium value of ^{4}He (right). The EWIS is not added to the plots due to its close exposure to the CDW and quite resemblance to the Weddell Deep.

The WDW shows highest values of θ and δ^{3}He (Figure 3.1.6). The ACC water leads all of the other sub-region waters in θ and δ^{3}He because its dominant water mass, the Circumpolar Deep Water is the warmest in the Weddell Sea region as compared to all other sub-regions. The high δ^{3}He ratio in Circumpolar Deep Water (CDW) is caused by entrainment of Pacific deep water affected by hydrothermal vents and is the source of the WDW in the Weddell Sea. The ^{3}He isotope can be assumed a ‘primary characteristic’ of the WDW in the Weddell Sea. The δ^{3}He is found nearly zero and even lower than surface equilibrium value (δ^{3}He =-1.8% at θ=-1.88ºC) in the cold shelf water (FRIS and LIS). The lowest δ^{3}He measured is -3.70% in FRIS.

The δ^{3}He addition into Pacific deep water and its entrainment into WDW through CDW give it a positive correlation with θ (shown as dark brown line in Figure 3.1.6). However the δ^{3}He in ISW shows also a correlation with θ, but the slope of that correlation is clearly different (shown as blue line in Figure 3.1.6). The different ISW’s δ^{3}He and θ correlation and its lower δ^{3}He anomaly are caused by the increase of ^{4}He (hence reduced ^{3}He/^{4}He ratio) in the local ISW. The bedrock on which the glaciers rest and slide provides addition of ^{4}He from the decay of uranium present in the earth crust. Therefore, the older the age of glaciers the more ^{4}He the glacial ice will accumulate, thus, a higher negative δ^{3}He in ISW can be observed.

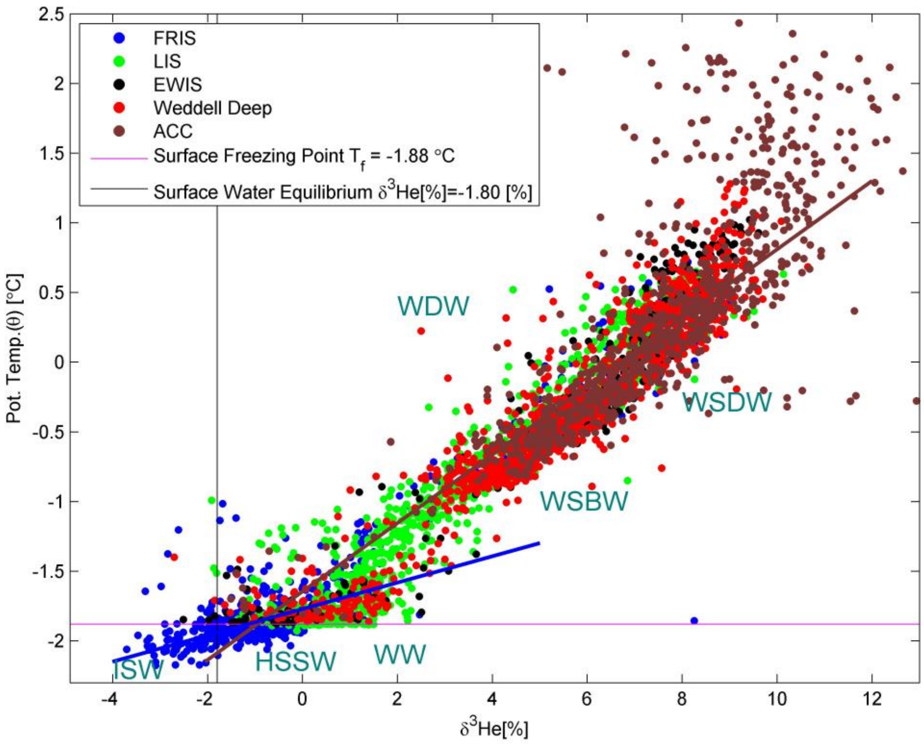

Figure 3.1.6 The θ-δ^3He plot with identified water masses of distributed regions in the Weddell Sea. The magenta horizontal line shows surface water freezing point. The black vertical solid line shows surface water equilibrium value of δ^3He. The dark brown line represents the slope of ACC data and blue line represents the slope of FRIS data.

The Figure 3.1.7 mainly reflects the solubility differences of ^{4}He and Ne at different temperatures. Ne is more soluble than ^{4}He for cold temperatures. So, one would expect a decreasing ratio with decreasing temperatures. The cold surface water ^{4}He/Ne value of 0.222 (black solid line) is derived from the previously mentioned ^{4}He=1.79 nmol/kg and Ne=8.05 nmol/kg equilibrium concentrations in surface water. The dynamics of meteoric ice with air bubbles trapped into and its ultimate release through basal melting into ocean water (see 1.1) would suggest persistent equilibrium of the ^{4}He/Ne ratio in the ocean water. But, the Δ^4He/ΔNe ratio for pure GMW is 1.43 (i.e. higher to ^{4}He/Ne value of 1.41 in atmospheric air), thus indicates the more ^{4}He in pure GMW from some additional sources or/and depletion of Ne in glacial ice due to differential diffusion (less than 1% decrease of Ne in GMW according to Loose & Jenkins 2014). Hence, particularly FRIS shows exceptionally higher ^{4}He/Ne ratio.

The pure crustal ^{4}He addition cannot be calculated or predicted, because it depends on the time the glacial ice from that the GMW was melted had rested on the bedrock. So far unpublished sub-ice-shelf measurements indicate an addition of up to 4% crustal ^{4}He in certain locations below Filchner Ice Shelf (O. Huhn, personal communication, unpublished data). ACC water has also higher ^{4}He/Ne ratio due to the addition of primordial ^{4}He. According to (Hohmann et al. 2002), the atmospheric

^{4}He component can be distinguished from the volcanic and crustal ^{4}He component by using Ne. An extrapolation of ISW of FRIS in Figure 3.1.7 would lead to pure GMW's ^{4}He/Ne=0.309 at -91.08ºC.

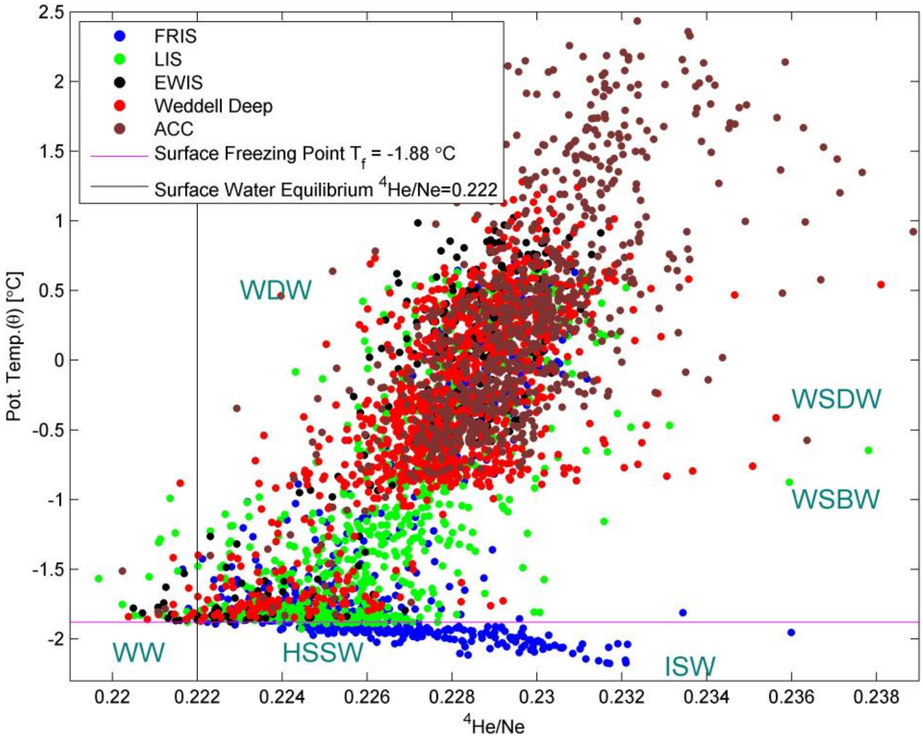

Figure 3.1.7 The θ-^{4}He/Ne plot with reference of surface freezing point and surface water ^{4}He/Ne value of distributed regions in the Weddell Sea. The magenta horizontal line shows surface water freezing point. The black vertical solid line shows surface water equilibrium value of ^{4}He/Ne ratio.

The Figure 3.1.8 is the cross validation of Figure 3.1.7 which shows how much additional ^{4}He is added to ACC water and to FRIS water from the different sources. The FRIS (Figure 3.1.8) shows a higher ^{4}He/Ne ratio with increase of Ne as positive correlation (the blue solid line). As Ne has no additional source except air therefore increasing of ^{4}He/Ne ratio with Ne increase in shelf water indicates crustal ^{4}He addition and/or the solubility differences of ^{4}He and Ne as a function of θ and salinity. According to Hohmann et al. 2002, the atmospheric ^{4}He component can be distinguished from the volcanic and crustal ^{4}He component by using Ne.

The pure GMW's ^{4}He/Ne (0.309) is higher than the surface water ^{4}He/Ne ratio (0.222). This also demonstrates the role of fractionation and the different solubility of ^{4}He and Ne as a function of θ and salinity. Since the pure GMW is colder and fresher than the surface water therefore acquire more capability under higher hydrostatic pressure to dissolve more ^{4}He than that of surface water, the Figure 3.1.8 shows increases of ^{4}He/Ne ratio in FRIS water with increase of Ne that gives it a positive correlation (the blue solid line), hence, a rise of 4.5% of ^{4}He (crustal ^{4}He is the largest expected source) in the FRIS water is observed due to addition of basal GMW as compared to surface water ^{4}He/Ne equilibrium value.

The ACC (Figure 3.1.8) show decrease of ^{4}He/Ne ratio with increase of Ne as a negative correlation (the brown solid line) due to primordial ^{4}He but no Ne in ACC water. The ACC ^{4}He/Ne ratio decreases up to 0.226 with increase of Ne. The ACC warm water is more affected by the ^{4}He addition, from hydrothermal vents and volcanic activities; hence the ratio is shifted 5.4% due to addition of ^{4}He.

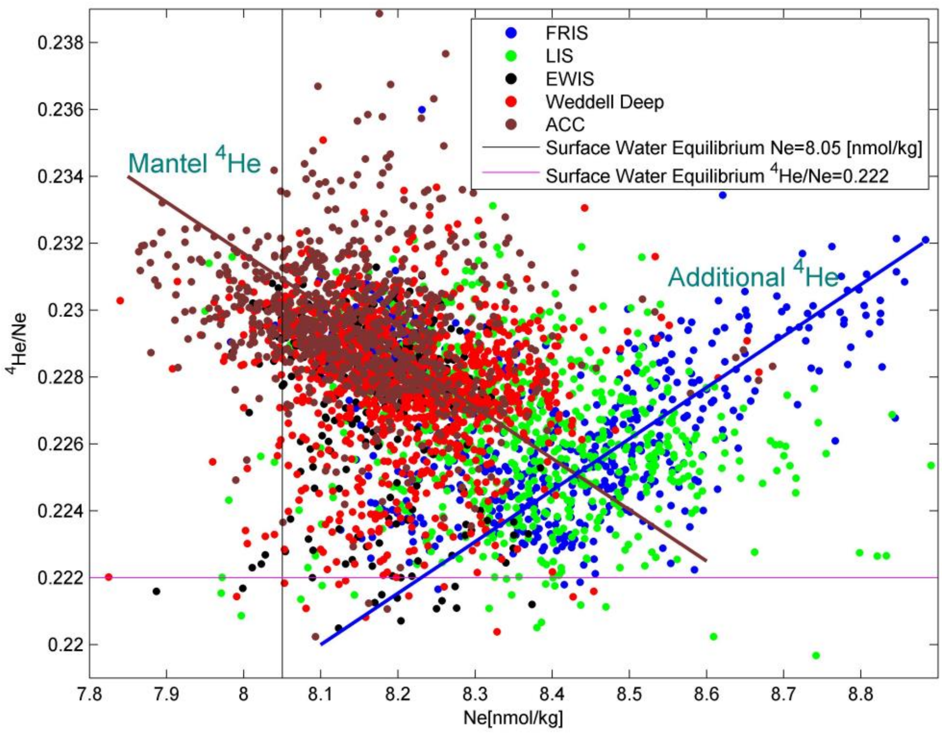

Figure 3.1.8 The ^{4}He/Ne-Ne plot with reference of surface Ne and surface water ^{4}He/Ne value in distributed regions of Weddell Sea. The magenta horizontal line show Surface Water freezing point. The black vertical solid line shows Surface Water Equilibrium value of ^{4}He/Ne ratio. The blue solid line represent slope of FRIS data and brown solid line represent slope of ACC/FRIS indicating additional ^{4}He addition.

3.2 Parameters and Water Mass Distribution in Bottom Layer

The maps below are presenting the parameters (θ, S, ^{4}He, Ne and δ^3He anomaly) and the calculated water masses (WW, WDW, HSSW and GMW fractions in percent derived by the OMP method) in the bottom layer (i.e. within the lowest 50m). The spreading of the dense water masses, i.e. the GMW on which we focus and its parent water mass HSSW (see Figure 3.1.2), occurs mainly in the bottom layer. However, later (section 3.3) we will also regard the upper layers by discussing selected vertical subsections in the area of investigation.

To create the maps, the irregularly distributed values had to be interpolated on a regular grid. The parameter values and water mass fractions are interpolated within longitude and latitude using an ‘objective mapping’ algorithm provided by M.Visbek (http://mooring.ucsd.edu/software/matlab/doc/toolbox/datafun/obana.html). The longitude and latitude spacing 0.5º and 0.12º, the interpolation (gaussian) radius and a cutoff radius have been chosen to compromise between desired resolution and data coverage (i.e. to avoid interpolation gaps). Empty white areas in the maps lack data also in a far distance and are therefore accepted in order to maintain the resolution of the interpolation for the areas covered with data.

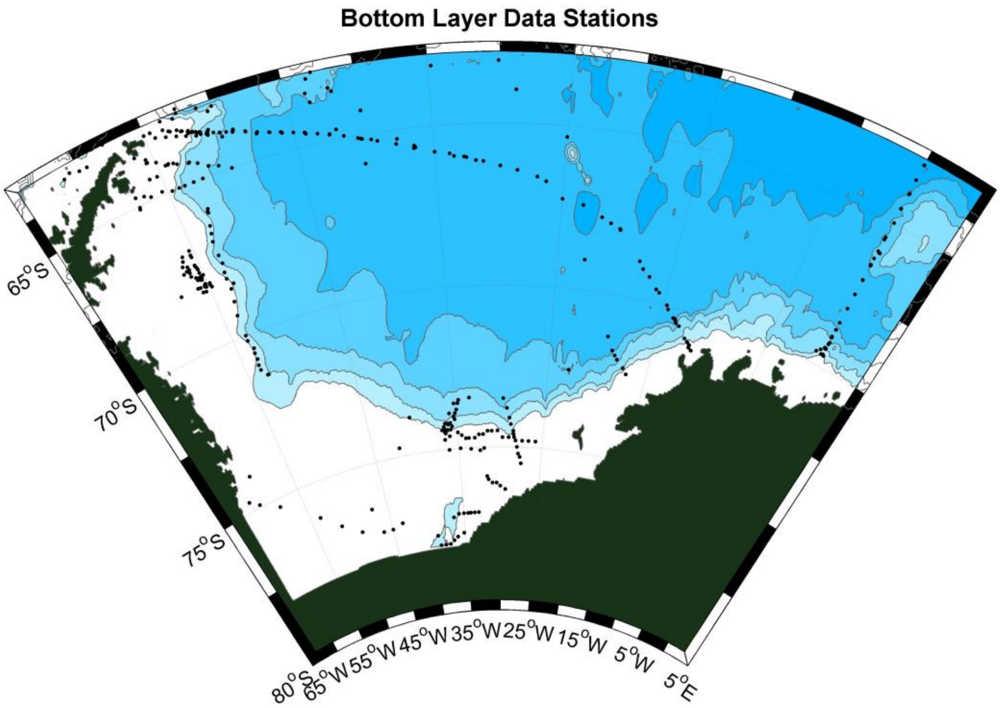

Figure 3.2.1 The data for the bottom layer (50m) maps of the parameters and the calculated four water masses, the black dots are the stations in the Weddell Sea used in the interpolation.

The region Fimbul Ice Shelf and Maud Rise at Prime Meridian shows the warmest bottom layer compared to all others of the Weddell Sea Ice Shelves and shows a temperature above 0ºC in the Potential Temperature (θ) map Figure 3.2.2 (left). That indicates the major inflow of WDW into the Weddell Sea through the Weddell Gyre from the east. The θ map clearly shows the LIS bottom layer below -1.3ºC, the FRIS bottom layer below -2ºC is even colder than the LIS bottom layer. A strong gradient of θ can be observed on the slope in front of the Filchner Depression.

The Filchner Slope is identified as the junction where most of cold FRIS water is expected to be mixing with WDW. Hence, most of the WSBW is expected to form here and adds to the bottom layer of Weddell Gyre. The gradient of θ in front of LIS is not as strong as in front of FRIS, probably because the LIS bottom layer is not as cold as FRIS bottom layer, or simply because we do not have a section of stations in front of LIS down the slope as we have on the Filchner Slope. The Weddell

Basin along Weddell Transect is found to be -0.8ºC, thus indicating the presences of WSBW (θ<-0.7 ºC) possibly flowing out of the Weddell Sea or recirculating in the Weddell Basin.

The salinity map Figure 3.2.2 (right) demonstrates the northwestern RIS as the highest saline 34.88psu bottom layer in the Weddell Sea. The salinity decreases from RIS to FRIS from 34.88 to 34.68psu. The LIS bottom water layer is measured around 34.62psu. The Weddell Basin shows almost 34.65psu throughout in its bottom water.

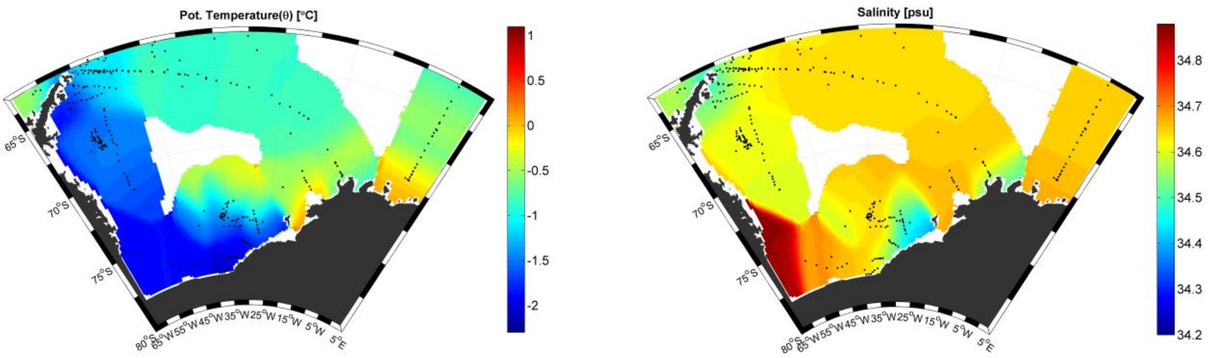

Figure 3.2.2 Potential Temperature (θ) (left) and Salinity (right) bottom layer (50m) maps in the Weddell Sea, the black dots are the stations in the Weddell Sea used in the interpolation.

The ^4He map (Figure 3.2.3 left) shows its maximum of 2.02 nmol/kg and the Ne map (Figure 3.2.3 right) shows its maximum of 8.80 nmol/kg in the FIS bottom layer. ^4He and Ne concentrations show a rapid decrease over the Filchner slope and decline to 1.92 nmol/kg and 8.50 nmol/kg respectively at almost 74ºS, 25ºW. The LIS does not show as high ^4He and Ne concentrations as FRIS (specially compared to the values at FIS front), however $^4He \approx 1.95$ nmol/kg and Ne ≈ 8.55 nmol/kg can be observed in the bottom layer at LIS front, significantly higher than the other areas. The ^4He and Ne on the LIS slope could be generated by a flow from the Filchner Slope to LIS in the bottom layer but due to lack of data between the two regions undermines the interpolation between these regions and does not indicate such a flow along the slope in the bottom layer from FRIS to LIS.

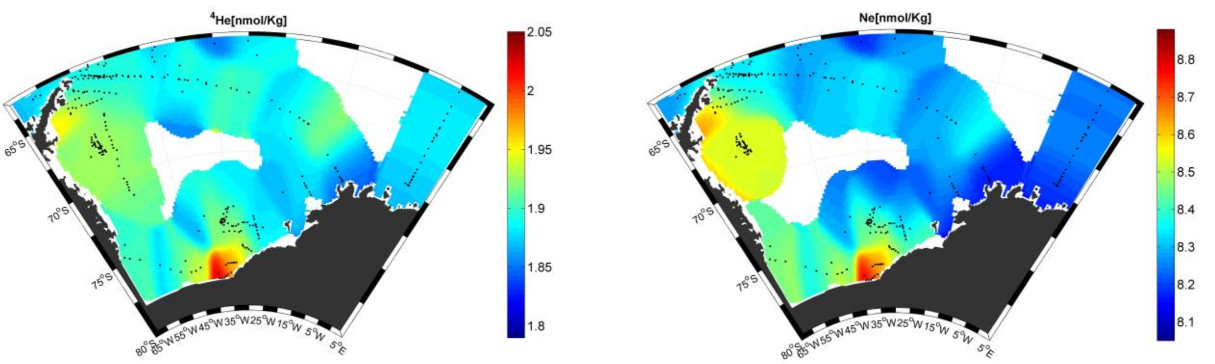

Figure 3.2.3 The ^4He (left) and Ne (right) bottom layer (50m) maps in the Weddell Sea, the black dots are the stations in the Weddell Sea used in the interpolation.

The northern edge of LIS at 65ºS shows exceptionally high ^{4}He and Ne of about 1.95 nmol/kg and 8.60 nmol/kg respectively. Therefore, it can be concluded that a local water mass high in ^{4}He and Ne originated from LIS is flowing from the northern edge of LIS than from the LIS front.

The δ^3He map Figure 3.2.4 (left) resembles the WDW circulation from the ACC. The Prime Meridian continental slope has the highest δ^3He ≈ 7% in the bottom layer, and can be assumed as influenced by the WDW pathway from the ACC into the Weddell Sea through the Weddell Gyre. The δ^3He is extremely low in all other shelf bottom layers, particularly at FRIS, because of the low influence of WDW onto the southwestern shelf. The WDW Figure 3.2.4 (right) in the bottom layer is observed highest with 70% at the Prime Meridian at the continental slope. In the deep Weddell Basin bottom layer WDW of around 45% is found along the Weddell Transect. The WDW at the FRIS is the lowest measured i.e. below 10% probably due to the shallow shelf water topography and location of the FRIS front far away from the Filchner slope and shelf break. The LIS shows 20% WDW, a bit higher than FRIS.

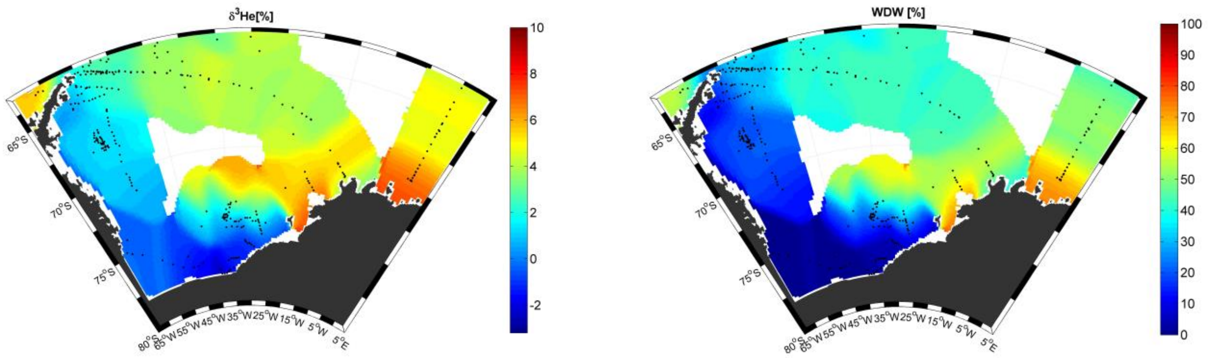

Figure 3.2.4 The δ^3He (left) and WDW (right) bottom layer (50m) maps in the Weddell Sea, the black dots are the stations in the Weddell Sea used in the interpolation.

The WW in the bottom layer of the Weddell Basin is as expected low (around 10%) in Figure 3.2.5 (right). The WW in FRIS and LIS bottom layers is also below 20%, the WW is up to 40% only in the shelf water at 75ºS, 20ºW. This WW maximum coincides with the salinity minimum seen in the Salinity map (Figure 3.2.2), which could be caused by the lowest salinity value measured (34.0psu) from the data assigned to WW in Table 1. This salinity minimum might have been caused by less sea ice formation or strong local sea ice melting at that location, which is shallow and apparently isolated from the Weddell Sea general circulation.

The highest salinity in the shelf water is induced by the coastal polynyas mostly produced at the northwestern edge of RIS (S > 34.88 psu, see salinity map). Such a high salinity is related to the formation of HSSW. Indeed, nearly 100% HSSW computed by the OMP can be observed in the region Figure 3.2.5 (right). The HSSW is then expected to disperse northward towards LIS (60% to 70 %) and flows also into the Ronne Depression, where it mixes with inter cavity water. The FIS front shows around 80% HSSW. The decline of -20% of HSSW from RIS to FIS bottom water outflow can be regarded as HSSW mixing with mWDW and WW (before entering the RIS) and GMW (after entering the RIS). The HSSW decreases fast on the Filchner slope and is below 50% in the deep basin. The Weddell Basin bottom layer is around 50% HSSW along the Weddell Transect.

Therefore we can assume that most of the HSSW (originated in southwestern shelves water) flow across the Weddell Transect. The EWIS at the Prime Meridian and further east of it lack HSSW, even if high saline (and warm) water is found at the Prime Meridian (see above Figure 3.2.2), originating from high saline NADW (Foldvik & Gammelsrød 1988).

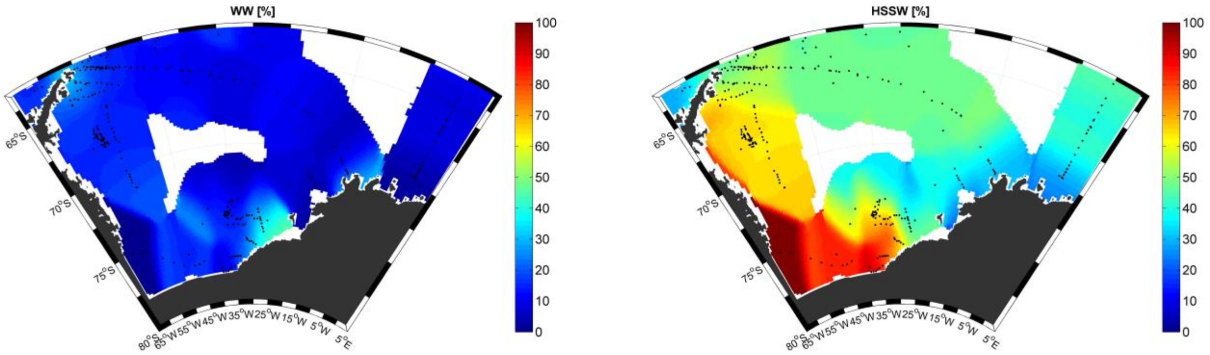

Figure 3.2.5 The WW (left) and HSSW (right) bottom layer (50m) maps in the Weddell Sea, the black dots are the stations in the Weddell Sea used in the interpolation.

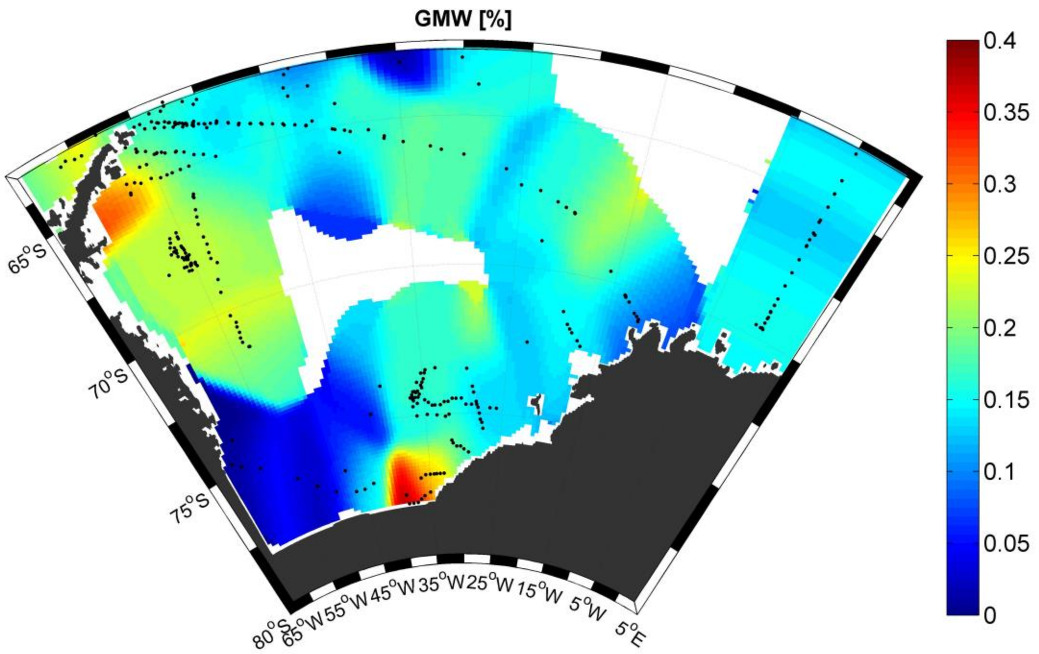

Figure 3.2.6 The GMW bottom layer (50m) map in the Weddell Sea, the black dots are the stations in the Weddell Sea used in the interpolation.

The GMW maximum of 0.37% is clearly spotted in the FIS bottom water outflow from Filchner Trough (Figure 3.2.6). The GMW from FIS decreases fast in the bottom layer of the Filchner

Depression towards the north (0.15%-0.2%). The southern edge of LIS front at 70ºS shows a sudden appearance of the GMW ≈ 0.25%. The GMW flow between these two shelf region cannot be traced in the bottom layer map due to the lack of data (low values of GMW on the shelf between the FRIS and LIS region aren based on a single station only).

However, GMW is assumed to disperse from the Filchner Slope to the LIS slope and mix with local LIS GMW plume as we will show below in the discussion of ISW1-Figure 3.4.2. A prominent GMW plume detected at 65ºS, 56ºW in front of the former Larsen Ice Shelf A may indicate locally formed WSBW (θ<-0.7 ºC see θ map) and will be cross-verified from the further analysis in Figure 3.4.3 analysis. The GMW in the inner Weddell Basin seems to cross the Weddell Transect to the north and east into the ACC.

All the discussed parameters and water masses in the bottom layer do clearly show their spatial distribution and formation region and project their pathways in the Weddell Sea. The WDW transported within the Weddell Gyre makes its way into the Weddell Sea largely through the passage between Fimbul Ice Shelf (EWIS) and Maud Rise. The WDW (or mWDW) faces FRIS water high in GMW at the Filchner Slope and causes the most of the earth’s cold bottom water formation. The FRIS front and Filchner Depression have in their bottom layer negligible influence from the Weddell Gyre’s warm water. Further downstream, the Weddell Gyre transports the local GMW of FRIS to the LIS region, where it further mixes with the LIS’s WSDW/WSBW.

3.3 The Filchner Ronne Ice Shelf (FRIS) Sections.

In the following selected sections of the parameters and the OMP based water masses are used to investigate their local vertical variations, distribution and spreading. As a result, a general circulation of the water masses could be established.

The irregularly distributed sections’ parameter values and water mass fractions are interpolated within longitude/latitude (horizontal) and the depth (vertical) using the same ‘objective mapping’ algorithm as for the maps above (Chapter 3.2). The horizontal spacing typically varies from 0.5º to 0.01º depending on the horizontal scale of the section. The vertical spacing varies from 10m to 100m. The interpolation (gaussian) radius for the horizontal, vertical interpolation and cutoff radius have been set depending on the number and distribution of the available data points. A smaller number of available data points would need larger radius to avoid gaps in the interpolated fields, a higher number of data points allow on the other hand smaller radius and thus a higher spatial resolution.

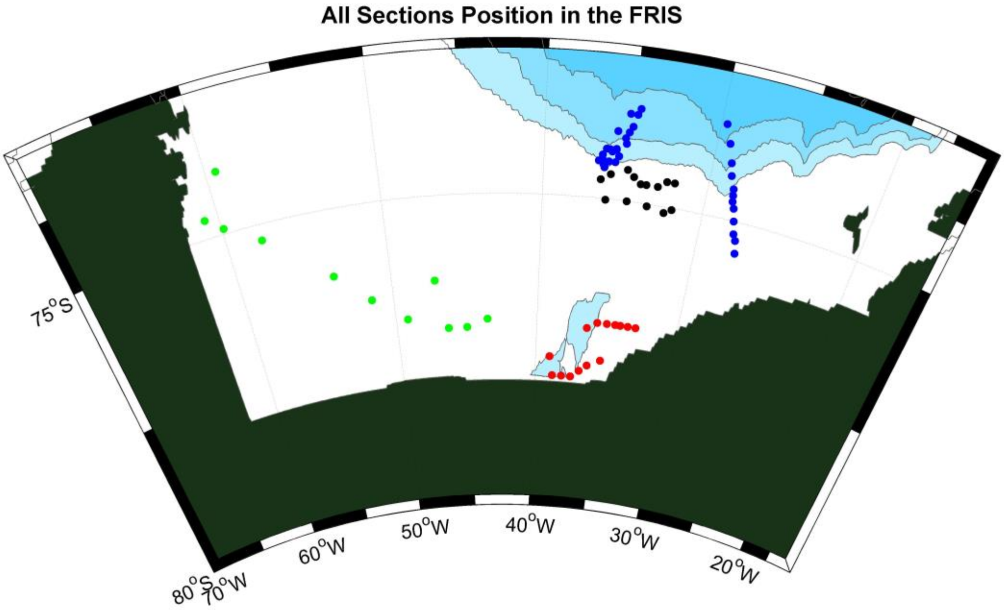

Figure 3.3.1 The map including the sections close to the FRIS. The Sections in red, black and blue are compared to each other whereas the green ones are analyzed separately.

3.3.1 The Ronne Ice Shelf (RIS) Section

The θ section in Figure 3.3.2 shows two minima below -2ºC below 150m depth at both edges of the section (the same positions where GMW is high, see Figure 3.3.2), θ is slightly higher around -1.5ºC at 53ºW probably due to presence of mWDW.

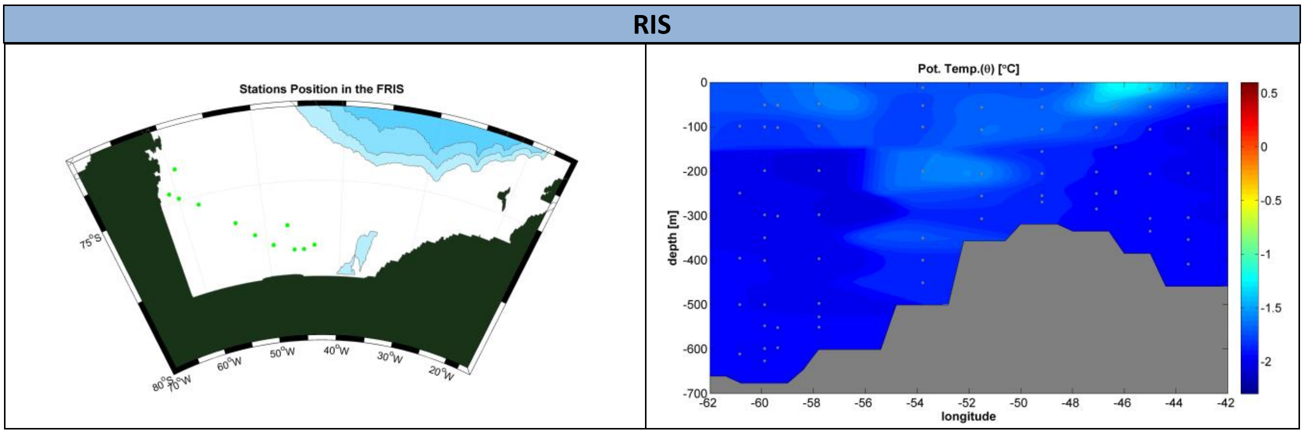

Figure 3.3.2 (continued) The sections map and the parameter θ in the Ronne Ice Shelf (RIS) at located stations in the map.

The salinity section in Figure 3.3.2 shows very high salinity of 34.8psu at 400 to 650m depth at the western edge of RIS and a decrease towards the eastern edge of around 34.6psu probably due to mixing with WW or GMW. The δ^3He is around 1% (above surface equilibrium -1.8%) in 200m at

53ºW, indicating the presence of mWDW (WW+WDW). The δ^3He is substantially reduced from west to east, possibly due to GMW addition with relative higher ^{4}He at the eastern edge.

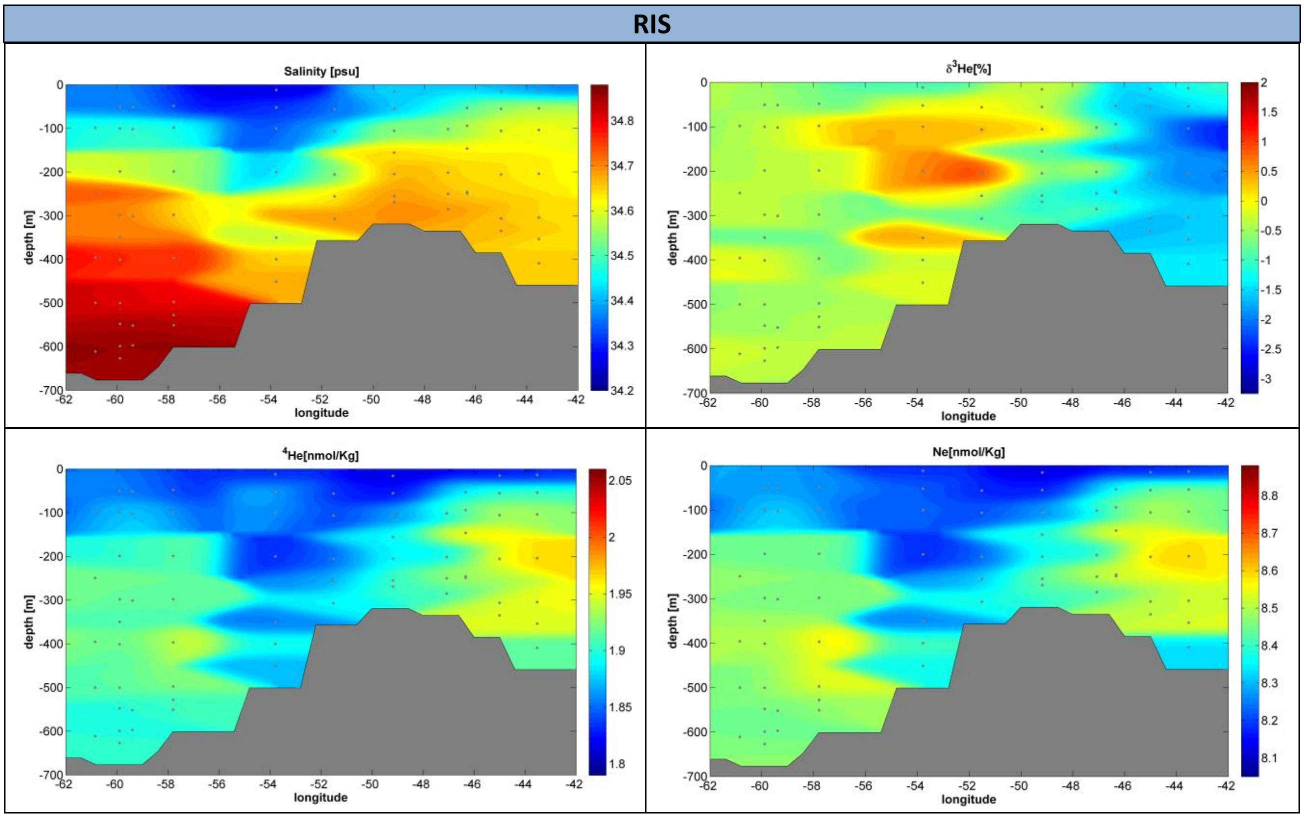

Figure 3.3.2 (continued) The sections of Salinity, δ3He, He and Ne in the Ronne Ice Shelf (RIS) at located stations in the map.

The ^{4}He and Ne sections in Figure 3.3.2 have highest ^{4}He =1.96 nmol/kg and Ne = 8.60 nmol/kg at the eastern edge of RIS from 200m depth to bottom and support the assumption of GMW addition. At the western edge from 200m to the bottom, the ^{4}He is around 1.92 nmol/kg and Ne is around 8.55 nmol/kg, therefore, we can assume an increase of GMW from the western to the eastern edge of RIS or a decrease from east to west.

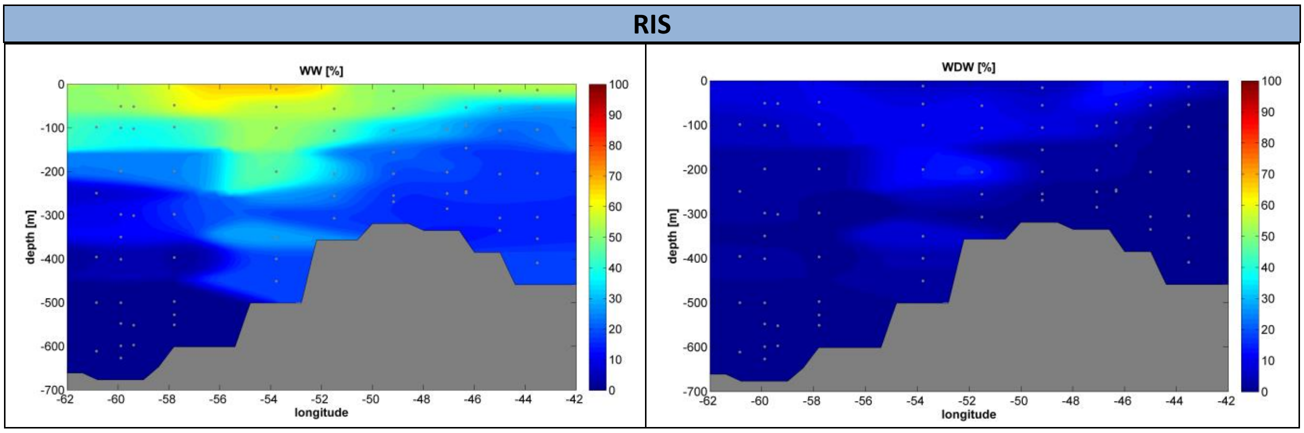

Figure 3.3.2 (continued) The sections of WW (left) and WDW (right) in the Ronne Ice Shelf at located stations in the map.

The WW is up to 60% in the surface water at 54ºW. Below, it declines, possibly, due to mixing with WDW to form mWDW in 100m to 200m depth at 54ºW and underlying HSSW. At the same position we had observed a weak signal of δ^3He of about 1% (Figure 3.3.2). Therefore, the WDW has negligible influence on the section except a weak mix with WW in the surface water at 54ºW. WDW is found nowhere above 15%.

The HSSW section shows the HSSW maximum in the depth below 500m at the western edge of RIS (around 60ºW i.e. in the Ronne Basin) as we have already seen in the salinity section above. The origin of the HSSW is the polynya along the northwestern RIS front. The HSSW (100%) with around 34.88psu may move through the Ronne Depression into the RIS cavity and cause basal melting under the RIS and FRIS.

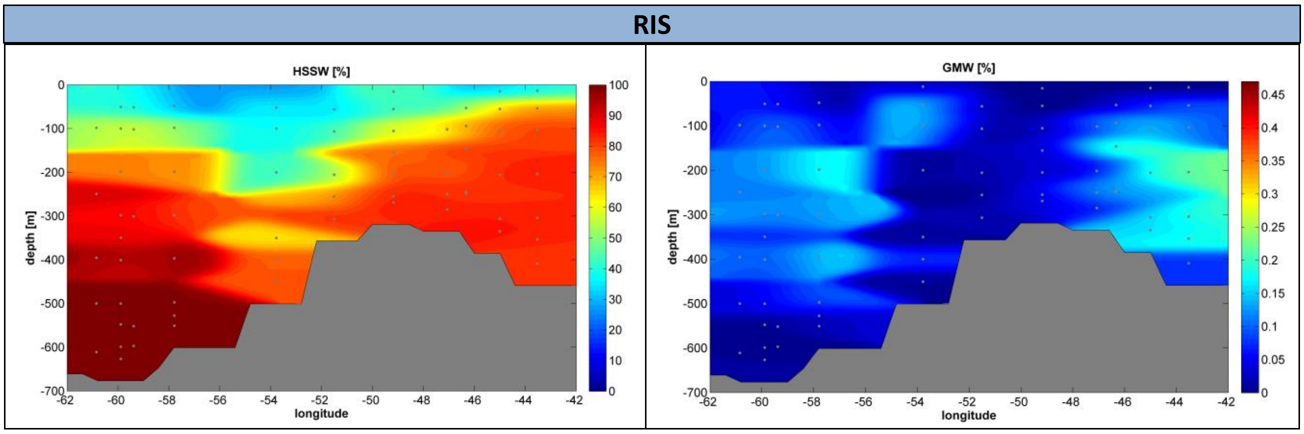

Figure 3.3.2 The sections of HSSW and GMW in the Ronne Ice Shelf at located stations in the map.

The mixing of HSSW and GMW in the ice shelf cavity forms comparatively low saline and less dense ISW. Mixing of HSSW with mWDW and the ISW recirculation in the Ronne Depression might have caused a decrease of HSSW in 200m to 400m at 58ºW. Thus, the formation, up rise and stratification of ISW above HSSW is clear. This ISW rises because it is less saline and might sink again into the cavity by further mixing with mWDW and/or HSSW. Thus, we assume an inter-cavity circulation pattern in the Ronne Depression, which can be identified from some small patches of GMW in the upper 400m depth from 60ºW to 56ºW. The ISW would recirculate in the cavity until its salinity is low enough to stratify over the HSSW. The ISW in the RIS cavity would also rise further up and circulate in the RIS cavity from west to east. The highest GMW observed in the section is 0.25% at the eastern edge of RIS. The increase of GMW fraction from the western edge to the eastern edge is probably due to receiving a GMW feedback from the FIS (along the Filchner Depression) outflow.

3.3.2 The Filchner Ice Shelf (FIS) FIS77 and FIS78 Sections

In the two FIS sections in Figure 3.3.3, (the left column FIS78 in close distance to the ice shelf front, the right column FIS77 is 91 km further north) the formation and dynamics of GMW is further investigated and compared the RIS sections (Figure 3.3.2). The two FIS sections in Figure 3.3.3 are the eastern extension of the RIS section and show FIS and the Filchner Depression as the main passage of GMW. There may be temporal changes involved, when the RIS section is compared to the FIS sections because the RIS section consist data from ANT 12/3(1995) and the FIS sections consist data from ANT 29/9(2013-14).

FIS78	FIS77
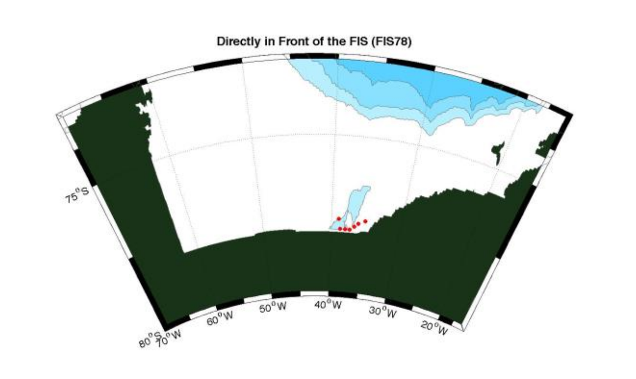	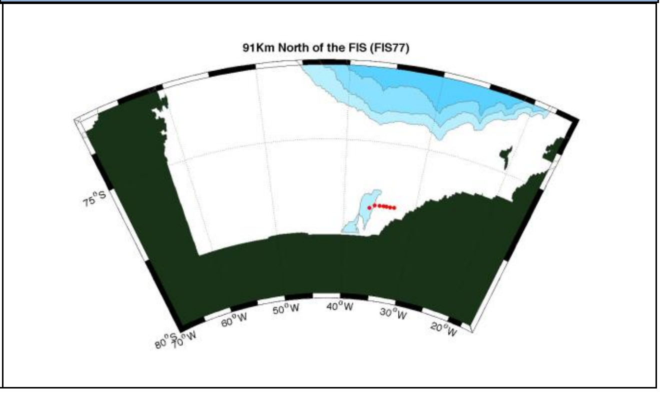

Figure 3.3.3 (continued) The sections stations map FIS78 (left) directly in front Filchner Ice Shelf and FIS77 (right) 91Km north of FIS78 as shown in red dots in the maps.

The θ in section FIS78 (Figure 3.3.3 left) is substantially low around -2.3ºC at similar position where high ^{4}He, Ne and GMW (FIS78) are located (see below Figure 3.3.3). θ in FIS77 is at its minimum of around -2ºC in 600m depth at 34.5ºW. The θ of surface water is below -1.5ºC and decreases with depth.

The salinity section (FIS78) shows 34.65psu below 1000m at 37ºW and the low salinity of 34.20psu is observed in the surface water at the similar longitude. The salinity section (FIS77) shows that the salinity of the surface water is low around 34.30psu and increases with depth up to 34.67psu at 36.5ºW. In the bottom layer, the salinity of FIS78 is a little bit lower than further northward in FIS77.

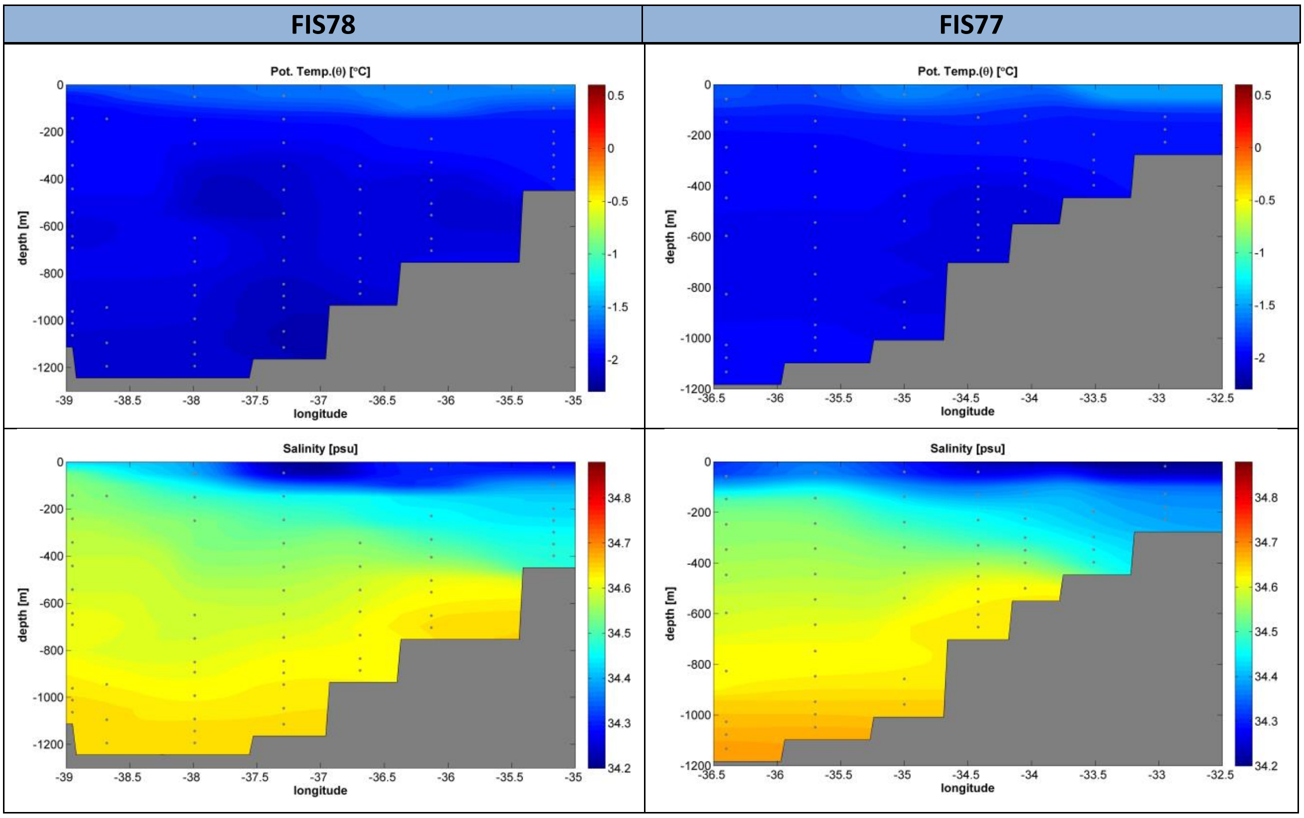

Figure 3.3.3 (continued) The sections of θ and salinity in front of the Filchner Ice Shelf at located stations in the maps.

The FIS78 δ^3He (Figure 3.3.3) is substantially low. It is slightly below 0% down to 400m depth and then decreases with depth down to -3.25% at 37.5ºW in 1100m depth. δ^3He below 400 m is higher in FIS77 (≈ -1.5%) than in FIS78 (< 2.0%). The highest ^{4}He of 2.05 nmol/kg and Ne of 8.88 nmol/kg are observed in the depth of 800m to 1100m at 37ºW in respective FIS78 sections. In FIS77 the maximum ^{4}He is 1.98 nmol/kg and Ne at 8.75 nmol/kg in the depth of 400m to 800m at 34.5ºW.

From the sections (θ, S, ^{4}He) two ISW core (i.e. HSSW+GMW; θ < -2.19ºC, S > 34.60 and ^{4}He > 1.98 nmol/kg as defined by Schlosser 1986) can be identified in FIS78, one in1000m depth at 37ºW and a second ISW core at in 600m depth 35.5ºW. This second ISW core (FIS78) can also be identified in FIS77 at 34.5ºW in 600m depth.

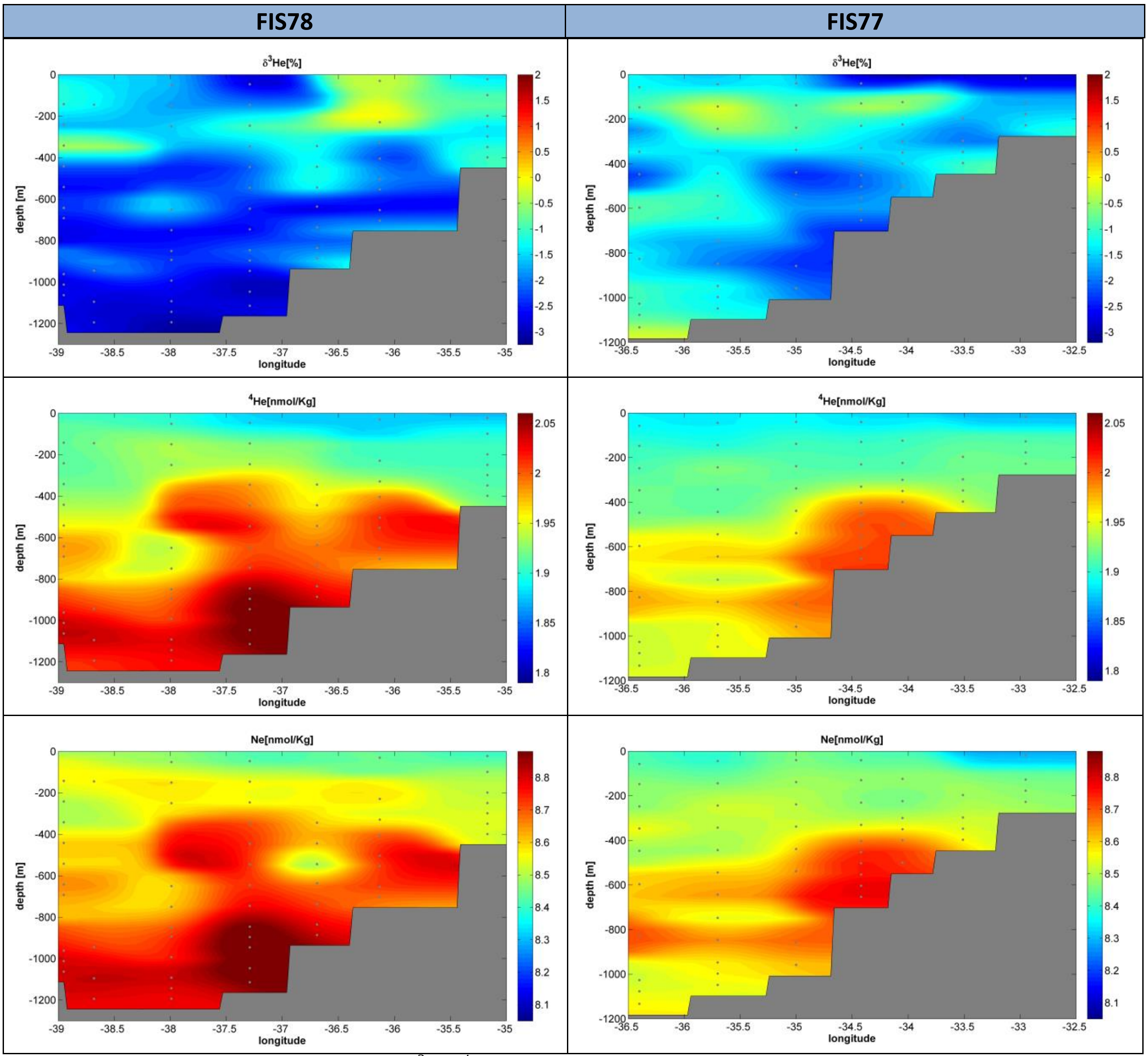

Figure 3.3.3 (continued) The sections of δ^3He, ^{4}He and Ne in front of the Filchner Ice Shelf at located stations in the maps.

The WW in FIS77 in the upper 100m) is highest at 37ºW of around 70%. A similar fraction of WW around 70% is also present in surface water at 33ºW in FIS78. The presence of WDW in Figure 3.3.3 is almost invisible (<15%) in both WDW sections (FIS77 and FIS78). The θ and δ^3He sections (FIS78) also support negligible WDW entrainment into the region by their lowest values measured in the Weddell Sea. A minor increase in δ^3He at 200m depth in δ^3He section does not make WDW significantly visible (<15%) in FIS77. The initiator water mass is HSSW produced along RIS and converted into ISW after mixing with basal GMW. The HSSW exceeding 90% is traced from 500m to 1100m depth in FIS at 37ºW in FIS78 in Figure 3.3.3. The HSSW up to 80% is also observed at 600m depth at 34.5ºW in FIS77.

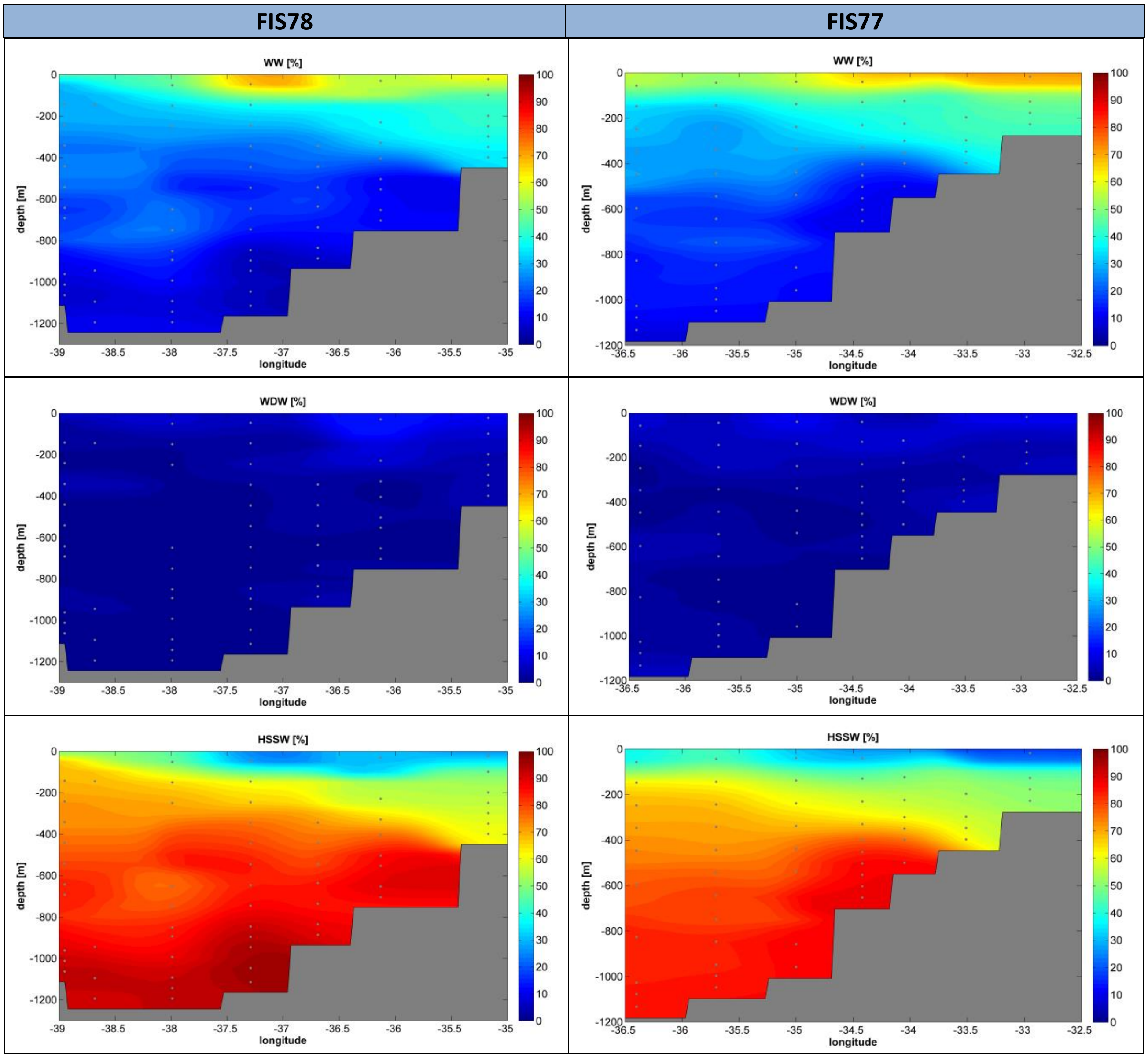

Figure 3.3.3 The sections of the WW, WDW and HSSW in front of the Filchner Ice Shelf at located stations in the maps.

In the GMW section (FIS78, directly in front of the ice shelf front), the highest fraction of GMW is up to 0.47% at 1000m depth at 37ºW and two other GMW plumes are also noticed both at 500m depth at 35.5ºW and 37.5ºW. The maximum GMW fraction is by 88% higher at FIS78 than at RIS (see Figure 3.3.2). Therefore, it is assumed that the major basal melting happens below FRIS and takes its way out of the FIS through Filchner Depression. According to Joughin & Padman 2003, the junction located between the RIS and FIS is assumed to be the largest flux gate of GMW within the FRIS cavity with a basal melt rate of 24.8Gtons/yr from remote sensing data sets.

The FIS77 section exhibit the dynamics of the GMW plume further northward of FIS and show the dispersal of GMW by lower fraction detected at FIS77 compared to the FIS78. The maximum GMW is 0.35% at 600m at 34ºW in FIS77. Thus, the fraction of GMW has been reduced by 25.5% from FIS78 to FIS77. The cause of the GMW fraction decrease could be that a part of the GMW plume at

FIS78 (0.47% at 37ºW in1000m depth) is diverted to the western slope of the Filchner Trough and the rest of the plume flows along the eastern Filchner Trough slope or the GMW plume is trapped inside the Filchner Trough as a phenomena of recirculation. Foldvik et al. 1985 has also indicated a trapped ISW mass in the Filchner Trough at the FIS front. A layer of ISW can also be observed at 37.7ºW in 600m depth (FIS78) that has become less saline compared to the trapped ISW below, likely due to dilution with upper water masses or it originates from a slightly different source with higher HSSW and lower GMW.

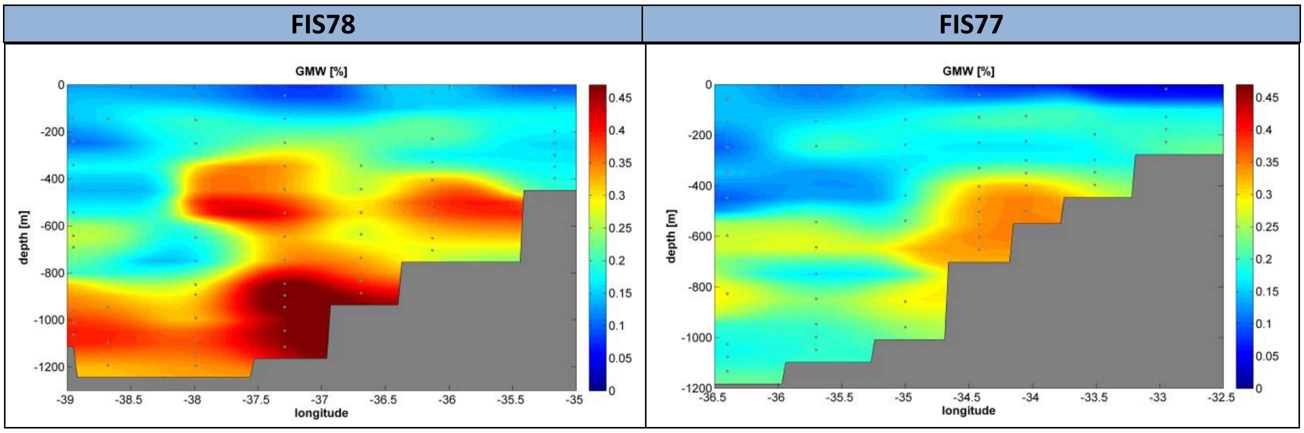

Figure 3.3.3 The sections GMW in front of the Filchner Ice Shelf at located stations in the maps.

The GMW as confined in ISW would recirculate and mix again with new GMW plume until the ISW is low saline and less dense enough to stratify over the recirculation region. We can also speculate that the GMW fraction of 0.47% (the highest calculated from the data) might have been caused due to repeated mixing of trapped ISW with newly formed ISW.

The GMW could also be diluted from ambient water flowing southward. The westward dilution of the GMW plume with ambient water is visible in 800m to 1200m depth from 37ºW to 39ºW in the GMW (FIS78) section and in 400m to 1000m depth from 33.5ºW to 36.5ºW in GMW (FIS77) section. This dispersal can also be traced by their respective ^{4}He and Ne at similar depths and longitudes. The dispersal of GMW is mainly restricted by the topography of the Filchner Depression.

The above analysis between the two sections across the Filchner Trough show a decrease of GMW fraction so as well as to ^{4}He, Ne and HSSW along the flow northward within the through Filchner Trough.

3.3.3 The Filchner-Ronne Ice Shelves (FRIS) FRIS95 and FRIS14 Sections

Further to the north than the two previous sections we have two other sections across the Filchner Depression available, "FRIS95" and "FRIS14". The stations in the FRIS14 section lie 35 km further north of FRIS95. Hence, spatial variation might hamper the comparison of these two sub-sections.

The comparison of θ shows that θ is below -1.5ºC in both sections (FRIS95 and FRIS14). However, θ show an increase from -2ºC to -1.5ºC in 300m to 650m depth, and a decrease from -1.5ºC to -1.9ºC to in surface water between the two sections. The section FRIS14 shows very low salinity (34.25) in the surface water as compared to FRIS 95 (34.42). The lower salinity in FRIS14 is also visible below 200m. The salinity decrease in surface water of FRIS14 can be regarded as sea ice melting and/or decreased formation of sea ice and the decrease below 200m can be expected due to increased GMW formation.

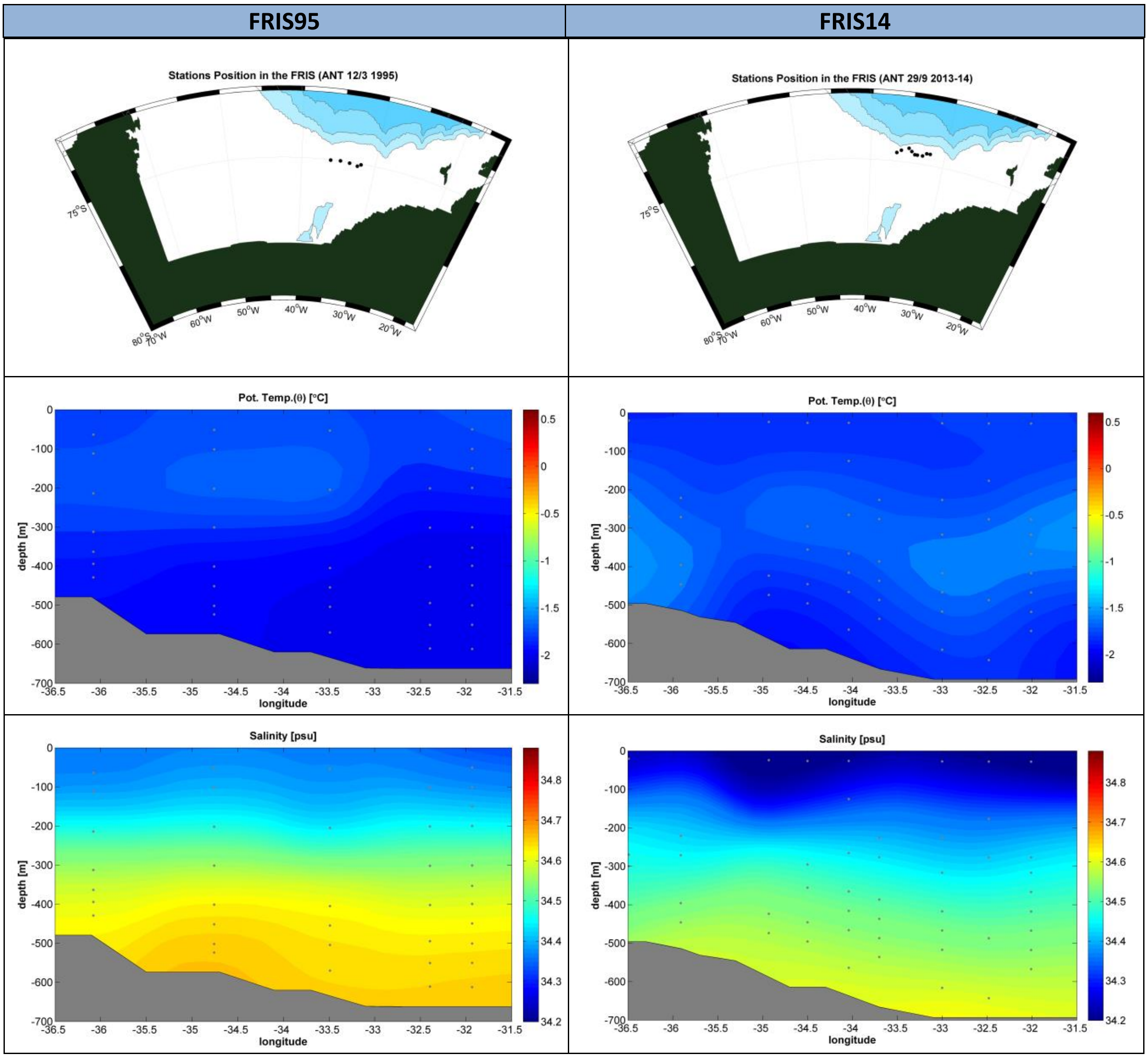

Figure 3.3.4 (continued) The sections of the θ and salinity as a comparison of two longitudinal strips from (FRIS95) ANT 12/3(1995) and (FRIS14) ANT 29/9(2013-14), stations shown in black dots in the maps.

The δ^3He sections (FRIS95 and FRIS14) show a little increase +1% of δ^3He at the eastern edge in 300m to 650m, and a decrease of -1% in surface water. The ^{4}He is about 1.95 nmol/kg at the eastern edge below 400m in both ^{4}He section. But in FRIS14 a second core with higher ^{4}He is observed at 35ºW below 400m. The FRIS14 Ne sections follow the similar pattern as ^{4}He in FRIS14 with Ne around 8.60 nmol/kg at the eastern edge below 400m depth in both Ne sections and shows in FRIS14 at 35ºW below 400m the same second plume. The ^{4}He and Ne occurrence in the second plume would mean either an additional GMW plume appearance in the 20 years interval. Another reason that is not visible in the FIS95 section could be that it originates from a secondary GMW flow path, e.g. more on the western side of the Filchner Depression, but we will show below, that increased GMW formation is the more likely reason.

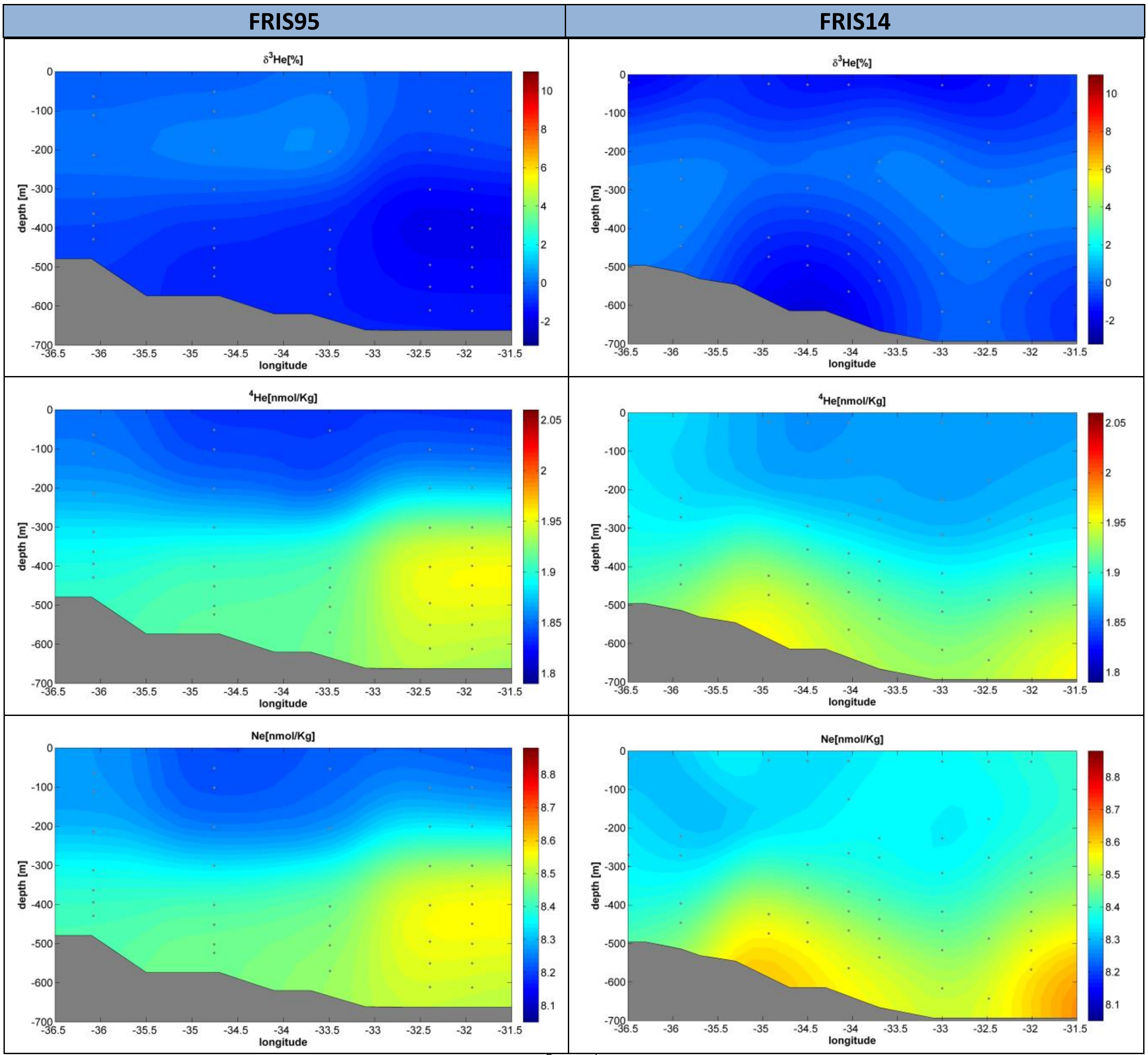

Figure 3.3.4 (continued) The sections of the tracers δ^3He, ^{4}He and Ne as a comparison of two strips from (FRIS95) ANT 12/3(1995) and (FRIS14) ANT 29/9(2013-14) as shown at located stations in the maps.

Also the WW is increased in surface water from 50% to 70% between FRIS1995 and FRIS14 and similar below 200m by +20% WW. The WDW is below 25% throughout both WDW sections (FRIS14 and FRIS95). However, a slight increase of WDW can be noticed from 200m to 500m in FRIS14 compared to the FRIS95. That can be explained by the position of that section further north and hence, closer to WDW circulating in the inner basin.

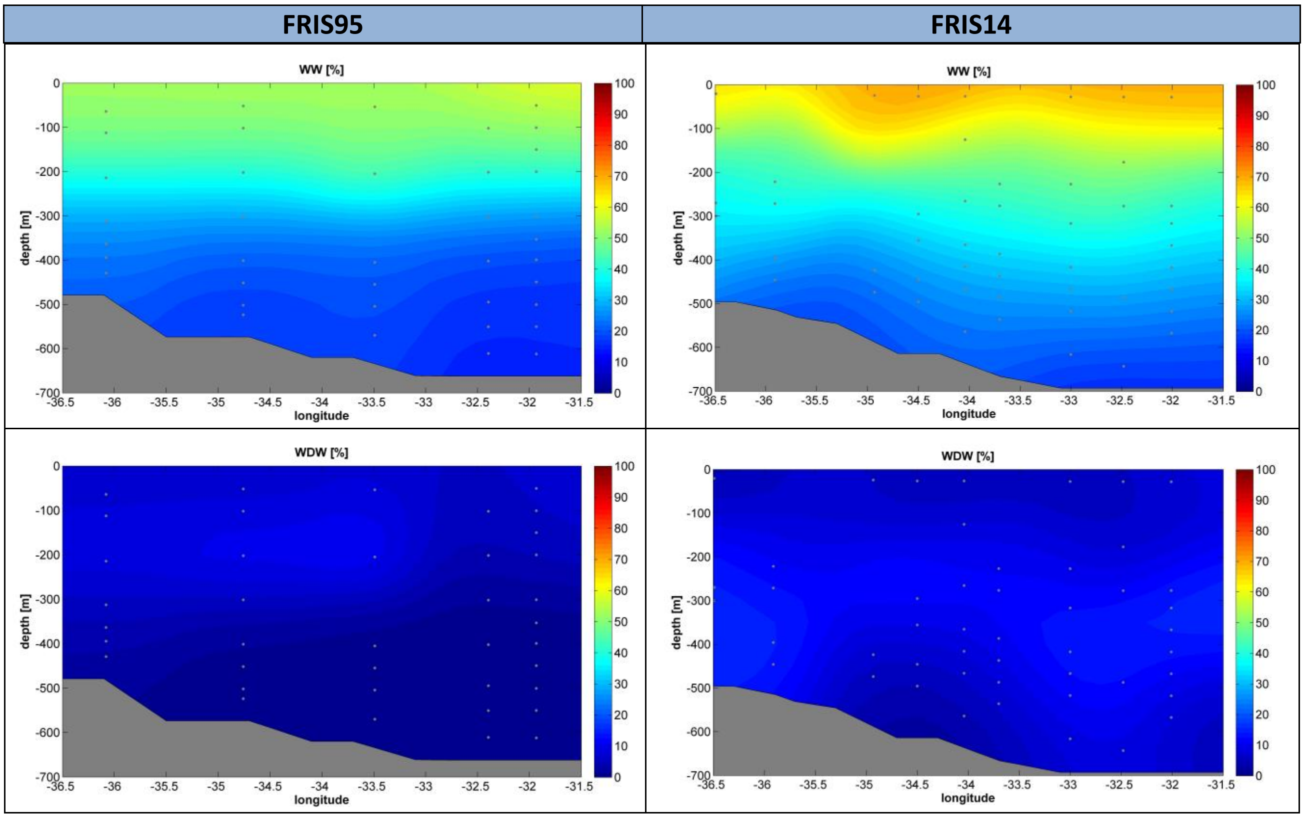

Figure 3.3.4 (continued) The sections of WW and WDW as a comparison of two longitudinal strips from (FRIS95) ANT 12/3(1995) and (FRIS14) ANT 29/9(2013-14) as shown at located stations in the maps.

The HSSW is in both sections the dominant water mass of 50% in the surface water and 80% below 300m is HSSW in section FRIS95. The FRIS14 shows -30% less HSSW, in the western part of the section in 400m depth, and HSSW has decreased by -20% in the surface water between FRIS95 and FRIS14 HSSW sections, hence the HSSW sufficient decreases from the south to the north of the section. Either less HSSW is formed during the 20 years interval, or the HSSW is more diluted by less saline water, most likely by increased GMW formation.

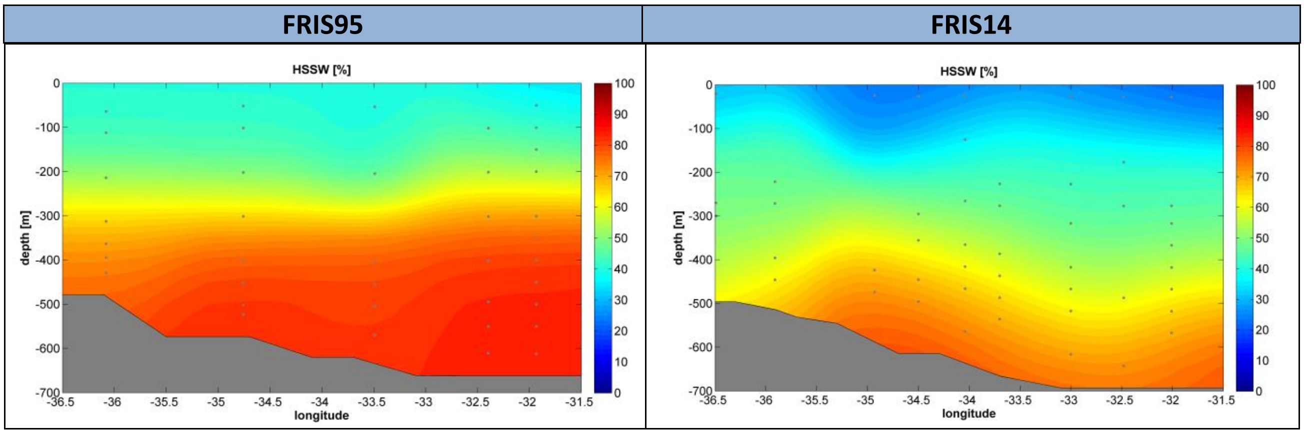

Figure 3.3.4 (continued)The sections of HSSW as a comparison of two longitudinal strips from (FRIS95) ANT 12/3(1995) and (FRIS14) ANT 29/9(2013-14) as shown at located stations in the maps.

The FRIS95 section shows GMW 0.25% in 300m to 650m depth at 31.5ºW and no GMW plume is measured in the west of the section. The FRIS14 section shows two GMW plumes between 500m to

700m depth at 31.5ºW and 35ºW. This ‘new’ GMW plume of 0.25% in 500m depth at 35ºW in section FRIS14, and cannot be observed in the section FRIS95. Since the GMW observed in the Filchner Depression has its source further south that increases after 20 years in the northern section (FRIS14) can only be explained by increasing GMW formation at the FRIS.

FRIS95	FRIS14

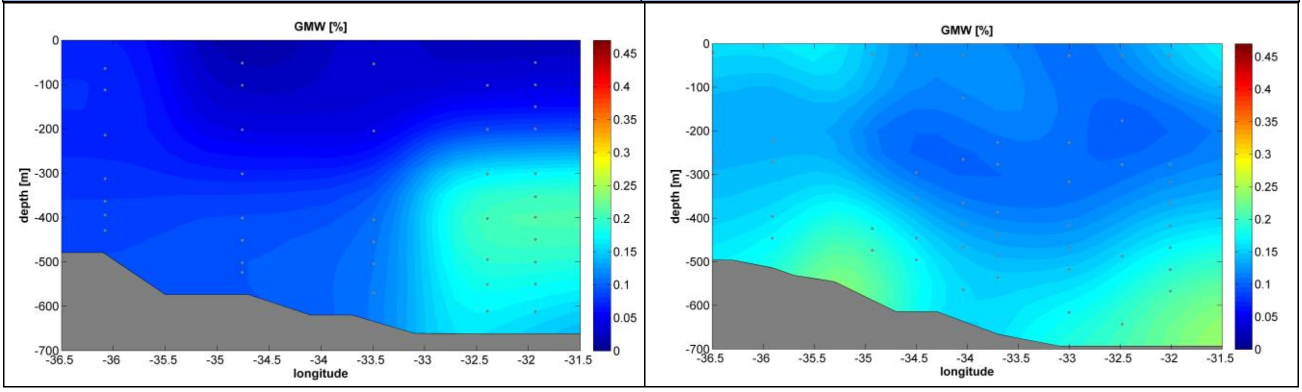

Figure 3.3.4 The sections of GMW as a comparison of two longitudinal strips from (FRIS95) ANT 12/3(1995) and (FRIS14) ANT 29/9(2013-14) as shown at located stations in the maps.

This sufficient decrease of HSSW and salinity and increase of WW in the upper layers in 2014 (FRIS14 sections) as compared to 1995 (FRIS95 sections) could have been caused by less sea ice formation the in the Weddell Sea. However, a ‘new’ plume of 0.25% GMW with higher Ne is detected (even though FRIS14 is 35Km north of FRIS95) in the FRIS14 section. This would lead to the conclusion of increased basal melting and in addition decrease of sea ice formation in the Weddell Sea during the interval of 20 years. Increased GMW formation explains the temporal changes in the salinity and HSSW and increased GMW on the northern FRIS14 section. Such a temporal freshening and increased basal melting of FRIS are also indicated by (Timmermann & Hellmer 2013) in Chapter 1.6.

3.3.4 The Filchner Slope FRIS30 and FRIS35 Section

The sections in the right column of Figure 3.3.5 (FRIS30) 30ºW of Filchner Slope comprise data only from ANT 29/9 (2013-14) and are more exposed to EWIS influx. The sections in the left column of Figure 3.3.5 (FRIS35) 35ºW include data from ANT 12/3 (1995) and from ANT 29/9(2013-14); therefore, temporal variances in the water masses could undermine the interpolation. The empty white patches in sections of (FRIS35) are due to larger data gaps.

FRIS35	FRIS30
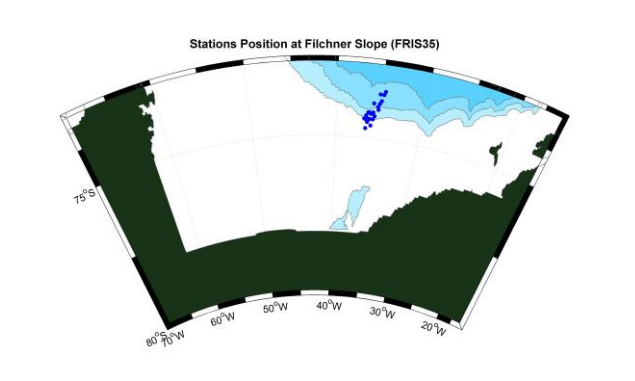	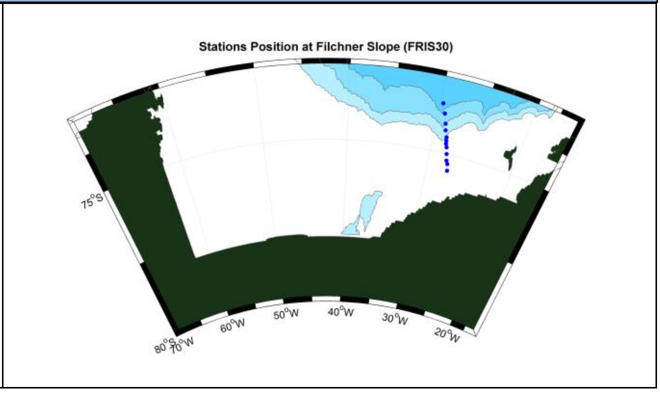

Figure 3.3.5 (continued) The sections stations map FRIS35 (left) and FIS77 (right) over Filchner Slope as shown in blue dots in the maps.

In FRIS30 cold water of -1.9ºC dominates the upper 400m and the warmest water (θ = 0.6ºC) is found northward in 1000m depth, further down θ decreases to subzero at greater depth of 3000m due to EWIS's bottom water entrainment .In FRIS30 θ shows a strong increase along the slope from -1.5ºC to -0.4ºC from 500m to 3000m depth respectively.

FRIS35	FRIS30
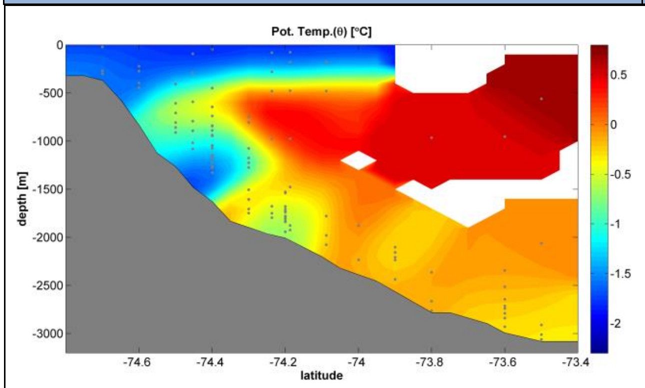	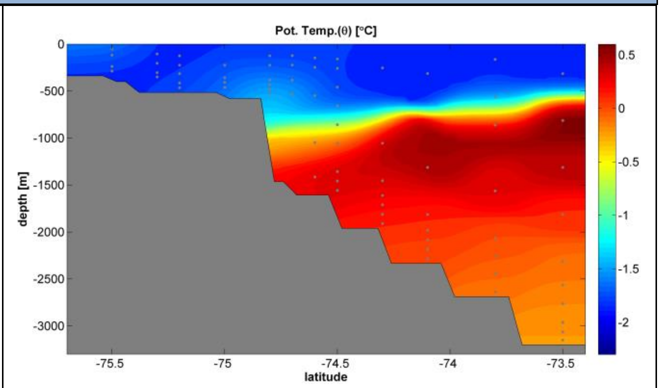
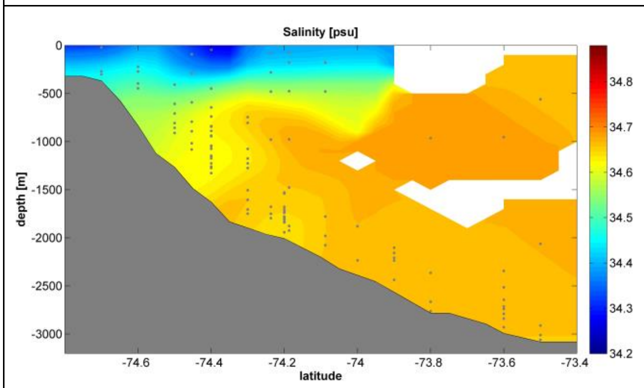	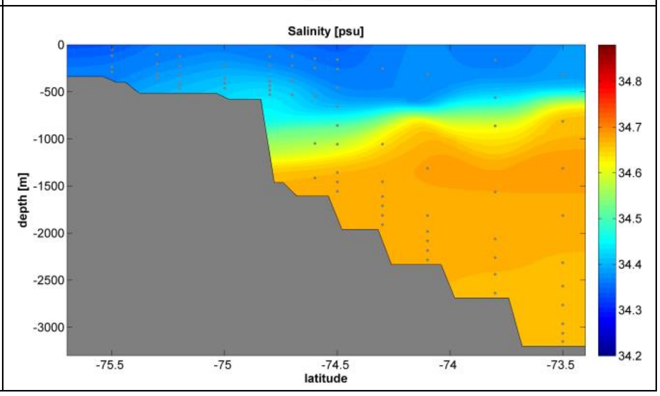

Figure 3.3.5 (continued) The sections of θ and salinity over Filchner Slope as shown in blue dots in the maps.

The low temperatures down the slope ≈2000 m in the FRIS35, are not visible in FRIS30, and clearly indicate the presence of ISW spilling out of the Filchner Depression. The salinity section (FRIS30) shows that the WDW is more saline (around 34.65psu) than the southern shallow cold water (S < 34.4psu). The FRIS35 salinity also shows dominance of saline WDW (S = 34.65psu) rather than HSSW (34.60) when compared to FRIS35.

The δ^{3}He section (FRIS30) shows δ^{3}He around 8% at 73.5ºS in 1300 depth, the δ^{3}He decreases when it gets closer to the Filchner Slope. Therefore, it indicates the addition of ^{4}He due to dilution with other water masses. The δ^{3}He section (FRIS35) also shows δ^{3}He around 8% at 73.5ºS in 500 depth (shallower than δ^{3}He in FRIS30), but that effect is most likely caused by interpolation, since there are not sufficient data at the surface) and decreases fast when it gets closer to the Filchner slope. That faster decrease could be caused by addition of ^{4}He from GMW/ISW spilling out of the Filchner Depression.

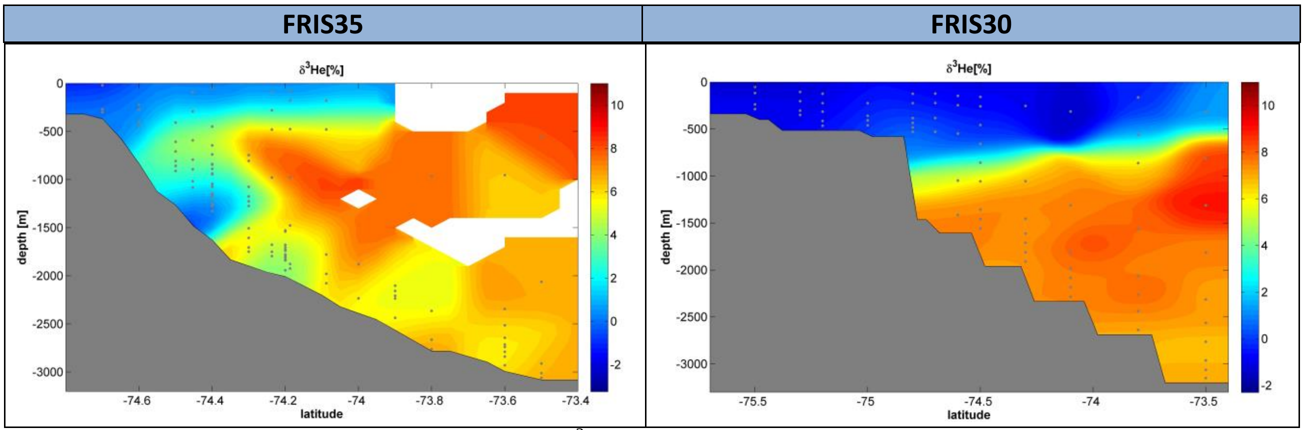

Figure 3.3.5 (continued) The sections of δ^{3}He over Filchner Slope as shown in blue dots in the maps.

The ^{4}He section (FRIS30) shows 1.91 nmol/kg south of 75.5ºS in 500m depth on the shelf and higher ^{4}He of around 1.92 nmol/kg is observed north of 73.5ºS between 1300m to 3000m. The Ne section (FRIS30) shows values around 8.45 nmol/kg on the shelf and extending northward in the upper 500m op to 73.75°S. Ne is around 8.25 nmol/kg below 1300m. There is a weak ^{4}He signal (and even weaker Ne signal) visible at 73.5°S between 1300m to3000m, indicating a GMW plume from EWIS.

The ^{4}He section (FRIS35) has 1.94 nmol/kg over the slope at 74.5ºS in 500m to 1500 depth and then decreases fast down the slope with a slight increased signal of ^{4}He in the bottom water visible at 73.5°S between 2500m to 3000m. The Ne in section FRIS35 is the highest (8.45 nmol/kg) in 500m to 1500 depth at 74.5ºS and then decreases down the slope with a slight increased signal in the bottom of the deep basin.

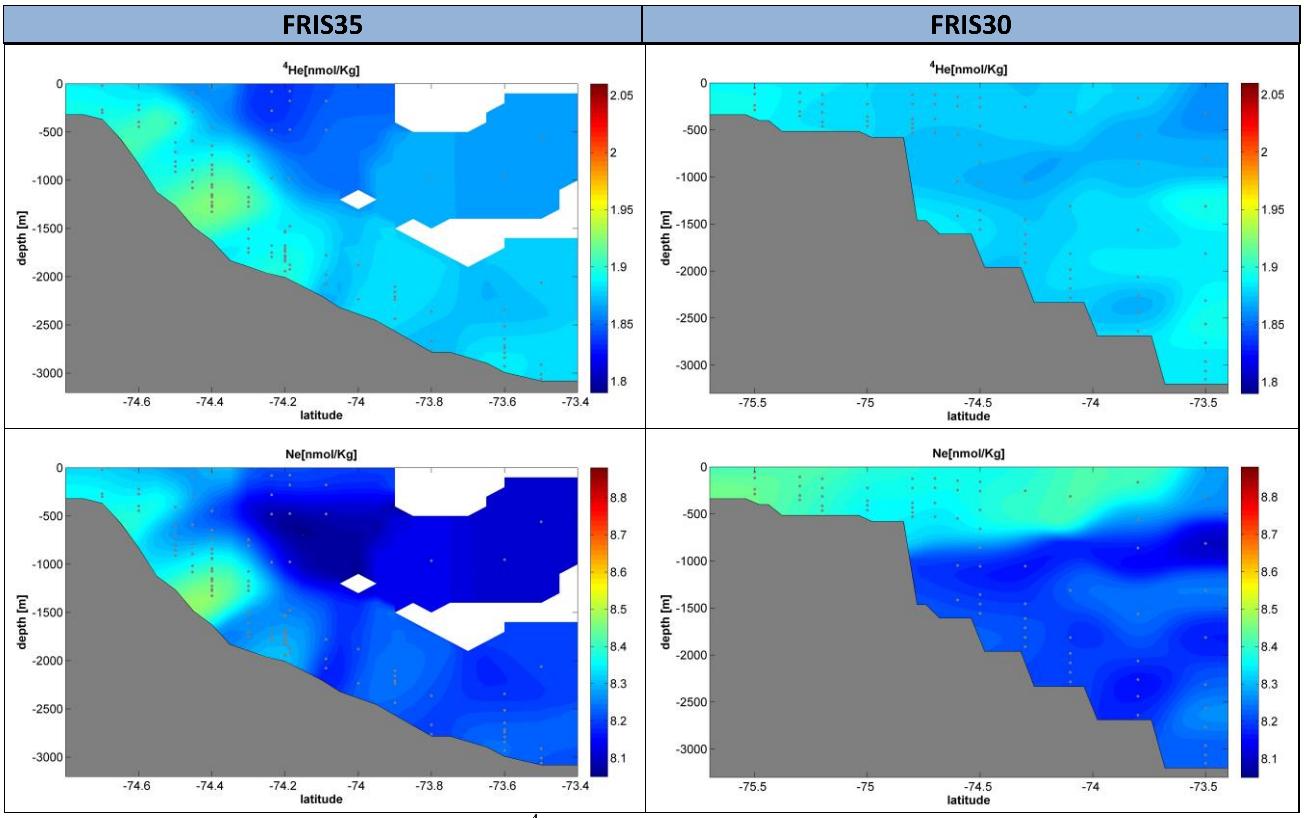

Figure 3.3.5 (continued) The sections of ^{4}He and Ne over Filchner Slope as shown in blue dots in the maps.

The FRIS30 cold upper layer down to 500m depth constitutes HSSW>50% with higher Ne > 8.45 nmol/kg, whereas the bottom water at 73.5ºS has HSSW around 30%. The HSSW section (FRIS35) exhibit a similar pattern of mixing as in the GMW section (FRIS35) and losses a large fraction while mixing with WDW over the slope and measured around 35% at the bottom water.

The WDW is sandwiched between overlying cold surface and cold bottom water. The WDW extent towards the slope is from North to South is similar in both WDW sections (FRIS30 and FRIS35) but mixing of cold FRIS water and WDW can be observed at 74.4ºS between 500m to 1500m depth in FRIS35. The WDW mixing with other water masses over the slope seems lower in FRIS30. The WW is also around 50% in the upper 500m (similar in FRIS30 and FRIS35). The strength of WW is stronger in FRIS30 if compared to FRIS35.

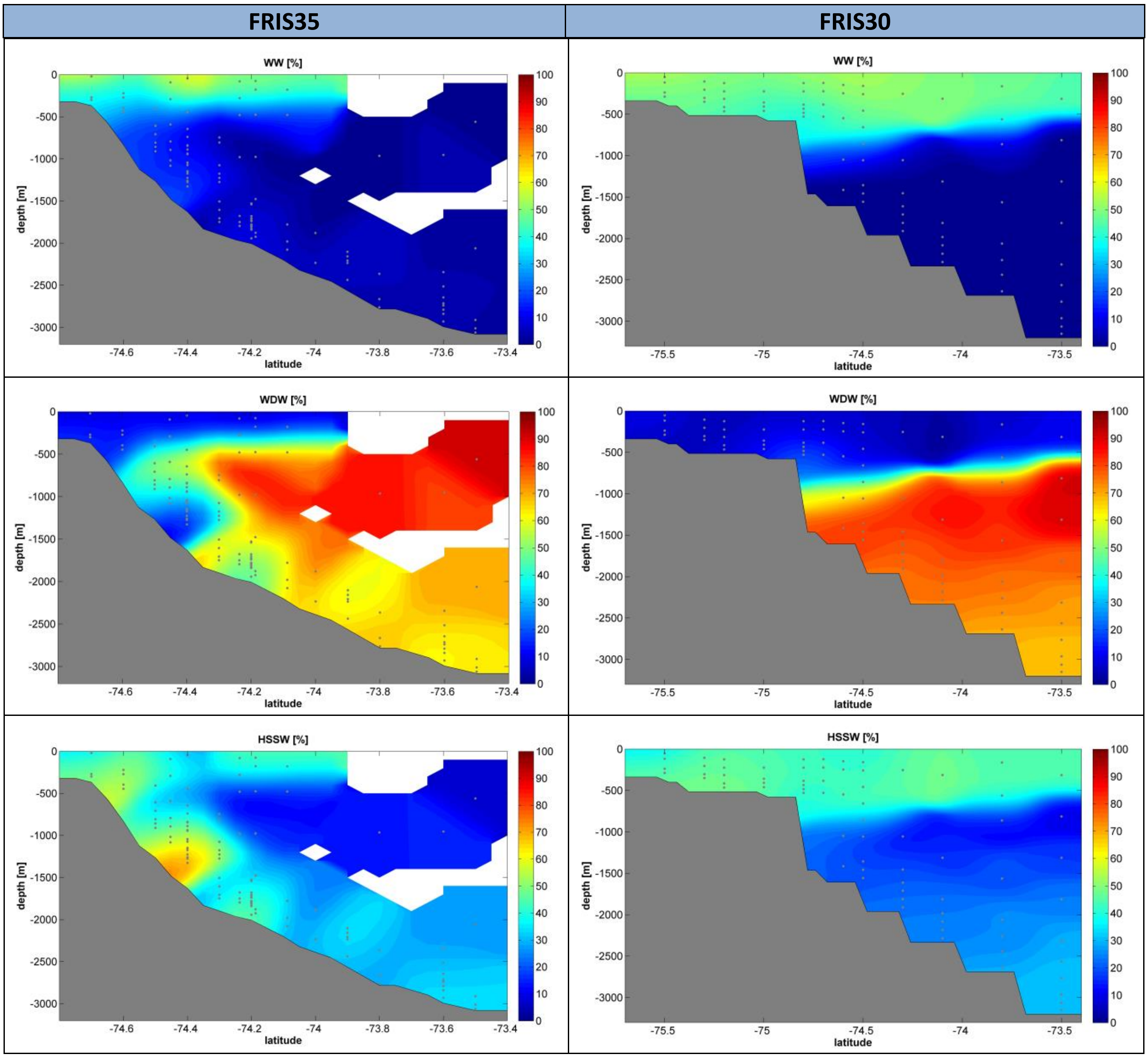

Figure 3.3.5 (continued) The sections of the calculated WW, WDW and HSSW on the Filchner Slope as shown in blue dots in the maps.

In the GMW section (FRIS30) an unexpected high GMW signal can be seen with fraction 0.25% at the northern edge of the section. There is only 0.17% at the southern shallow shelf water in 500m depth. The deep signal on FRIS30 can be identified also in FRIS35, but there it is only visible between 2500-3000m depth. The FRIS35 shows 0.25% at the slope front in 500m at 74.5ºS.

A rapid decrease of GMW can be observed (0.1%) down the slope to 2500m and then a sudden increase of +0.07% at the bottom of the basin at its northern edge is observed and recognized as a plume of GMW likely coming from EWIS. Therefore, apparently there are two GMW plumes detected on the slope in FRIS35, one GMW plume in the bottom water and one on the upper part of the slope. The GMW plume in bottom water is likely originating from EWIS, the upper on from Filchner Depression. The flow of GMW plume is westward along the boundary of the slope. The

GMW section (FRIS30) shows two GMW plumes, one in shallow shelf water and a second GMW plume in northern deep water.

FRIS35	FRIS30

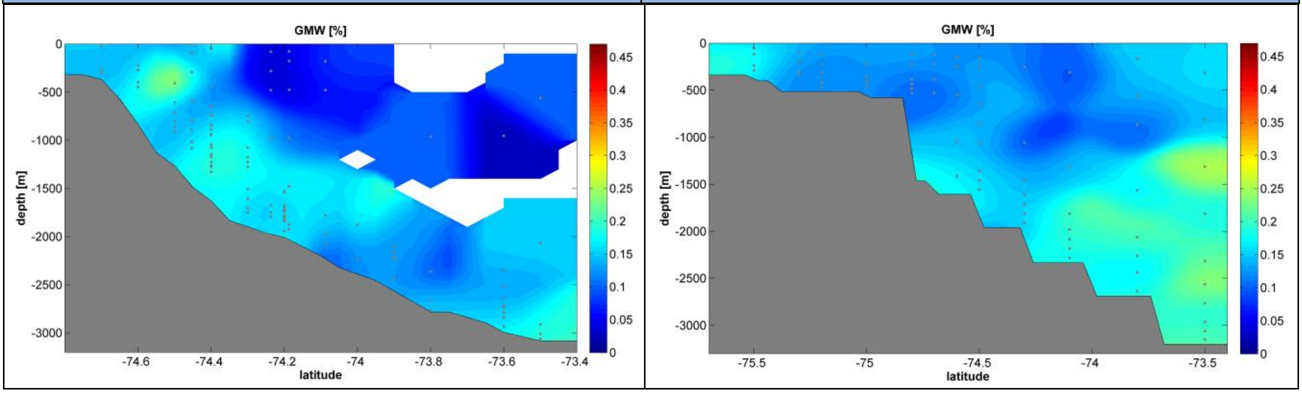

Figure 3.3.5 The sections of GMW on the Filchner Slope as shown in blue dots in the maps.

The sections analysis (Figure 3.3.4 and Figure 3.3.5) from the Filchner Slope reveals FRIS water interaction with WDW from Weddell deep water and demonstrates the formation of WSBW (HSSW+GMW+WDW). The sections also show a fraction of GMW plume in the bottom water along the Filchner Slope originating from the EWIS.

The all above analysis propose the general circulation of the observed water masses in the FRIS region and interaction with Weddell deep water and EWIS water. The HSSW source could be identified in front of RIS, where it may sink down to the Ronne Depression into the shelf cavity. The HSSW flows to the FRIS and mixes with GMW (and generates ISW) that comes out of the FIS front, east of the Berkner Island. The OMP reveals the highest GMW fraction directly in front of the FIS where is flows out of the cavity. The GMW plume is then quickly dispersed in the Filchner Depression and even to the LIS. A 20 year temporal analysis near Filchner shelf break indicates freshening of the shelf water; however the temporal and spatial resolution of the data is very low and more measurements at the region are required.

3.4 The Larsen Ice Shelf (LIS) Sections

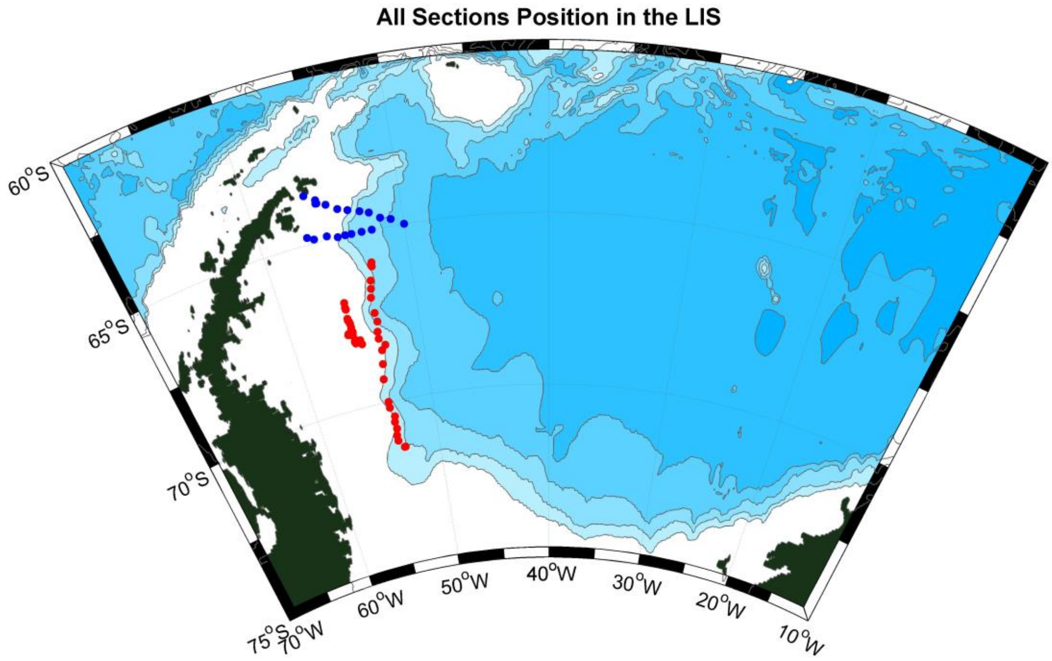

Figure 3.4.1 The map including the sections position in the LIS. The sections in red (ISW1 and ISPOL) are compared to each other and same as to blue sections. The ISPOL 'helicopter-stations' (only single NG samples near the bottom) have been removed due to their "random" occurrence off the drift track.

In the introduction chapter 1.6 we have discussed the fragile existence of LIS analyzed by (Paolo et al. 2015) and Timmermann & Hellmer 2013. The LIS has been exclusively explored by two expeditions ISW-1 (1992) and ISPOL (2005) and one at northern edge of LIS region by ANT 29/3 (2013) that is located nearest downstream to ISW-1 and ISPOL. The LIS front is located at ~60ºW and the ISW1 section lies along the LIS slope at ~54ºW as shown in the map (Figure 3.4.1). The stations of ISPOL are located closer to LIS than ISW-1. The Ne measurements for ISW-1 is not available therefore the OMP is applied without Ne.

3.4.1 The ISW-1 and the ISPOL Sections

The sections Figure 3.4.2 analyzed here give further information of the circulation between FRIS and LIS and of LIS interaction with the Weddell deep water. The stations of ISW-1 Figure 3.4.2 (right) are located along the expected WSBW flow along the LIS continental slope. The LIS front is almost 300Km far from ISW-1 and 230Km far from ISPOL stations at 68ºS.

The surface and bottom waters are found at similar $\theta \approx -1.88$˚C (ISW-1). The warm water above 0.6ºC is dominant in 500m to 1500m depth. The θ decreases fast below 1000m depth. The bottom water ($\theta < -1$˚C) can be identified as WSBW in the θ section (ISW-1). In the θ section (ISPOL), the surface water in the upper 200m is found around the surface freezing point -1.88ºC. The subzero cold bottom water in the northern edge of ISPOL might have been caused by the expected local GMW production. The salinity section (ISW-1) shows high saline warm water 34.68psu in 500m to 1500m depth. The salinity section (ISPOL) also shows the high saline 34.68psu warm water in 600m to 1600m depth and the surface water is the lowest saline with 34.38psu.

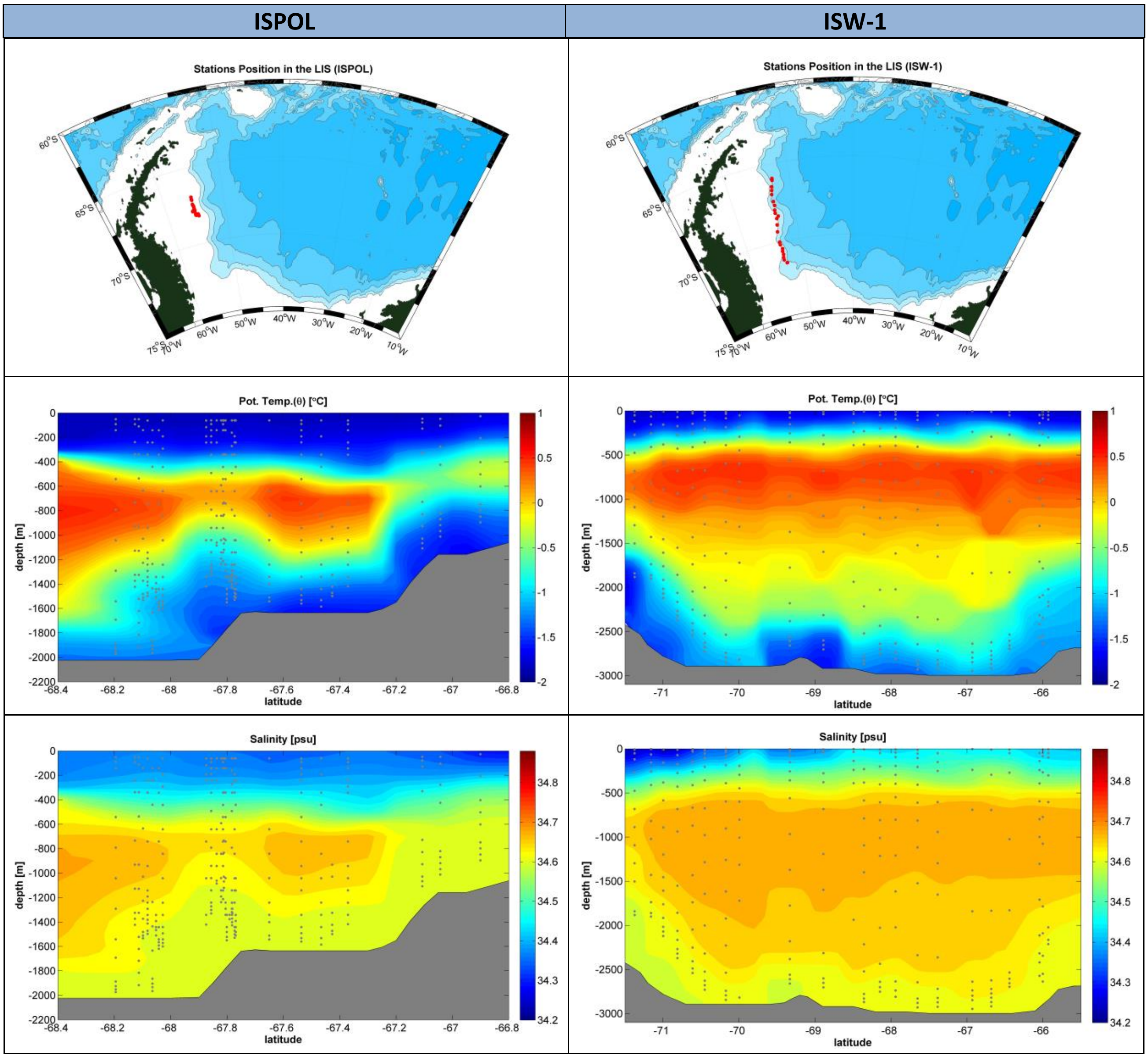

Figure 3.4.2 (continued) The sections of the θ and salinity as a comparison of two strips from (right) ISW-1 (1995) and (left) ISPOL (2005) as shown in red dots in the maps.

The δ^3He in 500m to 1500m depth (ISW-1) is around 8% and dominant in 500m to 1500m depth, and indicates expected WDW in high fractions. In δ^3He section (ISPOL), the δ^3He is about 8% south of 68ºS in 400m to 1600m depth, δ^3He has a minimum in the layer at 67.8ºS. This decrease of δ^3He might have been caused by the mixing with water mass low in δ^3He e.g. WW and HSSW.

The ^{4}He (ISW-1) as three clear spots around 1.95 nmol/kg to 1.93 nmol/kg are observed in 1400m and 2400m at 70ºS, 69.3ºS and 68.2ºS. The ^{4}He concentration seems to decrease in the bottom water from south to north in the section (ISW-1) with some noticeable sudden increase at 70ºS and 68.2ºS in the bottom water.

The ^{4}He section (ISPOL) shows the highest ^{4}He in the section around 1.94 nmol/kg in the northern bottom water, other strong signals of ^{4}He around 1.93nmol/kg are observed at 67.8ºS in 1300m depth and at southern edge in the bottom water . The Ne section (ISPOL) has the highest 8.56 nmol/kg at 67ºS in the bottom water. The strong signals of Ne are observed in 1600m depth at 67.1ºS and in 1300m depth in the northern bottom water of the section.

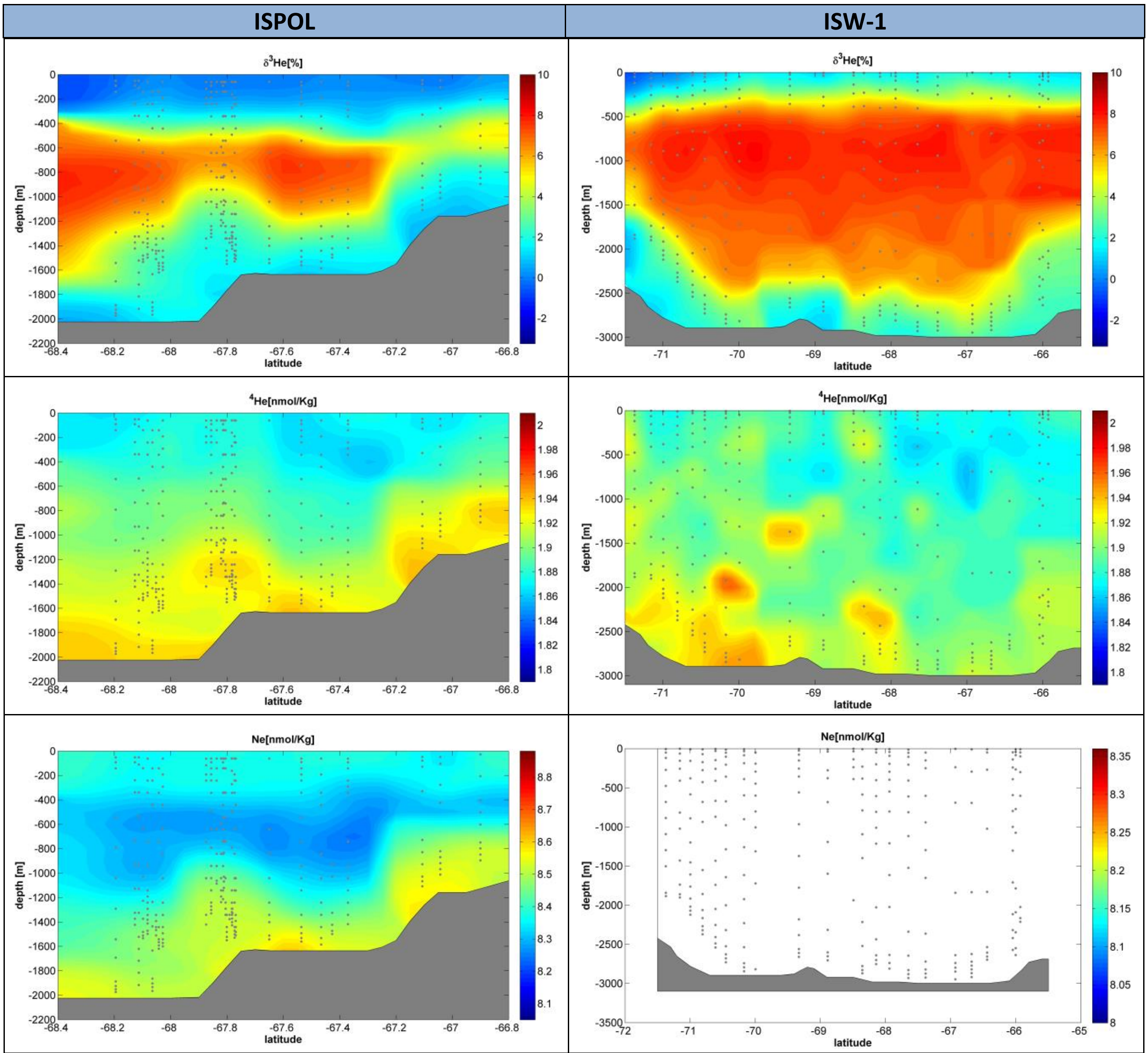

Figure 3.4.2 (continued) The sections of δ^{3}He, ^{4}He and Ne as a comparison of two strips from (right) ISW-1 (1995) and (left) ISPOL (2005). The interpolation is not available for Ne section (ISW-1) because Ne data is not present from ISW-1.

The WW section (ISW-1) shows WW not higher than 55% at 71ºS in the surface water and the fraction decrease below 35% in the surface water north of 70.5ºS. The bottom water has WW below 20% in the section. The WW (ISPOL) is around 50% throughout the surface water in WW section (ISPOL); the bottom water has WW < 20% in the section.

The WDW (ISW-1) is around 85% (with θ = 0.6ºC) in 500m to 1500m depth and sandwiched between surface and cold bottom water. WDW is found up to 60% even in 2400m depth in the WDW section. The WDW (ISPOL) fractions seem to decline from south to north. The WDW is < 85% south of 68ºS in 400m to 1600m depth, it decreases at 67.8ºS and again decreases north of 67.8ºS.

ISPOL	ISW-1

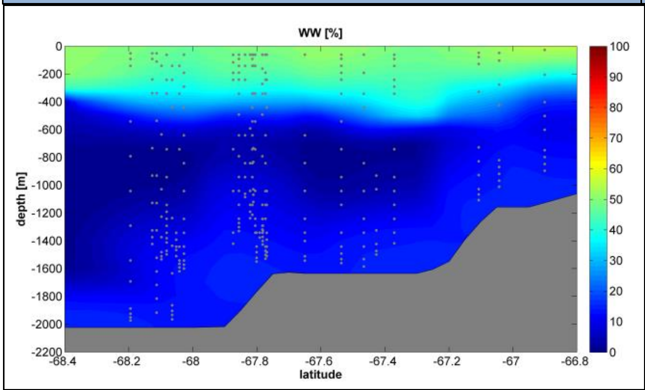

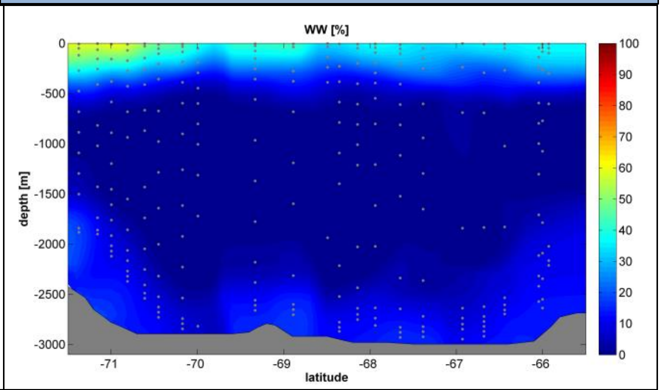

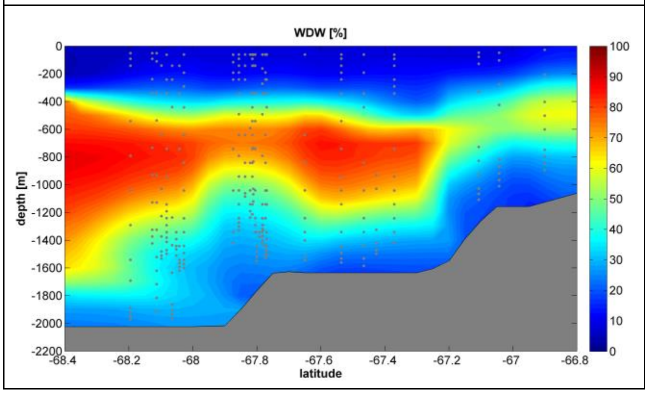

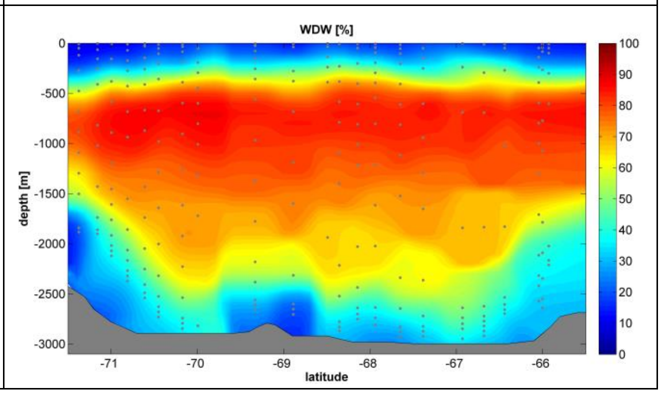

Figure 3.4.2 (continued) The sections WW and WDW as a comparison of two strips from (right) ISW-1 (1995) and (left) ISPOL (2005).

The HSSW section (ISW-1) shows 65% in its southern bottom water and decreases to 50% northward at the bottom with an exceptional sudden decrease at 70ºS and increase at 69ºS. The HSSW section (ISPOL) shows 65% in its northern bottom water and decreases to 50% in the southern bottom water. The HSSW in the surface is calculated around 50%.

The GMW section (ISW-1) shows the highest fraction of 0.37% in the WSDW (θ ≈ -0.2˚C) in 2000m at 70ºS. There are two additional 'warm' GMW plumes of 0.33% in 1400m at 69.5ºS in WDW (θ ≈ 0°C) and in 2400m at 68.2ºS, their occurrence in WSDW/WDW (where θ > -0.3ºC) might be related to LIS basal melting and its mixing with mWDW at LIS slope. If we see the ^4He, GMW, WDW and HSSW sections simultaneously, we find that the ^{4}He section (ISW-1) supports the warm GMW plume at 70ºS with the highest 1.96 nmol/kg in 1200m to 2500m depth, where relatively high WDW > 70% is found as compared to low HSSW < 30%.

Another (ISW-1) GMW plume around 0.17% emerging from southern edge at 71.5ºS is located in colder water θ ≈ -1.8ºC, and higher HSSW ≈ 60%. Since, the GMW is hardly visible but it can be cross verified from the ^{4}He section which shows ^{4}He ≈1.93 nmol/kg at the southern edge at 71.5ºS in the bottom water. The LIS southern extent is nearly at 70ºS and the local GMW of LIS is expected to flow northward, whereas the ISW-1 GMW plume in the cold bottom water appears at 71.5ºS. Thus, we conclude it originates from FRIS WSBW.

Therefore we can assume the cold and warm GMW plumes in the section of ISW-1 from different origin, one in the WSBW (θ < -0.7˚C) emerging from the southern edge of the GMW section (ISW-1), the second is warm GMW plume (θ > -0.7ºC), thus recognized as local WSDW. The WSDW has even higher GMW fraction 0.37% (locally formed) than the GMW fraction 0.2% in WSBW (entrained from FRIS) in the GMW section (ISW-1).

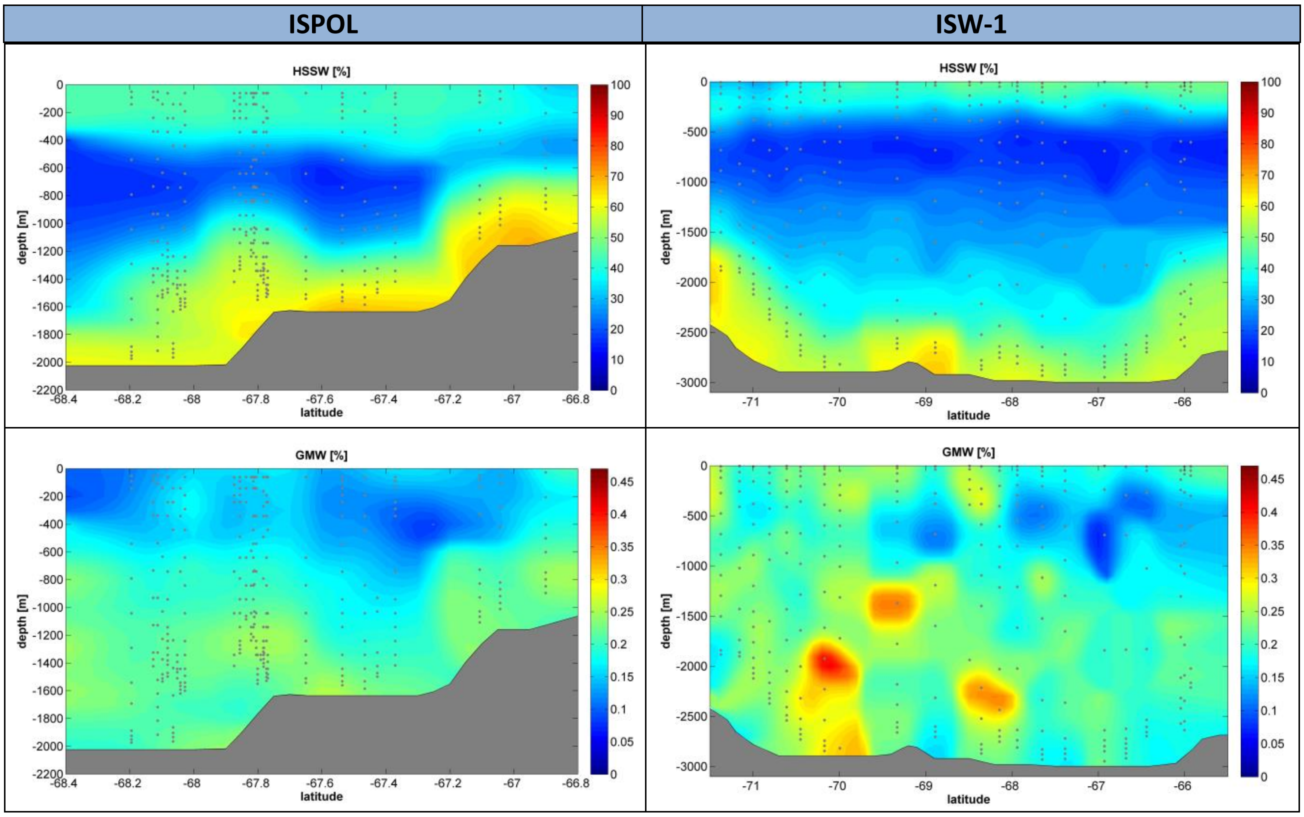

Figure 3.4.2 The sections of HSSW and GMW as a comparison of two strips from (right) ISW-1 (1995) and (left) ISPOL (2005).

In the GMW section (ISW-1), mixing of the warm GMW plume (in local WSDW) and cold GMW plume (in entrained WSBW from FRIS) is also observed at 70ºS and at 68.2ºS from 2500m to the bottom water. This mixing can be verified from the ^{4}He section that shows the sudden increase of

^{4}He concentrations in the bottom water at the same locations. The mixing of local WSDW and FRIS WSBW is higher at 70ºS inferred from the high increase of ^{4}He in the bottom water at same location. This mixing results increased GMW fraction in the bottom water at 70ºS. This increase of GMW fraction is also observed in the GMW map (Figure 3.2.6). The higher mixing particularly at 70ºS might have been caused due to likely steep slope at 70ºS as the mixing occurs most between two water masses where the slope is steeper.

The GMW section (ISPOL) shows a GMW plume of 0.25% in 600m to 1600m depth at 68.3ºS, and the water mass is warm enough (-0.2˚C < θ < 0.5˚C) at the same location. The lowest HSSW < 20% and WDW > 75% can also be observed at the same location in their respective sections (ISPOL). The warm GMW plume might be considered as local formation. We can assume it as produced by basal melting through mWDW entrainment into the LIS cavity. The ISPOL section also shows cold GMW plume 0.25% in the bottom water (WSBW θ < -1.5˚C) from 67.8ºS to 66.8 ºS and is expected as local LIS production. This cold GMW in the WSBW layer decreases to 0.17% from north to south and might indicate the FRIS'WSBW (θ < -0.7˚C) presence in the bottom water at southern edge as similar to ISW-1.

The above analysis also indicates that the LIS front is more exposed to the WDW than the FRIS (WDW sections in Figure 3.3.2, Figure 3.3.3 and Figure 3.3.4). The FRIS sections Figure 3.3.4 are approx. 468Km far from FRIS front and show WDW below 25% throughout the sections but the ISW-1 is only 300Km far from LIS front and shows a WDW layer around 80%.

The GMW fraction in WSDW (also in WDW) is found even higher than the GMW plume in WSBW inferred from θ and WDW and GMW sections (ISW1 sections) at LIS. The HSSW fractions in LIS water are found comparatively lower than FRIS water. The GMW plumes in WSDW shows the mixing of basal GMW and mWDW to form local WSDW (ISW-1 and ISPOL) and WSBW (only ISPOL) in LIS. The HSSW ≈ 60% (ISPOL) in LIS bottom water with GMW fraction up to 0.25% also represents HSSW inflow to the LIS cavity and mixing with basal GMW. Therefore, the sections from the ISPOL show LIS' own formation of WSBW and WSDW. Whereas, the ISW-1 sections could only expose local WSDW

3.4.2 The LIS-1 and the LIS-2 Sections

The sections in Figure 3.4.3 north of LIS at 65ºS from ANT 29/3(2013) provide the nearest longitudinal view section (i.e. perpendicular to the main flow) to LIS. Section LIS2 is a little further downstream than LIS1. The θ section (LIS1) shows temperatures below -1.8ºC on the western shelf and the cold surface layer decreases eastward. On the continental slope, θ shows fast decrease down to bottom of the slope and measured around -1ºC. The warmest water is found east of 54ºW in 500m to 1500 m depth above 0ºC. The θ Section (LIS2) also shows -1.5ºC on western shelf at 55ºW and then the θ decreases down the slope to the bottom water -1 ºC. The warmest water above 0ºC is found east of 54ºW in 500m to 1500m depth.

LIS1	LIS2
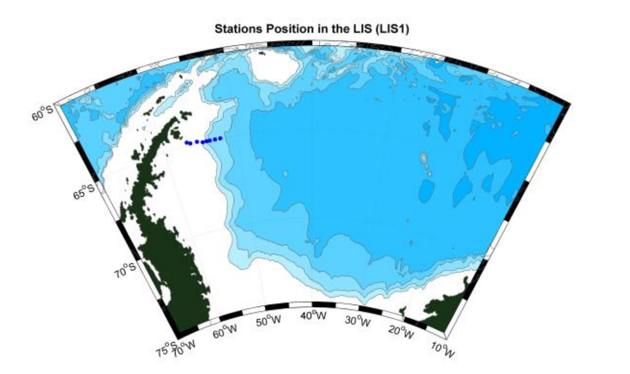	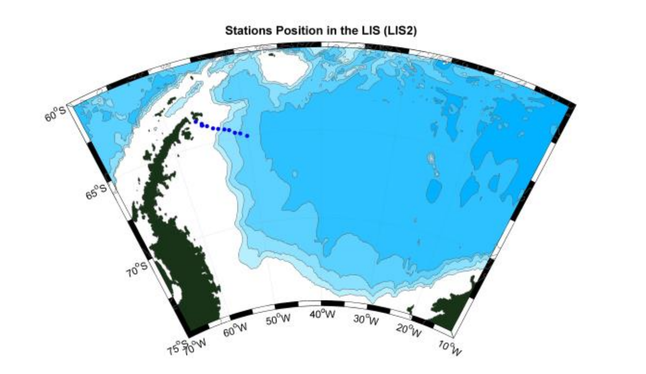
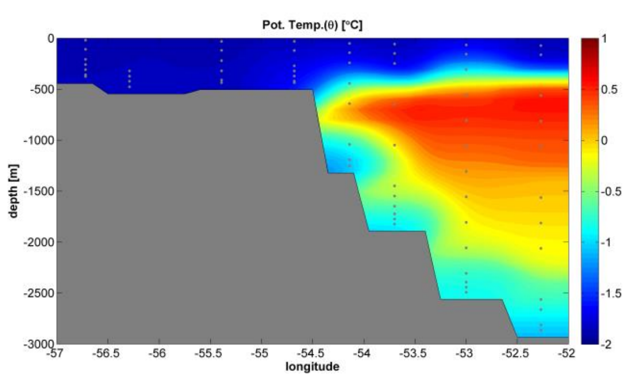	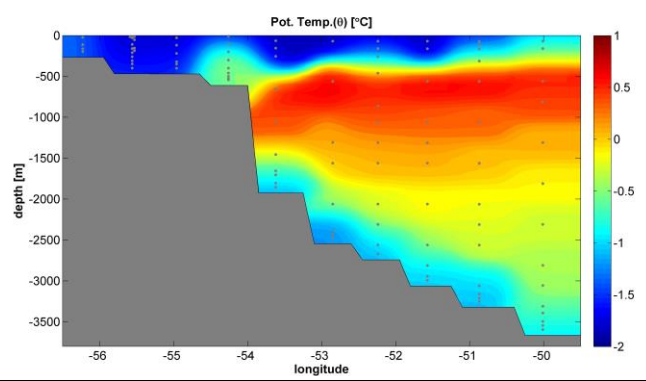
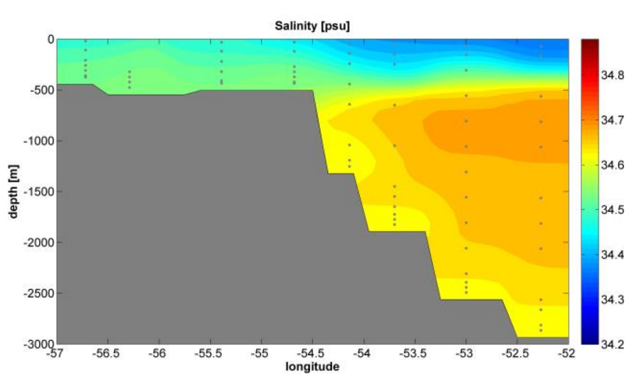	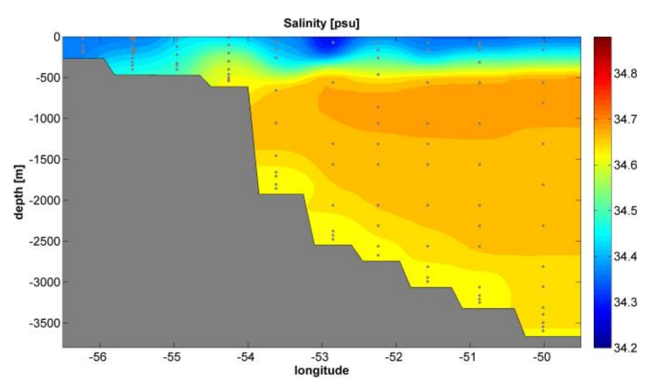

Figure 3.4.3 (continued) The sections of the θ and salinity as a comparison of two strips from ANT 29/3(2013) in left column (LIS1) and right column (LIS2) as shown in blue dots in the maps

The salinity section (LIS1) shows higher salinity (34.7psu) in warmer water east of 53.5ºW in 500m to 1000m depth higher than over the slope (34.6 psu). The western shelf water is even low saline and measured around 34.55 psu in salinity section (LIS1). The Salinity section (LIS2) also shows high salinity in warmer water 34.7psu east of 52.5ºW in 500m to 1000m depth that is higher than the 34.6psu. The salinity in the shelf water of LIS2 is less than the salinity in the shelf water of the LIS1, and shows some entrainment of low saline water to the shelf of LIS2 probably from the Bransfield Strait.

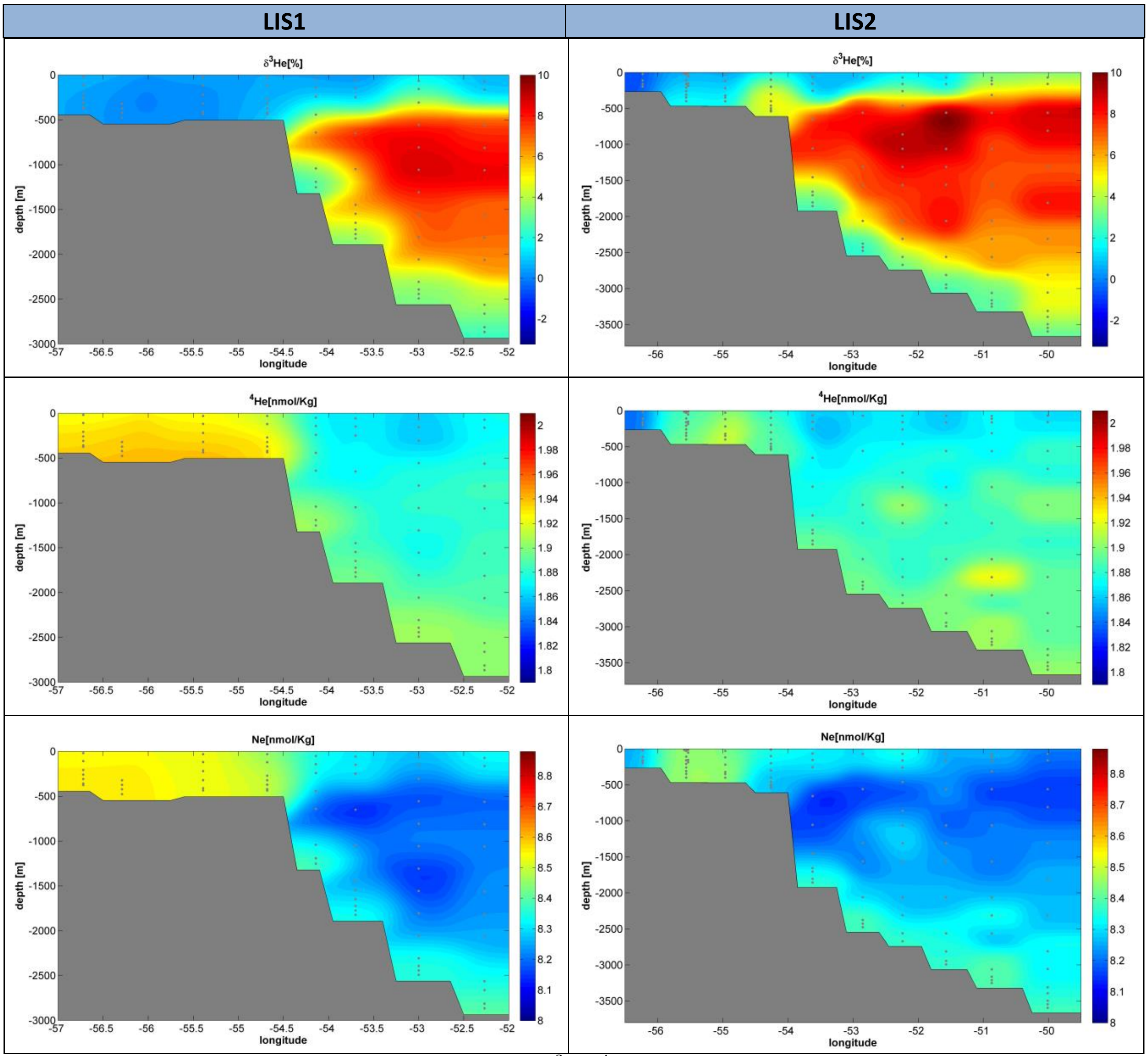

Figure 3.4.3 (continued) The sections of the tracers δ^3He, ^{4}He and Ne as a comparison of two strips from ANT 29/3(2013) in left column (LIS1) and right column (LIS2) as shown in red dots in the maps.

The δ^3He in LIS1, the highest is with 8% in 1000m depth at 53ºW and lower (δ^3He < 0.3%) in the western edge of the section on the shelf. The δ^3He (LIS2) is highest with 10% in 600m depth at 51.5ºW, which is a little higher than on LIS1, because it penetrates further into the inner basin and, hence, into the WDW. The lowest δ^3He is in the western edge of the section on the shelf around -1.8% (close to surface equilibrium value).

The ^{4}He (LIS1) is 1.94 nmol/kg in western shelf water and decreases fast down the slope to 1.90 nmol/kg in the bottom. The Ne section (LIS1) shows the similar distribution as ^{4}He with 8.56 nmol/kg in the western shelf water and 8.40 nmol/kg in bottom water. The ^{4}He and Ne sections (LIS2) both show a decrease down the slope. The ^{4}He section (LIS2) shows a decrease from 1.92 nmol/kg on the shelf at 55.5ºW to 1.89 nmol/kg down the slope at 3000m depth. The Ne section (LIS2) also shows the decrease from 8.45 nmol/kg on the shelf to 8.35 nmol/kg down the slope at

3000m depth. There is strange occurrence of ^4He up to 1.93 nmol/kg at 50ºW to 52.5ºW in 1000m to 2500m depth, that is relevantly higher than the ^4He measured over the slope, but the Ne measurement at the same location does not show higher Ne than the Ne measured over the slope.

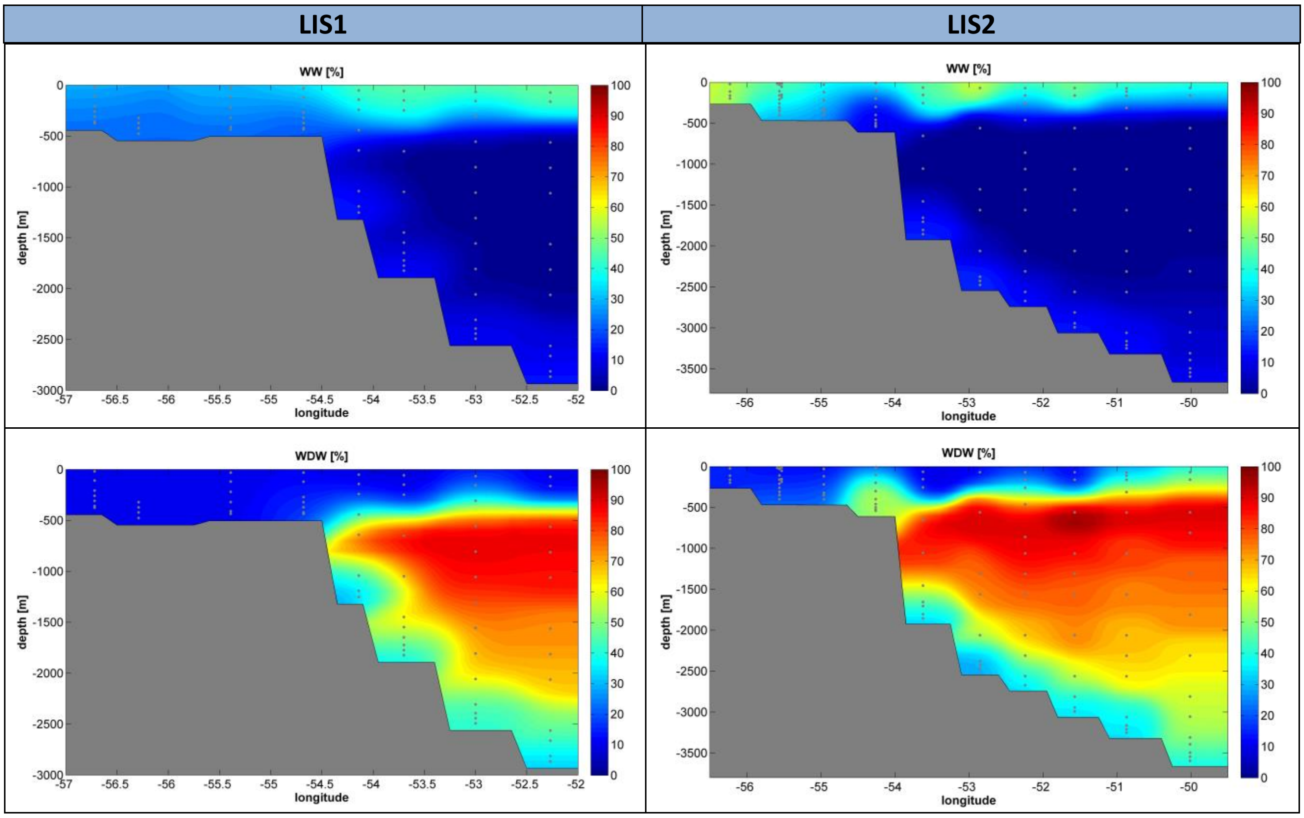

Figure 3.4.3 (continued)The sections of the WW and WDW as a comparison of two strips from ANT 29/3(2013) in left column (LIS1) and right column (LIS2) as shown in red dots in the maps.

The WW section (LIS1) does not show WW > 25% in the shelf water but east of 54.5ºW the WW is observed around 50%, that indicates the mixing or diluting WW with another water mass (possibly HSSW or GMW) on the shelf. In WW section (LIS2), the WW is calculated below 55% in the shelf water i.e. higher than WW of LIS1 on the shelf and might have been caused by the low saline water entrainment from Branfield Strait, the WW layer depth decreases further east with a sudden decrease (around 30%) observed at 54ºW. The WW (LIS2) is observed around 20% over the slope.

In the WDW section (LIS1) the highest calculated WDW is 90% at 53ºW in 1000m depth, the lowest WDW is calculated around 10% in shelf water. The WDW section (LIS1) also demonstrate its mixing with another water mass over the slope, the WDW is not present west of 54.5ºSW. The WDW section (LIS2) shows a WDW layer of around 85% in 500m to 1500m extending to 53.8ºW and the highest is calculated around 95% at 51.5ºW in 600m depth. The further extent of WDW west of 53.8ºW without noticeable decrease is caused by the lack of data.

The HSSW (LIS1) is around 65% in shallow water and decreases down the slope to 50% in the deep basin due to mixing with WDW. The HSSW (LIS1) mixes with WW on the shelf until it slopes down. The HSSW section (LIS2) does not show fast decrease along the slope and show almost similar HSSW fraction around 55% from westward shallow water down to the slope except in bottom water at 50ºW where HSSW is 45%.

A plume of 0.27% GMW is present on the entire shelf in the GMW section (LIS1), with θ < -1.88ºC. This GMW plume origin is expected to be from LIS that flows northward along the shelf. The GMW plume disappears fast down the slope. This disappearance of the GMW plume can also be traced by the decrease of HSSW, ^{4}He and Ne over the slope down to the bottom in their respective sections (LIS1). Thus, we can assume local WSBW formation at 65ºS in western shelf water of the Weddell Sea.

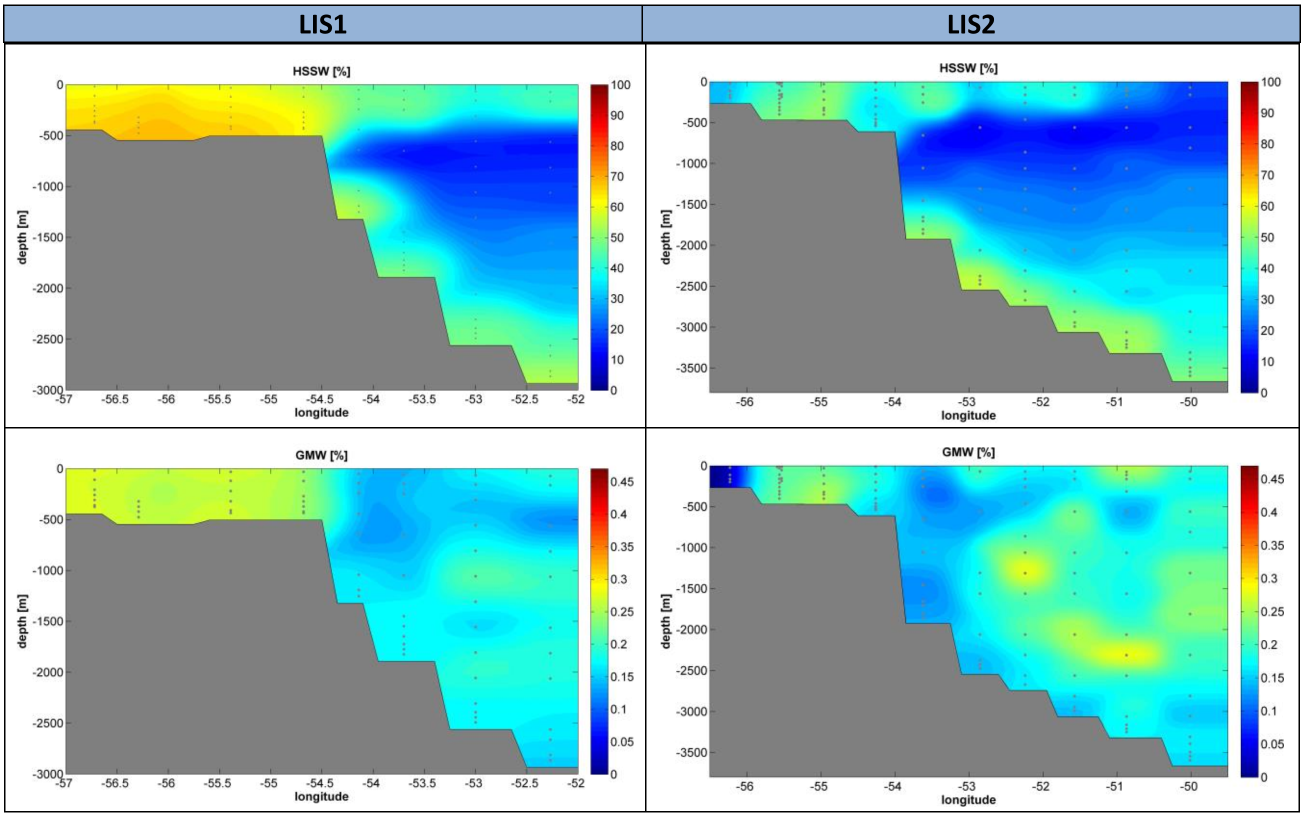

Figure 3.4.3 The sections of HSSW and GMW as a comparison of two strips from ANT 29/3(2013) in left column (LIS1) and right column (LIS2) as shown in red dots in the maps.

A 'strange' GMW plume 0.21% can be detected at 53ºW in 1000m to 2000m depth in the LIS1 GMW section, even higher than GMW on the slope (≈ 0.17%). In contrast, the ^{4}He and Ne are higher over the slope than ^{4}He (1.88 nmol/kg) and Ne (8.15 nmol/kg) at 53ºW in 1000m to 2000m depth. This 'strange' GMW plume at such depth and away from the shelf slope with lower values of ^{4}He and Ne is difficult to explain and might be overestimated by the OMP. The difference of 0.21% of the 'strange' plume and the fractions on the slope of 0.17%, however, is higher than the estimated uncertainty (±0.03%).

The sections Figure 3.4.3 (LIS2) further north of LIS1 at ≈ 64.5ºS from ANT 29/3 (2013) provide a similar scenario as observed in Figure 3.4.3 (LIS1). The GMW section (LIS2) has 0.23% GMW at 55ºW in shelf water and can be traced back to the shelf GMW plume at 56ºW in GMW section (LIS1). The GMW plume here disappears gradually towards the shelf break.At LIS2, another ‘strange GMW’ plume of up to 0.28% (even higher than the strange GMW plume of 0.21% in the LIS1 section) (with HSSW < 20% and WDW is > 80%) appears in 1000m to 2500m depth between 50ºW to 52.5ºW, whereas GMW is below 0.12% over the slope. ^{4}He shows also higher concentration in the plume than over the slope. In contrast, Ne is low than Ne over the slope. The GMW is almost 0% at 56ºW, and might have been caused by the surface water entrainment from Bransfield Strait. The ^{4}He increase in the ‘strange’ GMW plume detected in the GMW section (LIS2) might have been caused by mantle ^{4}He from WDW admixtures. The δ^3He there is of 10% (see δ^3He section) that signal of mantle ^{4}He can also increase ^{4}He 1% by adding mantel ^{4}He but not Ne. Thus, the OMP might have interpreted high ^{4}He as GMW plume as ^{4}He has the highest weight in the OMP than Ne.

Another explanation of the strange GMW plumes in Figure 3.4.3 might have their origin in the warm GMW ≈ 0.37% (in local WSDW) observed in the ISW1’ GMW section Figure 3.4.2 (where ^{4}He is 1.96 nmol/kg at 1200m to 2500m, WDW>70% and HSSW<30%). Therefore we can also conclude from the assumption that the WSDW at LIS makes its way out of the LIS region into the Weddell deep water without enough mixing with underlying cold WSBW, so that WSDW might show even higher GMW fraction than the GMW fraction in WSBW. Thus, the WSDW and WSBW appeared not to mix significantly at smooth bottom topography or due to low turbulence in the bottom water.

It can be concluded that the region of WSDW/WSBW formation has its extent from FRIS till 65ºS of LIS at the Antarctic Peninsula. The locally formed WSDW/WSBW in LIS mixes with WSBW flowing from FRIS along the slope.

3.5 The Weddell Transect and the Prime Meridian Sections

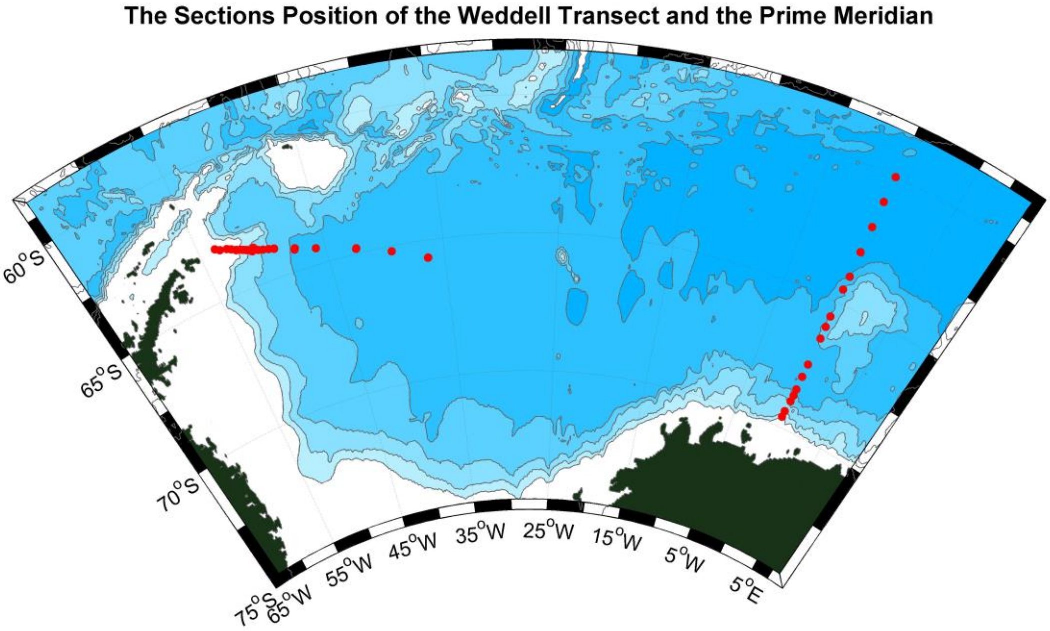

Figure 3.5.1 The sections map (red dots) of the sections Weddell Transect and the Prime Meridian in the Weddell Sea.

In the map (Figure 3.5.1) two sections are analyzed. One along the Weddell Transect (almost parallel to LIS2 but further north and extending further into the basin almost to the center of the Weddell Gyre) and another along the Prime Meridian (leading from the Antarctic Continent touching the western flank of Maud Rise to 60°S). The sections are helpful to investigate the Weddell Sea inflow and outflow. The Weddell Transect section consist of ANT 15/4 (1998) with ANT 10/4 (1992) data. The Prime Meridian section consist data from only ANT 15/4 (1998). This might help to disregard any possible temporal changes between the sections.

3.5.1 The Weddell Transect Section

The sections below Figure 3.5.2 are interpolated from the data of ANT 10/4 (1992) and ANT 15/4 (1998) as shown in the map (red dots). The section has been termed as Weddell Transect. The Weddell Transect is expected to demonstrate the WSBW out flow to the northeast from where shallower water masses (WSDW down to max. 2000 m) may escape the Weddell Basin across the South Scotia Ridge and the deeper water masses (WSDW and WSBW below 2000 down to the bottom) circulate eastwards towards the Prime Meridian.

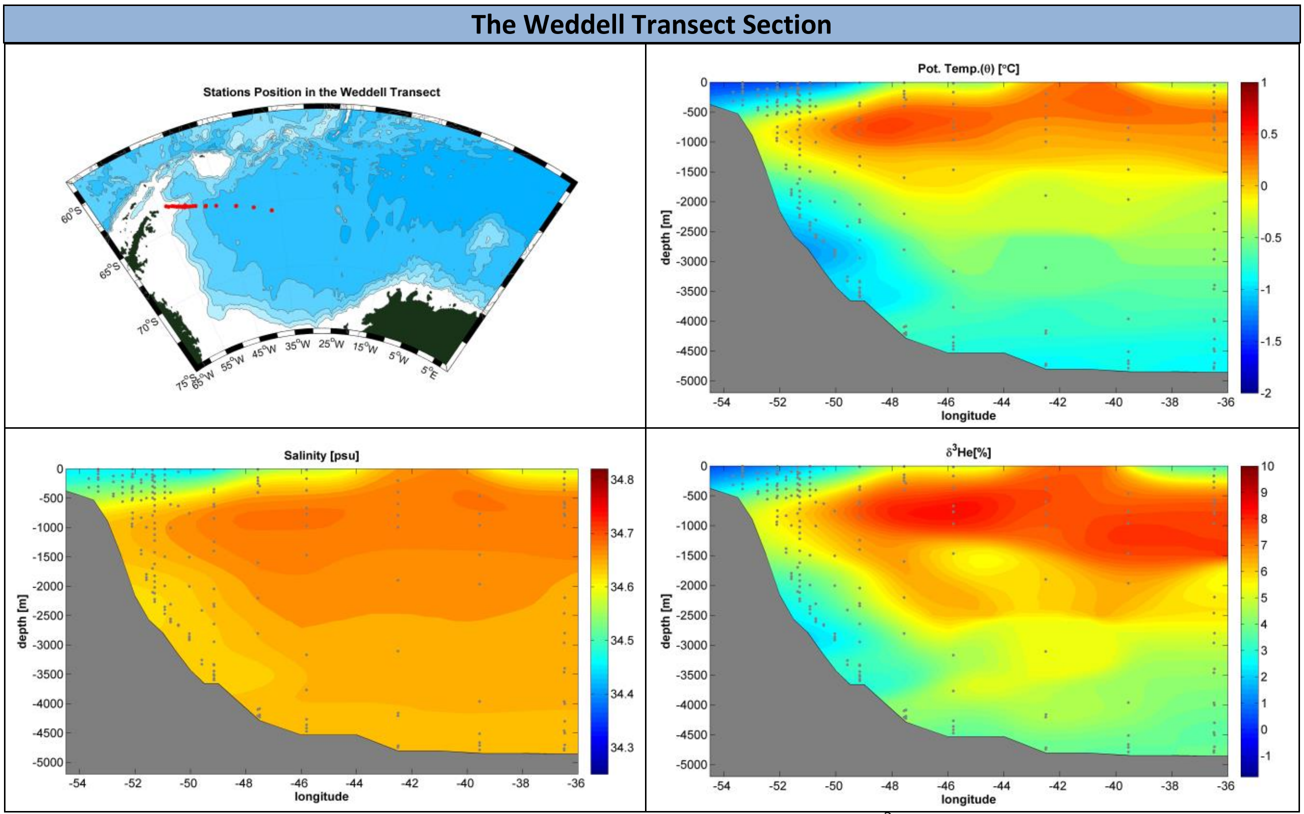

Figure 3.5.2 (continued) The sections map and the parameters (θ, Salinity and δ^3He) in the Weddell Transect as shown in red dots in the maps.

The θ section shows the coldest water on the western shelf with around -1.5ºC. The warmest water is found in the 300m to 1000m depth layer with around 0.3ºC. This warm water layer is stretched up to the surface water at 40.5ºW probably due to lack of vertical data resolution in surface water that the interpolation fails to reproduce the strong temperature gradient. The θ decreases over the slope below -0.7ºC down to the bottom with a sudden decrease (θ = -1.3ºC) observed over the slope at 51ºW. The lowest salinity is also detected in the shelf water around 34.45psu. The rest of the section shows a small gradient of salinity from warm water (34.67psu) to bottom water (34.64psu). There is also a quick decrease of salinity (34.62psu) over the slope at 51ºW.

The δ^3He is observed highest as 8% in the warm water; the lowest δ^3He is measured in the shelf water of around 0.5%. The low δ^3He of 2.5% is also detected at 51ºW over the slope and then increases up to 4% at the bottom.

The ^{4}He section Figure 3.5.3 shows an unexpected signal of 1.90 nmol/kg as the highest measured in the section in 3500m depth at the eastern edge of the section. Another similar ^{4}He signal of 1.87 nmol/kg is also measured in 1500m depth at the same location. Below 500m depth on the slope, ^{4}He is measured around 1.88 nmol/kg; In the bottom water, ^{4}He appears around 1.89 nmol/kg at 46.5ºW and the eastern edge of the section. The Ne section Figure 3.5.3 tends to verify the ^{4}He signal at the slope and in the bottom water, the highest Ne measured is 8.30 nmol/kg in 3000m depth on the slope and then after a decrease, the Ne increases again and is around 8.22 nmol/kg in the bottom water at 46.5ºW and 8.27 nmol/kg at the eastern edge of the section.

The Weddell Transect Section

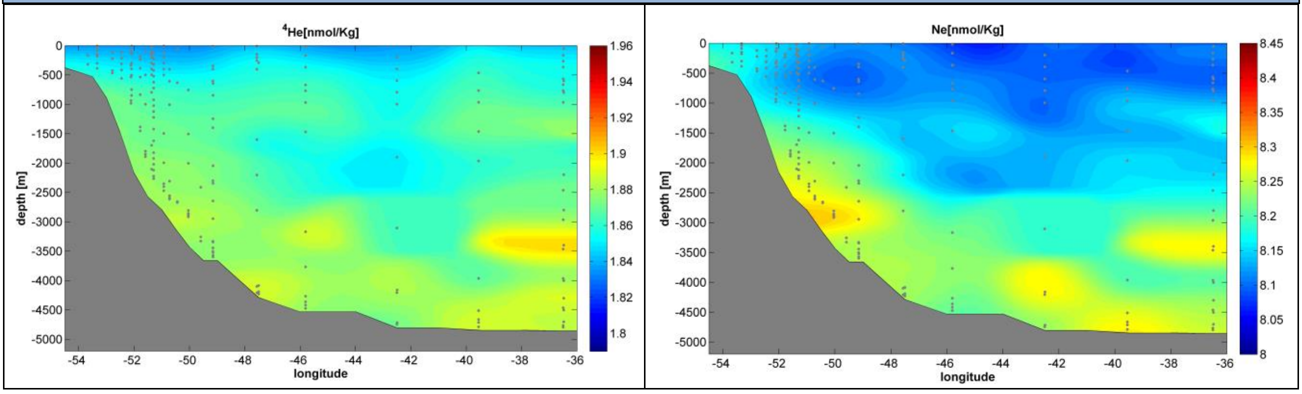

Figure 3.5.3 (continued) The sections the He, Ne in the Weddell Transect as shown in red dots in the maps.

The WW in Figure 3.5.3 is hardly visible in the section except in the shelf water where it is calculated around 40%. WW can also be found up to 20% over the slope and in the bottom water. The WDW in Figure 3.5.3 is calculated up to 85% in 300m to 1200m depth from the eastern edge of the section to 51ºW. The shelf water shows minimum fraction of WDW of about 20%. The WDW decreases fast in 1500m to 3500m depth and is calculated around 30%. The bottom water shows WDW around 40%. The HSSW in Figure 3.5.3 is observed in the shelf water and in the bottom water of the section not higher than 55%. The highest HSSW is calculated 55% in 3000m depth at the slope, the HSSW decreases down to slope with a little increase and observed around 50% in the bottom water at the eastern edge of the section.

The GMW section in Figure 3.5.3shows strange appearance of GMW plumes in 500m to 1500m east of 48ºW. Theses GMW plumes are not supported by Ne signal, except a weak ^{4}He signal in ^{4}He and Ne sections (probably caused by the high δ^3He that contains additional mantel ^{4}He). Nonetheless, along the Weddell Transect (relatively far off the sources of FRIS and LIS) the signal-to-noise ratio of the parameters might be too low to allow the OMP to distinguish unambiguously between pure GMW and other water masses with similar properties. Even with a variation of the OMP weighting factors (where weight factor of Ne was above 1000), it was not possible to obtain a "clearer" result for GMW along the Weddell Transect. However, 'expected' GMW plumes over the slope and in the bottom water are supported by the ^{4}He and Ne signals at the same position (see ^{4}He and Ne sections). The low GMW fraction of calculated 0.07% in 2500m depth over the slope is underestimated in the OMP despite the clear Ne signal (the highest signal in the entire Weddell Transect Ne section); this representation of GMW cannot be explained precisely. This low calculated GMW effect can also be spotted in the GMW map (the GMW map used all data in interpolation) along Weddell Transect at 50ºW.

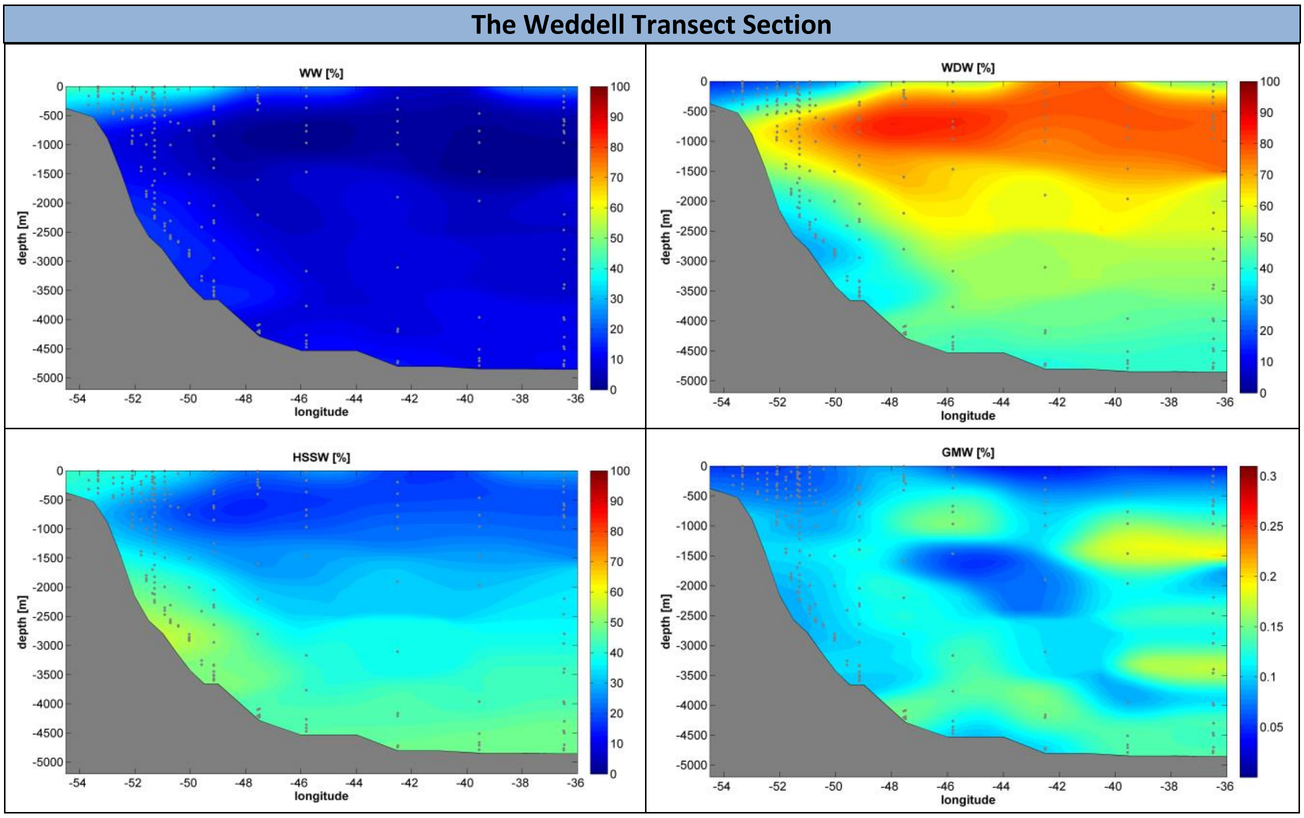

Figure 3.5.2 The sections of WW, WDW, HSSW and GMW in the Weddell Transect as shown in red dots in the maps.

From the Ne data, we can expect a high GMW plume over the slope and we can associate this as LIS' local GMW plume in the WSBW (θ < -0.7ºC) as we also observed clear Ne signal over the slope up to 46ºW in LIS1 and LIS2 (Figure 3.4.3). The GMW plume 0.15% with clear Ne signal observed in the bottom water east of 48ºW of the section can be associated to the FRIS' GMW plume in the WSBW (θ < -0.7ºC) or the contribution of both ice shelves (FRIS and LIS).

3.5.2 The Prime Meridian Section

The sections Figure 3.5.3 below have been interpolated from the data of ANT 15/4 (1998) at Prime Meridian from the continental shelf to 60ºS. The Maud Rise is located at 65ºS, with its center around 3ºE, at a distance of 125Km east of the section. The data from other cruises available at Prim-Meridian are excluded to avoid interference from temporal variability in the interpolation.

The highest θ of about 1ºC observed from 65.5ºS to 64.5ºS in 300m depth (Figure 3.5.3), such high θ in such shallower depth might have been interpolated due to existence of fewer data points above 0.5ºC (the highest is 1.27ºC in 163m depth) in upper 200m at the same location. The warm water layer > 0ºC reaches down to 1700m depth. The lowest θ below -1.3ºC is measured in continental shelf water. The θ decreases fast from 0ºC to -0.8ºC at the northern edge of the section, the bottom water at the same location indicates the flow of cold bottom water (WSBW). The salinity Figure

3.5.3 is around 34.7psu from 67.5ºS to 63.5ºS in 500m depth, the lowest salinity around 34.4psu is measured in continental shelf water. The salinity section does not show a strong gradient below 500m depth is around 34.65psu at the northern edge of the section in the bottom water. The δ^3He Figure 3.5.3 is highest at 10% in the warm water layer found at 66.5ºS in 500m depth, δ^3He at the northern edge of the section is around 2.5% in the bottom water. The lowest δ^3He is observed in continental shelf water of about 0% (The surface water is in equilibrium at -1.8%).

The Prime Meridian Section

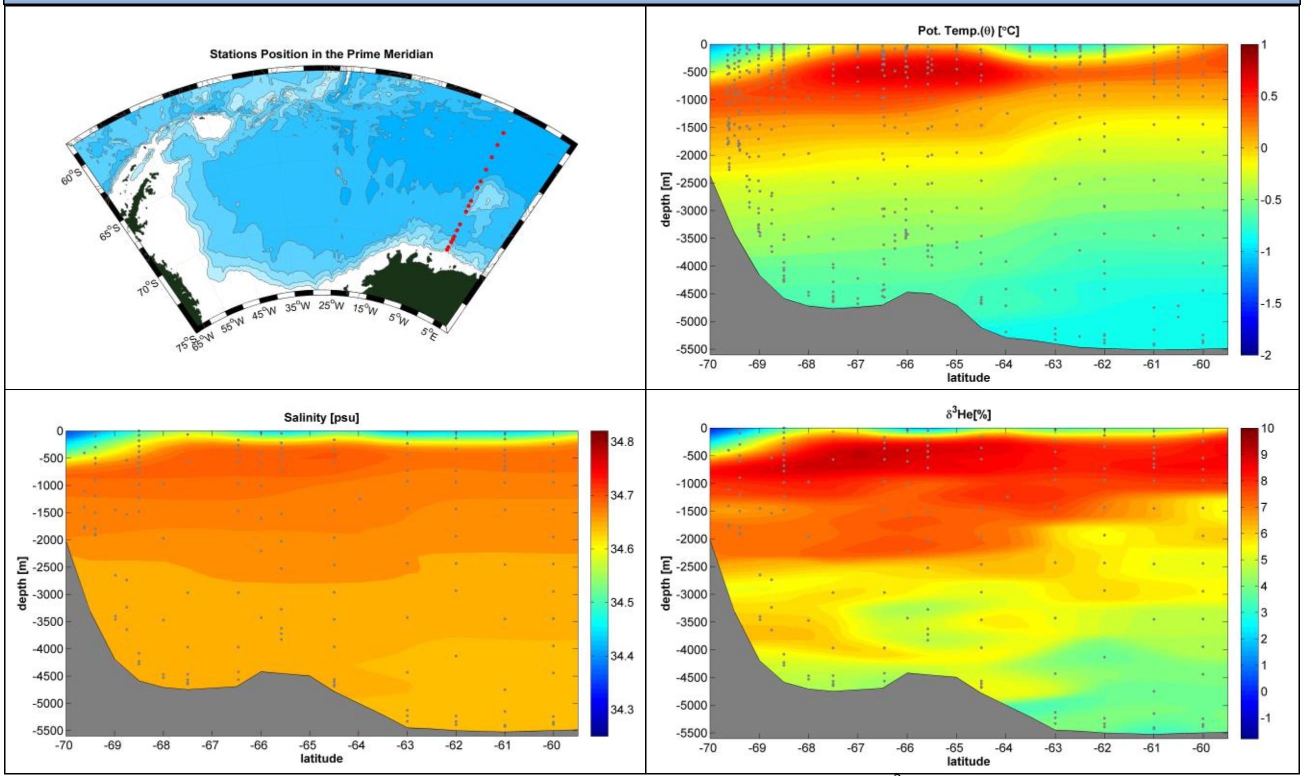

Figure 3.5.3 (continued) The sections map and the parameters (θ, Salinity and δ^3He) of the Prime Meridian as shown in red dots in the maps.

The ^{4}He section in Figure 3.5.3 shows the highest ^{4}He in the bottom water at the northern edge around 1.90 nmol/kg distributed in a depth from 3200m to the bottom of the section. Another ^{4}He signal around 1.88 nmol/kg is also observed in the bottom water at 67.5ºS. Therefore, we can recognize a flow of GMW in the bottom water of the section. The continental shelf does not show significant ^{4}He in its water. Therefore local GMW is not recognized. The surface water is 1.79 nmol/kg i.e. equivalent to surface equilibrium at 65.5ºS. The Ne section in Figure 3.5.3 does confirms the same pattern i.e. higher NG concentration in the bottom water. Ne up to 8.30 nmol/kg is measured at the northern edge of the section in the depths of 3000m to the bottom. Another Ne signal of around 8.25 nmol/kg is measured in the bottom water at 67.5ºS. The surface water is of 8.0 nmol/kg i.e. below surface equilibrium at 66ºS.

The Prime Meridian Section

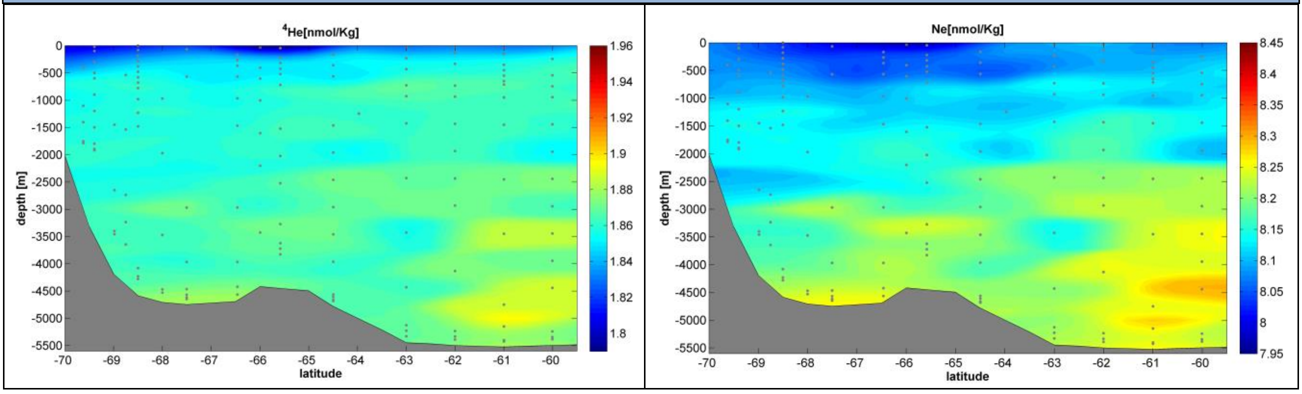

Figure 3.5.3 (continued) The sections the He, Ne of the Prime Meridian as shown in red dots in the maps.

The WW in Figure 3.5.3 is only noticeable in shelf water up to 55%. WW in bottom water is calculated below 20%. The WDW around 95% is dominant from 63.5ºS to 68ºS in 200m to 800m depth. The WDW fraction decreases fast below 1500m depth to around 35% in the bottom water at the northern edge of the section. The lowest WDW fraction is below 20% in the shelf water.

The HSSW in Figure 3.5.3 is found nowhere higher than 50% and indicates a HSSW flow around 50% in the bottom water at northern edge of the section. The HSSW in the bottom water at 67.5ºS is around 40%. The surface water including continental shelf water is below 25%, the least HSSW < 5% is calculated in 200m depth from 63.5ºS to 68ºS, i.e. the where WDW is dominant.

The GMW section in Figure 3.5.3 shows a patchy distribution of the GMW fractions throughout the section and is difficult to explain in 500m to 1000m depth at the northern edge of the section, the GMW of 0.16% is not supported by high ^{4}He and Ne at this location. Here, the signal-to-noise ratio of the parameters might also be too low to allow the OMP to distinguish unambiguously between pure GMW and other water masses with similar properties (see GMW section along the Weddell Transect, Fig. 3.4.3). Hence, we focus on the GMW fractions below 2000m where we have observed significant ^{4}He and Ne signals (see ^{4}He and Ne sections).

A GMW plume is observed around 0.14% in the depth of 3000m to the bottom from 69.5°S to 67.5ºS, since it is closer to the continental shelf but cannot be expected the local GMW plume due to smaller size of the shelf and existence of the GMW plume in the greater depth. We assume this GMW plume as inflow from Eastern Antarctica Ice Shelves (EAIS).

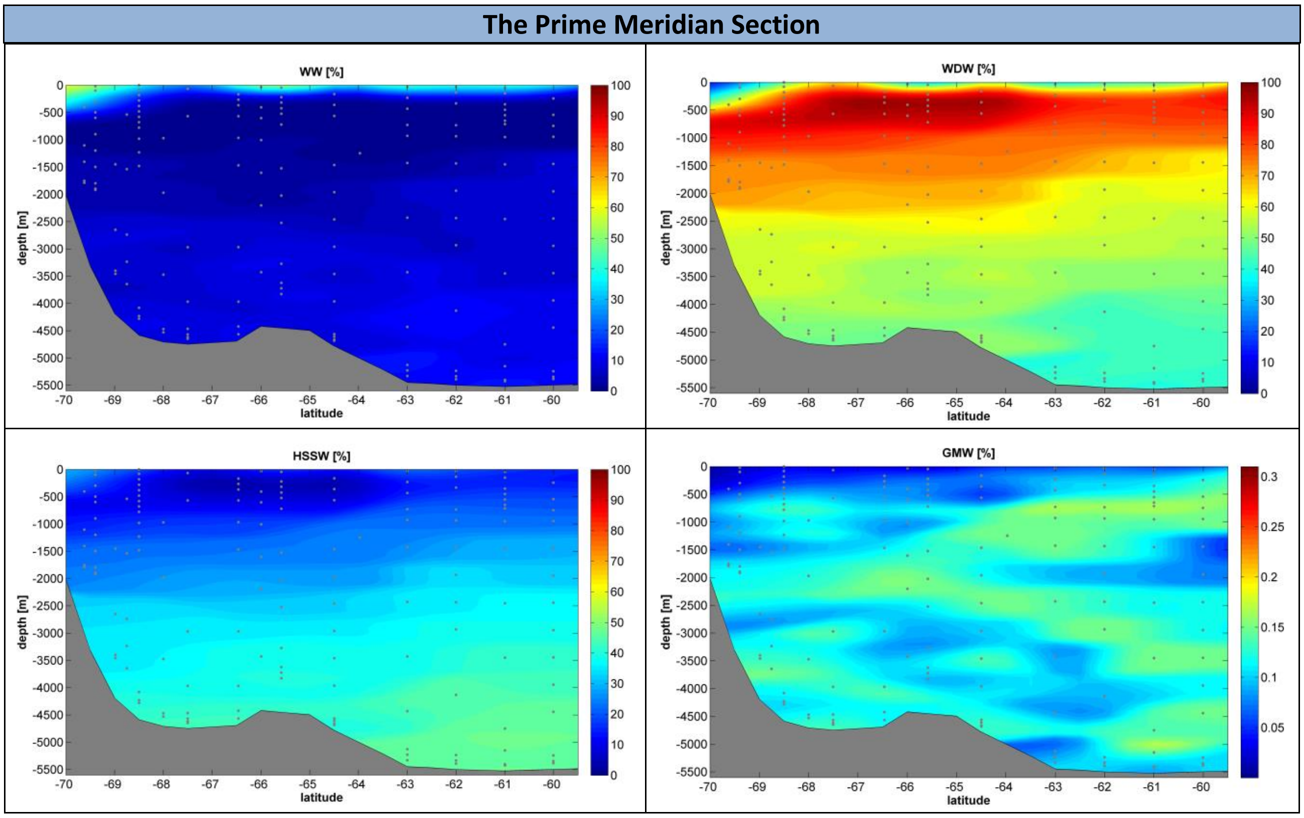

Figure 3.5.3 The sections of WW, WDW, HSSW and GMW of the Prime Meridian as shown in red dots in the maps.

Another plume of GMW 0.14% is found at 65.5ºS in intermediate depth of 1500m to 2500m. The existence of GMW in such intermediate depth off the shelf might be related to upwelling initiated by Maud Rise 125km east (upstream) of the section. Such a seamount causes the ocean waters to undergo vertical mixing. Maud Rise might have lifted the cold bottom water from EAIS and to mix it with overlaying WDW. Indeed, this GMW plume is warmer (-0.2ºC) than the rest of the GMW plumes below 2000m depth. Another evidence for upwelling water due to Maud Rise can be seen in WDW section. The WDW seems to be is pushed upwards into shallow layers at the same location.

In the northern edge of the section the water below 4000m depth shows the highest calculated GMW of 0.17% (WSBW < -0.7ºC), and apparently separate GMW plume at the same location in 3500m of 0.15% (WSDW > -0.7ºC). These GMW plumes are assumed to be the outflow from the Weddell Sea towards after considering the bathymetry and the pathway of the Weddell Gyre.

Note that the eastward outflow has higher GMW fractions than the westward inflow from the EWIS in the slope, clearly indicating that the Weddell Sea is a source for GMW. Also HSSW is still high in the out flowing WSBW.

The bottom water of the Prime Meridian northern edge can be associated to eastern edge of the Weddell Transect section. The both edges are almost 1750Km apart, but both bottom waters show similar GMW fraction of 0.15% and 0.17% (with uncertainty of ± 0.03%). Therefore, we can assume that the most of the WSBW identified in the Weddell Transect section is flowing eastward without significant dispersal to other direction as identified in the Prime Meridian section.

4. Summary and Discussion

The Weddell Sea hydrographic and noble gas data from 17 research expedition have been used to perform an Optimum Multiparameter analysis to investigate the water mass distribution in the regions of the Weddell Sea. During the ‘regional’ property plots analysis in chapter 3.1, the FRIS has shown well identified ISW (-2.3°C) and HSSW (34.88psu) with distinctly high ^{4}He and Ne. However, the LIS water did not show strong evidence of ISW and HSSW. The EWIS water indicate no contribution of HSSW and ISW formation and the water mass distribution look like Weddell Deep water. The ACC water and FRIS water are found both with $^{4}He/Ne$ ratios higher than the surface water equilibrium. The $^{4}He/Ne$ ratio shows a positive correlation with Ne in FRIS water and negative correlation in ACC water. The high $^{4}He/Ne$ ratio in FRIS water indicates an addition of ^{4}He or a ‘lower input’ of Ne by GMW. The extra addition of ^{4}He might be due to radiogenic (crustal) ^{4}He and the ‘lower input’ of Ne is due to different differential diffusion of noble gasses in glacial ice during its formation. On the other hand, there is no additional source of Ne in ACC and the addition of ^{4}He in ACC is due to mantel (primordial) ^{4}He from hydrothermal vents in the Pacific. However, the addition of ^{4}He is calculated as about 4.5% in FRIS and 5.4% in ACC.

The bottom layer maps in the chapter 3.2 show the FRIS region with the coldest and most saline (-2.2ºC, 34.88psu) bottom water followed by the LIS region. The maximum ^{4}He and Ne are observed at the FIS front due to high basal melting below FRIS, and the lowest ^{4}He and Ne are measured in the EWIS region. The lowest WDW and highest HSSW are observed at FRIS, but at the Filchner Slope the WDW increases and HSSW decreases fast down the slope. The GMW plume is observed at the FIS front over the Filchner Trough and can be traced flowing down the Filchner slope.

The sections analysis in Chapter 3.3 gives a broader understanding of hydrographic and noble gas parameters and the water masses distribution in vertical sections. The RIS front shows the highest calculated HSSW at its western edge with almost negligible presence of WDW. The RIS also shows an expected ISW recirculation at its western edge over Ronne Basin and a GMW feedback from the FIS at its eastern edge. The southern-most section in front of FIS shows the highest measured ^{4}He and Ne, and hence the highest calculated GMW fraction at 1000m depth. This GMW plume in ISW (HSSW+GMW) is identified as ‘trapped ISW’ below 800m in the Filchner Trough. This ISW keeps recirculating and undergoes repeated mixing with newly formed ISW unless it becomes less dense enough to stratify over the 'trapped ISW'. The 'trapped ISW' is also identified as the ISW core from its θ, Salinity and ^{4}He values. In addition a second ISW core is also located east of the FIS front.

The temporal comparison (1995 and 2014) of the two longitudinal sections across the Filchner Trench nearer to the Filchner shelf break shows a significant decrease of the salinity in the bottom water and in the surface water with increased WW. Additionally, HSSW decreases in the bottom water without visible increase of WDW. The bottom water in 2014 shows higher Ne and a second GMW plume which was not observed in 1995, regardless the dispersal effect as FRIS14 is 35km further north of FRIS95. Therefore, the freshening of the bottom water is due to increased basal melting and possibly sea ice melting and/or less sea ice formation within the 20 years interval. The temporal freshening and increase of basal melting of the FRIS bottom water verify the Timmermann & Hellmer 2013 in the Chapter 1.6, in which they have shown decrease of salinity in the Weddell Shelf water and increase of basal melting in FRIS in recent century, particularly, the FESOM (HadCM3) shows frightening freshening of the Weddell Shelf and FRIS basal melting in 22nd century.

The eastern section (FRIS30) on the Filchner Slope shows almost equally fractions of WW and HSSW in the upper 400m. And a small fraction of GMW in the shelf water, but it does not show a clear flow down to slope. However, it does show an unexpected GMW plume in the warmer water. Here, we observed a second GMW plume in the northern bottom water and recognized it as inflow from the EWIS. On a section further, to the west (FRIS35) on the Filchner Slope, the GMW flows from the shelf water down to slope where the GMW plume losses its fraction fast. The GMW map had also shown a fast decrease of GMW from the FRIS front to the Filchner Slope.

Since, there is lack of data between FRIS and LIS, no clear GMW flow is observed between the FRIS and the LIS. Therefore, more data is required between the FRIS and the LIS to analyze the effects of FRIS on LIS. However, in the GMW map and in the ISW-1 section, the LIS shows a sudden increase of GMW in its southern bottom water and indicates the FRIS GMW entrainment. However, the highest calculated GMW of 0.35% with high ^{4}He and Ne is found in the warm water in the ISW-1section indicating LIS basal melting and mixing with mWDW. A cold GMW plume ($\theta < -0.7$°C) is also observed in the ISPOL section. Therefore it is concluded that the LIS shares the contribution in WSDW and WSBW with the FRIS. The LIS also shows a prominent GMW plume of 0.27% in its northern edge at 65°S. It is another evidence of local GMW formation in LIS northern shelf water but the GMW plume disappears fast over the slope.

For the Weddell Sea inflow and outflow, two sections, one at the Weddell Transect and one at the Prime Meridian were analyzed. The Weddell Transect shows a clear signal of Ne, ^{4}He and HSSW at subzero temperature on the slope at 50.2°W, but the OMP is unable to show significant fractions of GMW at the same position, rather than the OMP shows the highest GMW fraction in WDW in 1200m depth where clear Ne and ^{4}He signals were not observed. This inconsistency is regarded as an OMP problem that needs to be taken into account to avoid underestimation of GMW in this region, and more investigation is required to solve this OMP consistency. However, the locations of the high Ne and ^{4}He on the slope and bottom along the Weddell Transect clearly indicate the 'expected' GMW plumes and can be distinguished as bottom water outflow from the Weddell Sea, where LIS' originating WSBW is recognized west of 48°W and FRIS' WSBW east of 48°W.

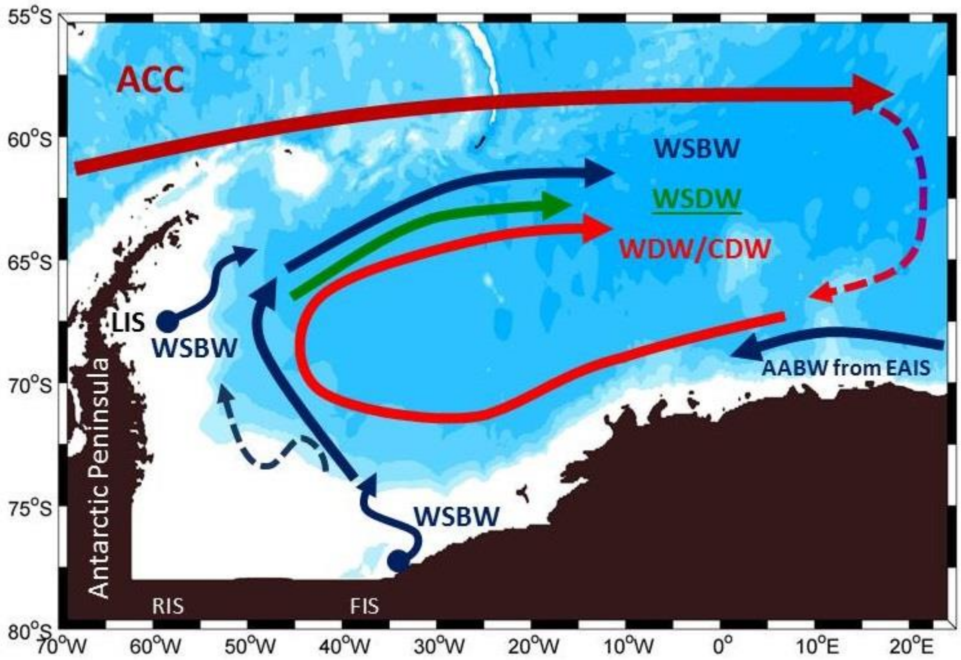

Figure 4.1.1 The Weddell Sea map showing the general circulation in schematic way of arrows of different colors for different water masses (red: ACC, blue: WSBW, orange: WDW/CDW and green: WSDW), where light blue dashed arrow shows FRIS bottom water entrainment to the LIS slope and orange dashed arrow shows turning of ACC into the Weddell Sea.

The GMW fraction in the bottom water at the eastern edge of the Weddell Transect corresponds to the GMW fraction in the bottom water at the northern edge of the Prime Meridian section. Thus, the WSBW outflow across the Weddell Transect is also observed in the Prime Meridian section. However, the GMW fraction at the bottom south of Maud Rise is recognized as an inflow from EAIS, because EWIS are observed with almost no sign of local GMW formation. In the light of above analysis the general circulation in the Weddell Sea is depicted in the map (Figure 4.1.1).

5. Conclusion

From the available hydrographic and noble gas data and the OMP method, it can be deduced that the FRIS is the largest contributor in WSBW formation, inferred from the highest fractions of GMW. The Filchner Slope is the site where most of the WSBW is formed. A 20 year temporal analysis indicated freshening of FRIS bottom water and increased basal melting. The flow of WSBW from the FRIS is propagated north-westward along the slope. The LIS analysis makes also the LIS contribution in WSDW/WSBW formation certain. The observed spatial distribution and temporal variability of GMW formation can be used to improve sophisticated models like FESOM (see 1.6) to allow more precise future projections of GMW formation in the Weddell Sea. However, the OMP method might require improvement e.g. because of the detected inconsistent results in calculating GMW fractions further downstream of the source regions. The FRIS bottom water entrainment to the LIS observed in ISW-1 may also be used for future prediction of LIS basal melt as coupling with FRIS in Timmermann & Hellmer 2013 results. Further in-situ observations including bathymetric data in the Southern Ocean is inevitable for assessing the precise future oceanic behavior.

6. Outlook

There is still a need to improve OMP by investigating and identifying the drawbacks of the OMP. I also would like to suggest the new high resolution measurements at the immediate LIS front (latitudinal sections at LIS front and longitudinal sections at the LIS slope), in the region between LIS and FRIS (section across the slope), in the region between FIS and RIS (latitudinal section), and one section each at the Weddell Transect and at the Prime Meridian as shown in the Figure 6.1.1, which should be carried out in the future Antarctic research expeditions. There is still sufficient work remaining to extend and complete the analysis of water mass formation and distribution in the Weddell Sea. To calculate GMW formation and transport rates, velocity data or water mass ages are requires. The latter could be determined by (existing and future) transient tracer observations (e.g. CFC, SF6). That extent of the analysis in the given time was not possible. The detailed data of ice shelves cavity geometry and topography is also required to precisely identify the GMW plume trajectory.

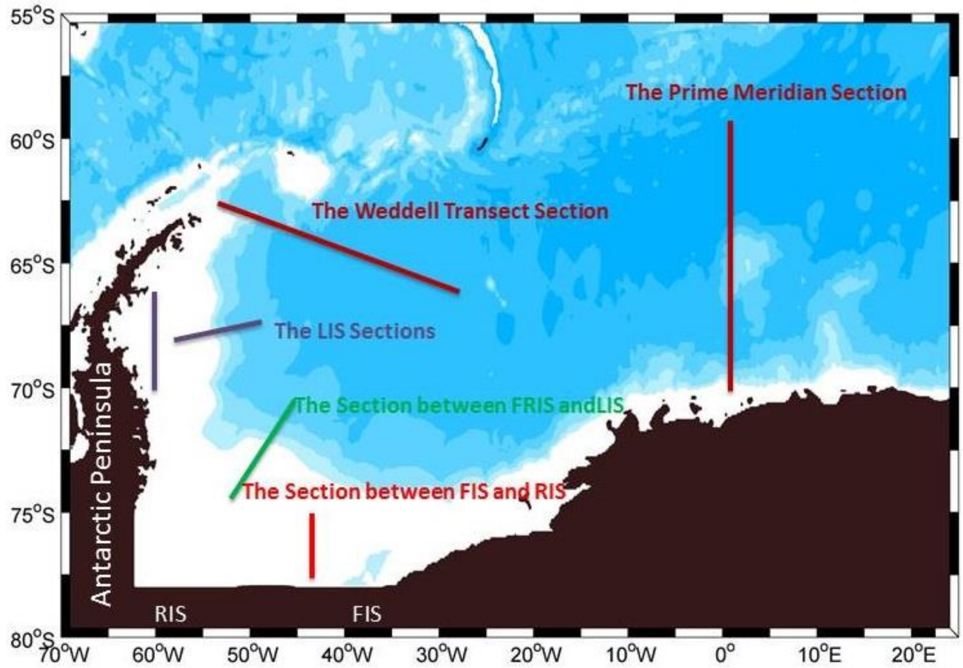

Figure 6.1.1 The proposed sections for the future expeditions in the Weddell Sea (different colors for different sections are labeled accordingly in the figure); where high resolution single year data are required to analyze the water masses distribution and quantification.

In future, further physical analysis of noble gases addition, depletion and their solubility anomalies differences in different physical environment should also be investigated to distinguish the atmospheric noble gases in the seawater from the non-atmospheric noble gases addition (e.g. crustal ^{4}He and mantel ^{4}He from atmospheric ^{4}He).

7. Appendix

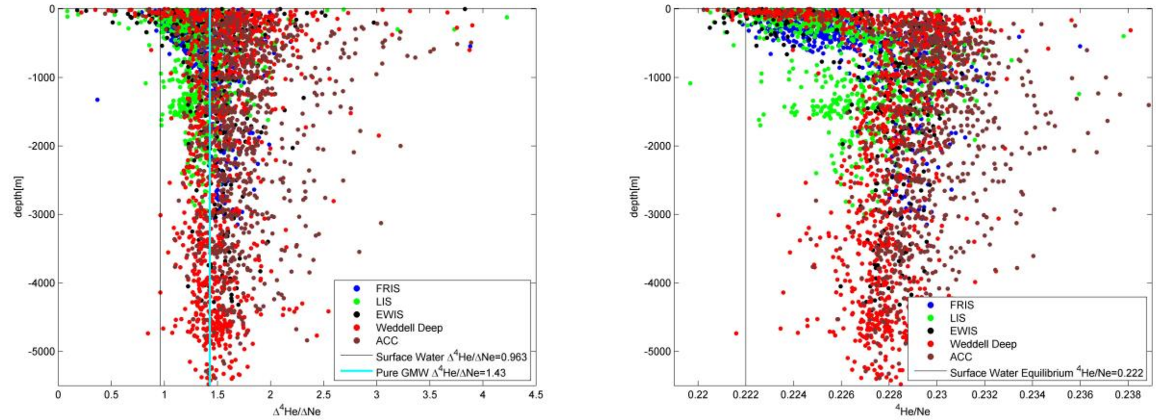

Figure 7.1.1 The depth-Δ4He/ΔNe plot (left) of distributed regions in the Weddell Sea where the black vertical solid line shows surface water value of Δ4He/ΔNe. The light blue vertical line shows pure GMW value of Δ4He/ΔNe. The depth-4He/Ne plot (right) of distributed regions in the Weddell Sea, where the black vertical solid line shows surface water equilibrium value of 4He/Ne.

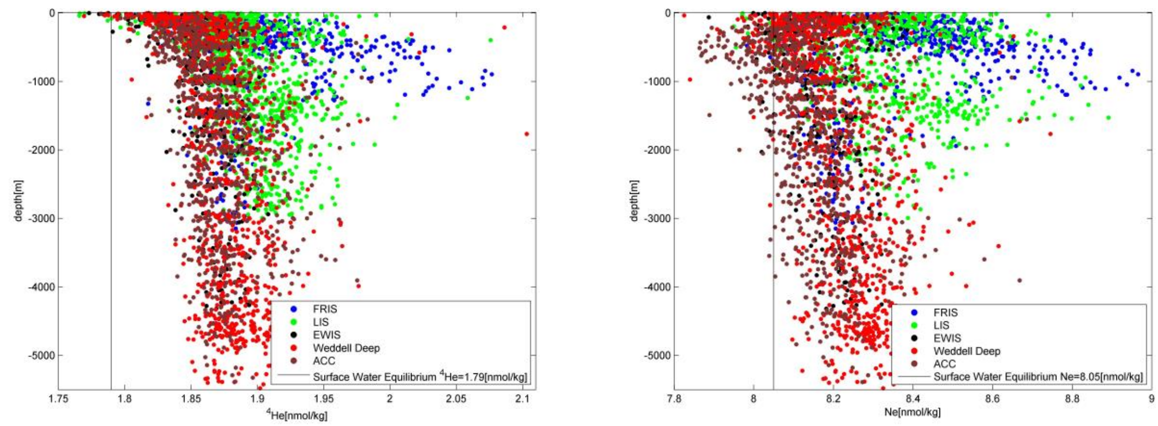

Figure 7.1.2 The depth-4He plot (left) of distributed regions in the Weddell Sea where the black vertical solid line shows surface water equilibrium value of 4He. The depth-Ne plot (right) of distributed regions in the Weddell Sea, where the black vertical solid line shows surface water equilibrium value of Ne.

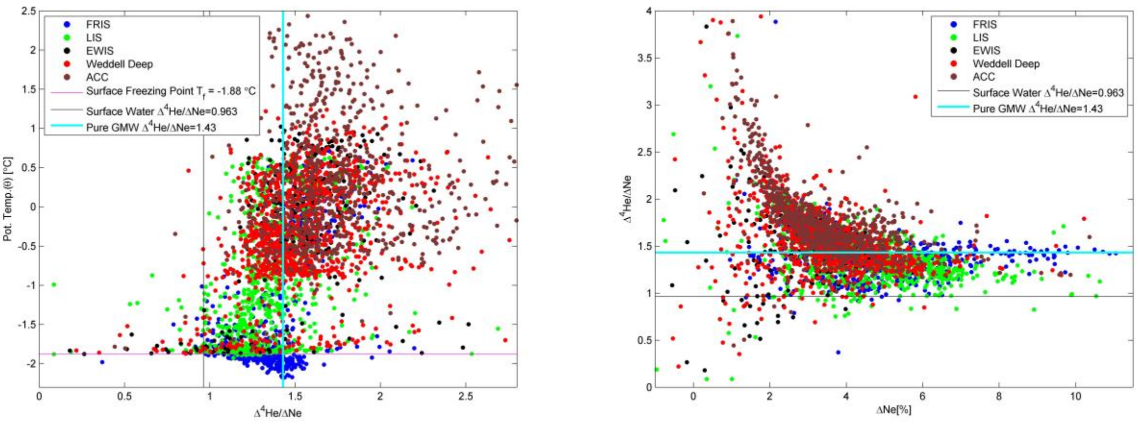

Figure 7.1.3 The θ-Δ4He/ΔNe plot (left) of distributed regions in the Weddell Sea where the black vertical solid line shows surface water value of Δ4He/ΔNe, the light blue vertical line shows pure GMW value of Δ4He/ΔNe and the magenta horizontal line shows the surface water freezing point. The Δ4He/ΔNe-ΔNe plot (right) of distributed regions in the Weddell Sea, where the black horizontal solid line shows surface water value of Δ4He/ΔNe and the light blue horizontal line shows pure GMW value of Δ4He/ΔNe.

8. References

Allison, I. et al., 2013. *IPCC Chapter 4: Cryosphere*, Available at: http://www.ipcc.ch/pdf/assessment-report/ar5/wg1/WG1AR5_Chapter04_FINAL.pdf.

Bulister, J.L., Rhein, M. & Mauritzen, C., 2013. Ocean Circulation & Climate. In *International geophysics*. pp. 227–249. Available at: http://medcontent.metapress.com/index/A65RM03P4874243N.pdf.

van Caspel, M. et al., 2015. Precursors of Antarctic Bottom Water formed on the continental shelf off Larsen Ice Shelf. *Deep-Sea Research Part I: Oceanographic Research Papers*, 99, pp.1–9. Available at: http://dx.doi.org/10.1016/j.dsr.2015.01.004.

Foldvik, A. et al., 2004. Ice shelf water overflow and bottom water formation in the southern Weddell Sea. *Journal of Geophysical Research*, 109(C02015), p.doi:10.1029/2003JC002008.

Foldvik, A. & Gammelsrød, T., 1988. Notes on Southern Ocean Hydrography, Sea-Ice and Bottom Water Formation. *Palaeogeography, Palaeoclimatology, Palaeoecology*, 67(1–2), pp.3–17.

Foldvik, A., Gammelsrød, T. & Tørresen, T., 1985. Circulation and Water Masses on the Southern Weddell Sea Shelf. *American Geophysical Union, Washington, D. C.*, 43, pp.5–20.

Foster, T.D. & Carmack, E.C., 1976. Frontal zone mixing and Antarctic Bottom water formation in the southern Weddell Sea. *Deep-Sea Research and Oceanographic Abstracts*, 23(4), pp.301–317.

Gordon, A.L., 2013. Bottom Water Formation. *Reference Module in Earth Systems and Environmental Sciences*, (1995), pp.1–6. Available at: http://linkinghub.elsevier.com/retrieve/pii/B9780124095489040197.

Gordon, A.L., 1993. Weddell Sea exploration from ice station. *Eos, Transactions American Geophysical Union*, 74(11), pp.121–126.

Hellmer, H.H. et al., 2011. On the freshening of the northwestern Weddell Sea continental shelf. *Ocean Science*, 7(3), pp.305–316.

Hellmer, H.H. et al., 2008. The ISPOL drift experiment. *Deep-Sea Research Part II: Topical Studies in Oceanography*, 55(8–9), pp.913–917.

Hinrichsen, H.-H. & Tomczak, M., 1999. Optimum multiparameter analysis of the water mass structure in the western North Atlantic Ocean. *Journal of Geophysical Research*, 98(C6), pp.10155–10169.

Hohmann, R. et al., 2002. Excess helium and neon in the southeast Pacific: Tracers for glacial meltwater. *Journal of Geophysical Research*, 107(C11, 3198), p.14pp. Available at: http://www.agu.org/pubs/crossref/2002/2000JC000378.shtml.

Huhn, O. et al., 2008. Evidence of deep- and bottom-water formation in the western Weddell Sea. *Deep-Sea Research Part II: Topical Studies in Oceanography*, 55(8–9), pp.1098–1116.

Joughin, I. & Padman, L., 2003. Melting and freezing beneath Filchner-Ronne Ice Shelf, Antarctica. *Geophysical Research Letters*, 30(9), pp.0–3.

Locarnini, R. a., Whitworth, T. & Nowlin, W.D., 1993. The importance of the Scotia Sea on the outflow of Weddell Sea Deep Water. *Journal of Marine Research*, 51(1), pp.135–153.

Loose, B. & Jenkins, W.J., 2014. The five stable noble gases are sensitive unambiguous tracers of glacial meltwater. *Geophysical Research Letters*, 41(8), pp.2851–2857.

Markus, T., Kottmeier, C. & Fahrbach, E., 1998. Ice Formation in Coastal Polynyas In the Weddell Sea and Their Impact on Oceanic Salinity. In *Antarctic Sea Ice: Physical Processes, Interactions and Variability*.

American Geophysical Union, pp. 273–292. Available at: http://dx.doi.org/10.1029/AR074p0273.

Michels, K.H. et al., 2002. The southern Weddell Sea: combined contourite-turbidite sedimentation at the southeastern margin of the Weddell Gyre. *Geological Society, London, Memoirs*, 22(1), pp.305–323.

Nicholls, K.W., Makinson, K. & Øterhus, S., 2004. Circulation and Water Masses Beneath the Northern Ronne Ice Shelf, Antarctica. *Journal of Geophysical Research C: Oceans*, 109(12), pp.1–11.

Paolo, F.S., Fricker, H.A. & Padman, L., 2015. Volume loss from Antarctic ice shelves is accelerating. *Science*, 348(6232), pp.327–331.

Rignot, E. et al., 2013. Ice-shelf melting around Antarctica. *Science*, 341(6143), pp.266–70. Available at: http://www.ncbi.nlm.nih.gov/pubmed/23765278.

Rodehacke, C.B. et al., 2007. Ocean/ice shelf interaction in the southern Weddell Sea: Results of a regional numerical helium/neon simulation. *Ocean Dynamics*, 57(1), pp.1–11.

Ryan, S. et al., 2016. On The Warm Inflow at The Eastern Boundary of the Weddell Gyre. *Deep-Sea Research Part I: Oceanographic Research Papers*, 107, pp.70–81. Available at: http://dx.doi.org/10.1016/j.dsr.2015.11.002.

Schlosser, P., 1986. Helium: a new tracer in Antarctic oceanography. *Nature*, 321(6067), pp.233–235. Available at: http://www.nature.com/doifinder/10.1038/321233a0.

Seehaus, T. et al., 2015. Changes in ice dynamics, elevation and mass discharge of Dinsmoor-Bombardier-Edgeworth glacier system, Antarctic Peninsula. *Earth and Planetary Science Letters*, 427, pp.125–135. Available at: http://dx.doi.org/10.1016/j.epsl.2015.06.047.

Sültenfuss, J., Roether, W. & Rhein, M., 2009. The Bremen mass spectrometric facility for the measurement of helium isotopes, neon, and tritium in water. *Isotopes in environmental and health studies*, 45(2), pp.83–95.

Timmermann, R. & Hellmer, H.H., 2013. Southern Ocean warming and increased ice shelf basal melting in the twenty-first and twenty-second centuries based on coupled ice-ocean finite-element modelling. *Ocean Dynamics*, 63(9–10), pp.1011–1026.

Weiss, R.F., 1971. Solubility of Helium and Neon in Water and Seawater. *Journal of Chemical & Engineering Data*, 16(2), pp.235–241. Available at: http://pubs.acs.org/doi/abs/10.1021/je60049a019.

List of Figures

List of Tables